SCAVENGER RECEPTOR A1 DISTINGUISHES BOVINE SERUM ALBUMIN-COATED PRISTINE AND CARBOXYLATED MULTI-WALLED CARBON NANOTUBES

by

Mai T. Huynh

APPROVED BY SUPERVISORY COMMITTEE:

Rockford K. Draper, Co-Chair

Paul Pantano, Co-Chair

Sheena D'Arcy

Warren J. Goux

This dissertation is dedicated to my wonderful family.

For their endless love, care, and support.

SCAVENGER RECEPTOR A1 DISTINGUISHES BOVINE SERUM ALBUMIN-COATED PRISTINE AND CARBOXYLATED MULTI-WALLED CARBON NANOTUBES

by

MAI T. HUYNH, BS

DISSERTATION

Presented to the Faculty of

The University of Texas at Dallas

in Partial Fulfillment

of the Requirements

for the Degree of

DOCTOR OF PHILOSOPHY IN

CHEMISTRY

THE UNIVERSITY OF TEXAS AT DALLAS

May 2021

ACKNOWLEDGMENTS

I thank the following agencies for funding my research: The University of Texas at Dallas – Eugene McDermott Graduate Fellows Programs and the National Science Foundation – Graduate Research Fellowships Program. I am extremely grateful to my advisors, Dr. Rockford Draper and Dr. Paul Pantano for their tremendous support, patience, motivation, and enthusiasm during my PhD study. They gave me the golden opportunity to do work on these wonderful projects and provided me with excellent scientific guidance throughout my graduate career. I would also like to extend my deepest gratitude to Dr. Paul Pantano for his guidance through each stage of my research project and inspiring me to grow as an independent scientist over the last seven years. I am equally deeply grateful to my other advisor, Dr. Rockford Draper for his helpful advice and invaluable and scientific insight into my research projects. I would like to express my deepest appreciation to Dr. Carole Mikoryak for spending time advising me and training me in the various methodologies needed to carry out the research. She has encouraged me throughout my academic research and daily life. I would like to extend my sincere thanks to my two committee members, Dr. Sheena D'Arcy and Dr. Warren Goux, and my Examining Committee Chair Dr. Li Zhang for providing their support and extensive knowledge. I would like to extend my gratitude to Dr. Thomas Lambert for teaching me the methodology of how to present my research work as clearly as possible. I thank Dr. Ruhung Wang for her scientific contributions, and Dr. Vasanth Murali for confocal Raman microscopy training. I thank Alex Brown, Jason Lin, Shashini Diwakara, Hong Pham, Raina Rahman, Samad Yousuf and Bryanna LeGrand for their hard work with our joint publication. I also thank Dr. Jean Francois Veyan, Dr. Kenneth Balkus, Jr., and Dr. Ronald A. Smaldone for contributions to our joint publication.

I would not have been able to finish my projects without them. I am grateful to Rishma Sharma, Dineli Ranathunga, Nooshin Akhavan, Sameera Abeyrathna, Nisansala Abeyrathna, Nancy Jacobsen, Ishwar Chuckaree, Rishabh Lohray, Erik Chow, Pratima Gangupantula, Loren Leigh Smith for being such great friends. I also wish to thank Dr. Winston Layne for helping trouble shoot problems I encountered with various instruments. I would like to acknowledge the Chemistry and Biochemistry department staff members Betty, Kelly, Stacey, Sadhona, and George and Biological Sciences staff members Mike and Micah for their support. I would like to extend my sincere thanks to Reena Schellenberg and The Eugene McDermott Student Programs staff members for their constant support. I would like to thank The Office of Graduate Education staff members for their support. My success and my completion of my dissertation could not have been possible without the support and nurturing of my family members, my grandparents, my parents, and my sister – Phuong Huynh.

April 2021

SCAVENGER RECEPTOR A1 DISTINGUISHES BOVINE SERUM ALBUMIN-COATED PRISTINE AND CARBOXYLATED MULTI-WALLED CARBON NANOTUBES

Mai T. Huynh, PhD
The University of Texas at Dallas, 2021

Supervising Professors: Rockford K. Draper, Co-Chair
Paul Pantano, Co-Chair

This dissertation concerns the interactions of multi-walled carbon nanotubes (MWNTs) with mammalian macrophages, cells that are first responders to foreign invaders in the body. The production and use of MWNTs are rapidly increasing world-wide despite the possible adverse effects they may have on human health. For example, MWNTs pose a human respiratory hazard because they can cause pulmonary fibrosis, which may lead to mesothelioma. How MWNTs trigger such adverse effects is not well understood, especially whether MWNT binding to surface receptors on macrophages occurs. A complicating factor is what effects a protein corona, derived from serum proteins such as bovine serum albumin (BSA), may have on the interaction of MWNTs with cells. Achieving consensus in this research field is hampered by batch-to-batch inconsistencies with commercially synthesized MWNTs. This dissertation first presents a comprehensive physicochemical characterization of two lots of pristine MWNTs (pMWNTs) and carboxylated MWNTs (cMWNTs), which is important since the biological response of MWNTs is related to their physicochemical properties. There were many similarities between the physicochemical properties of the two commercial lots of cMWNTs and neither significantly

diminished the 24-h proliferation of RAW 264.7 macrophages up to the highest concentration tested (200 μg cMWNTs/mL). Conversely, several physicochemical properties of the two lots of pMWNTs were different: notably, the newer lot of pMWNTs displayed less oxidative stability, a higher defect density, and a smaller amount of surface oxygen species relative to the original lot. Furthermore, a 72-h half maximal inhibitory concentration of ~90 μg pMWNTs/mL was determined for RAW 264.7 cells with the new lot of pMWNTs. These results demonstrate that subtle physicochemical differences can lead to significantly dissimilar cellular responses, and that production-lot consistency must be considered when assessing the toxicity or biomedical performance of MWNTs. Next, using the lots of well-characterized pMWNTs and cMWNTs, the interaction of MWNTs with class A-type 1 scavenger receptors (SR-A1s) was studied with a direct binding assay under conditions where the influence of nanotube functionalization and protein coronas could be carefully controlled. Both pMWNTs and cMWNTs coated with BSA bound to and were accumulated by RAW 264.7 macrophages, although the cells bound two times more BSA-coated cMWNT than pMWNTs. RAW 264.7 cells that were deleted for SR-A1 using CRISPR-Cas9 gene-editing technology had markedly reduced binding and accumulation of both BSA-coated cMWNTs and pMWNTs, suggesting that SR-A1 was responsible for the uptake of both MWNT types. Moreover, Chinese hamster ovary (CHO) cells that ectopically expressed SR-A1 accumulated both MWNT types, whereas wild-type CHO cells did not. One model to explain these results is that SR-A1 can interact with two structural features of BSA-coated cMWNTs, one inherent to the carboxylated nanotubes and the other provided by the BSA corona, whereas SR-A1 only interacts with the BSA corona of BSA-pMWNTs. A better understanding of the

mechanisms by which MWNTs interact with macrophages should lead to the rational design of nanotoxicity remediation efforts and biomedical applications of carbon nanomaterials.

TABLE OF CONTENTS

LIST OF FIGURES

LIST OF TABLES

CHAPTER 1

INTRODUCTION

1.1. CARBON NANOTUBE BACKGROUND

1.1.1. What are Carbon Nanotubes?

Engineered nanomaterials (ENMs) are used in a broad range of applications including biomedicine [1-6], electronics [7], and catalysis [8-10]. Among the ENMs, carbon-based structures are attractive for many applications. Carbon exists in more than one crystalline form and the various forms are called allotropes. The major carbon allotropes are diamond, graphene, fullerenes, and carbon nanotubes (CNTs). In 1991, CNTs were first atomically described and synthesized by Iijima [11] and come in two basic types, single-walled CNTs (SWNTs) or multi-walled CNTs (MWNTs) as shown in Figure 1.1. SWNTs are a single graphene sheet of sp^2-hybridized carbon rolled into a cylindrical tube along an (m,n) chiral vector in the graphene with diameters around 0.5-1.5 nm [12]. How the sheets are aligned when they are rolled up profoundly affects the properties of the resulting SWNTs, which can be either zigzag, armchair, or chiral as shown in Figure 1.2 [13]. The chiral indices (m,n) that define the chiral vector C determine the diameter and chirality. When m = 0, SWNTs are called zigzag SWNTs; when n = m, SWNTs are called armchair SWNTs, and when $n \neq m$, SWNTs are called chiral SWNTs. On the other hand, MWNTs contain two or more sheets of sp^2-hybridized carbon rolled into tubes nestled one within another by van der Waal forces [14], with diameters ranging from 2-100 nm and their interlayer distances of approximately 0.34 nm.

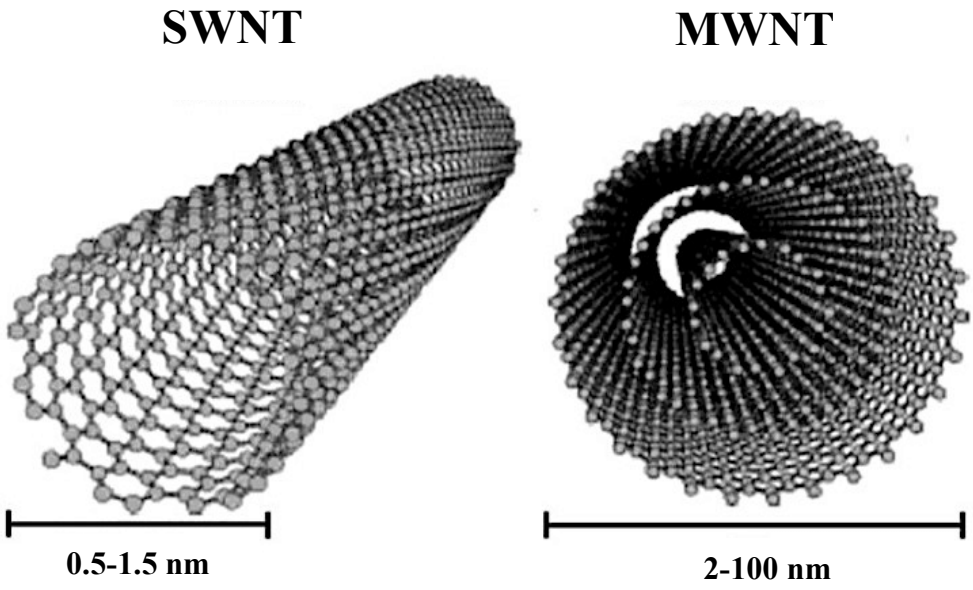

Figure 1.1. Schematic representation of a single-walled carbon nanotube with a diameter around 0.5-1.5 nm and a multi-walled carbon nanotube with diameters ranging from 2-100 nm [15], reproduced with permission from *Journal of Dental Research*.

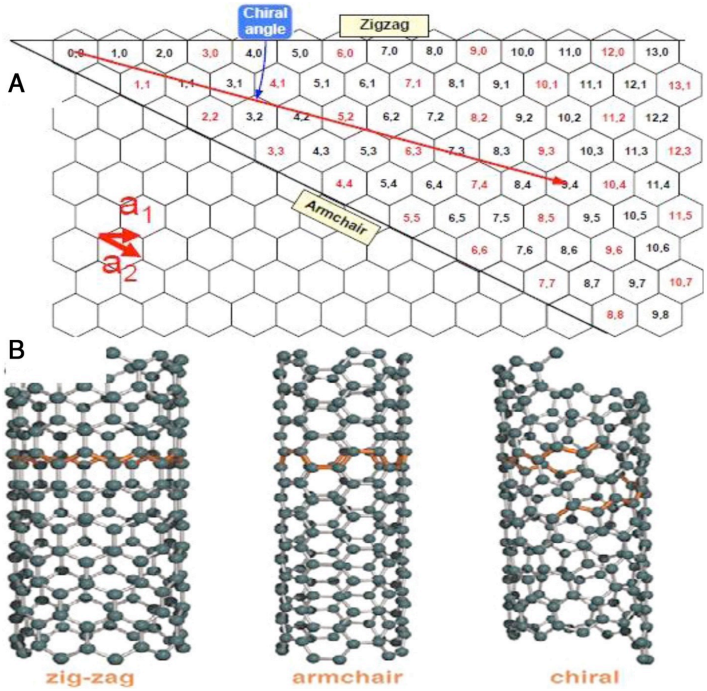

Figure 1.2. Different structures of SWNTs. **(A)** A SWNT structure is determined by two indices (n,m) that define the chiral vector C. The chiral vector C also determines the tube diameter. **(B)**

Models of three atomically perfect SWNT structures: zigzag, armchair, and chiral. The integers n and m determine the number of unit vectors in the honeycomb crystal lattice of graphene. When m=0, SWNTs are called zigzag SWNTs; when n=m, SWNTs are called armchair SWNTs, and other states are called chiral SWNTs. The SWNT structures have an effect on electrical properties of SWNTs, for example *armchair* SWNTs share electrical properties similar to metals and *zigzag* and *chiral* SWNTs possess electrical properties similar to semiconductors. This figure is reproduced with permission from *Materials Today* [13].

1.1.2. CNT Synthesis

There are three basic methods for the synthesis of CNTs, which mainly involve a gas phase process with metals, such as iron, cobalt, and nickel as catalysts: electrical arc discharge [16], laser vaporization [17,18], and chemical vapor deposition (CVD) [19]. The electrical arc discharge method uses high-purity graphite electrodes, acting as cathode and anode, and placed 1-2 mm apart in 400 mbar of a helium, hydrogen, or methane atmosphere. The electrodes are evaporated using high current (100 A) and high temperature (greater than 1,700 ^{o}C) to form CNTs that deposit on the cathode tip [11]. In laser vaporization, a quartz tube containing a block of pure graphite is combusted inside a furnace at 1,200 ^{o}C in an argon atmosphere using high-power laser vaporization, and the CNTs develop in the gaseous phase and are separated as they form [17]. CVD processes are the dominant modes of high-volume production due to low energy consumption, low waste generation, and the ability to tailor MWNT properties such as their outer diameters, lengths, alignment, purity, density, and orientation [20,21]. CVD requires lower temperatures (below 800 ^{o}C) than arc-discharge and laser vaporization. In the CVD process carbon molecules and a combination of metal catalysts including iron, nickel, and/or cobalt are used in a hydrogen or carbon monoxide atmosphere to form CNTs on the catalysts inside a high temperature furnace.

1.1.3. CNT Properties and Applications

CNTs are one of the allotropes of carbon with unique structural, mechanical, and electronical properties such as high thermal conductivity and expansion, electrical conductivity, strength and elasticity, electron emission, and high aspect ratio (Table 1.1). SWNTs are electrically conducting or semi-conducting, while MWNTs are usually conducting [22]. The structure of the tube determines whether a particular SWNT is electrically conducting or semi-conducting [23,24]. For examples, armchair SWNTs share electrical properties similar to metals and the zigzag and chiral SWNTs possess electrical properties similar to semiconductors [25]. Since each carbon atom in a graphene sheet is connected by a strong chemical bond to three neighboring atoms, CNTs are expected to have a higher tensile strength than steel and elasticity properties that are very resistant to damage from physical forces. Many studies have reported that CNTs are great thermal conductors that are stable at temperatures to 750 ^{o}C at atmospheric pressure and up to 2,800 ^{o}C under vacuum [26-30].

The unique physicochemical properties of CNTs lend themselves to a variety of industrial and biomedical applications. In fact, their electrical, mechanical and thermal conductivity properties make CNTs a good choice in the development of light weight, high tensile strength, and great thermal conductivity composite materials [31-34], nanoprobes and sensors [35-37], and devices for energy conversion and storage [38-40]. CNTs are also used in a wide range of biomedical applications from drug delivery to imaging to improving cancer therapies and use as antiviral agents [41-46]. CNTs have also been used in tissue engineering such as bone tissue regeneration [47] and nervous tissue regeneration [48].

Table 1.1. Theoretical and experimentally measured properties of CNTs, reproduced with permission from *Wiley* [49].

Property	Carbon nanotubes
Lattice structure	- (Cylindrical) hexagonal lattice helicity - Nanotubes: ropes, tubes arranged in triangular lattice with lattice parameters of a =1.7 nm, tube-tube distance = 0.314
Specific gravity	- 0.8-1.8 gcc^{-1} (theoretical)
Elastic modulus	- ~1 TPa for SWNT - ~0.3-1 TPa for MWNT
Strength	- 50-500 GPa for SWNT - 10-50 GPa for MWNT
Resistivity	- ~5-50 micro-ohm·cm
Thermal conductivity	- 3000 W $m^{-1}K^{-1}$ (theoretical)
Thermal expansion	- Negligible (theoretical)
Oxidation in air	- >700º C

1.2. CNT TOXICITY

The diversity of CNT applications is one driver of the exponential growth in their production and market opportunities. The production of MWNTs currently dominates the market, because they are easier to synthesize in large quantities compared to SWNTs and they are used in more large-scale products. However, the potential toxicity and hazard of MWNTs in biomedical applications, the workplace, and the environment has been reported and is raising environmental, health and safety (EH&S) concerns [50-56]. MWNT toxicity depends on the unique properties of

MWNTs, such as length, diameter, surface area, functionalization state of the CNTs, degree of aggregation, and purity. For example, MWNTs are larger and longer than SWNTs and there are reports suggesting that MWNTs, but not SWNTs, initiate chronic inflammatory responses that cause pulmonary fibrosis, and the similarity of MWNTs to asbestos could therefore potentially cause mesothelioma [57,58]. In other studies, the authors reported that MWNTs of different lengths cause different levels of toxicity that can lead to pulmonary fibrosis [59-61]. The Donaldson group has published a series of papers supporting the idea that MWNTs longer than 10-30 μm initiate a proinflammatory response that results in fibrosis, while shorter MWNTs do not [58,62-64]. Many of the early studies on CNT toxicity used unpurified preparations that were contaminated with metal catalysts (often iron) and other impurities that were themselves toxic, obscuring the potential role of CNTs in toxicity [65-67]. CNTs also differ in their covalent or non-covalent functionalization that could introduce variance in toxicity. Covalent functionalization, such as carboxylation or addition of amine groups, changes the surface charge on the CNTs, which might affect toxicity. In addition, the surface structure of MWNTs has also been correlated with pulmonary toxicity: MWNTs with defects in the carbon lattice framework were more toxic in pulmonary assays than non-functionalized or pristine MWNTs (pMWNTs) [68,69]. Further, MWNTs with surface carboxylation induced more inflammatory responses than pMWNTs [70], a conclusion exactly opposite that reached by Nel and co-workers [71]. Non-covalent functionalization, such as coating CNTs with various materials that do not covalently bond to the CNTs, introduces another variable. In addition, CNTs must be reliably dispersed and debundled using a biocompatible material in aqueous solution to enable testing of biological toxicity. Wang et al. reported that bovine pulmonary surfactant Survanta® coated SWNTs do not cause a cytotoxic

or fibrogenic effect at physiologically relevant concentrations [72]. Liao and co-workers reported that MWNTs coated with the dispersant Pluronic® F-108 (PF108) did not induce proinflammatory responses in vitro or in vivo, whereas MWNTs coated with bovine serum albumin (BSA) were proinflammatory [73]. Similarly, coating MWNTs with polystyrene-based polymers protected against pulmonary toxicity [74]. However, Holt et al. demonstrated that PF108-coated SWNTs damaged the lysosomal membrane of HeLa cells sufficiently to release SWNTs into the cytosol, but BSA-coated SWNTs did not [75]. In addition, to better understand potential mechanisms of CNT toxicity, or lack of toxicity, part of the information that needs to be collected is the applied CNT dose, and more importantly, the amount of CNTs that actually accumulate in a cell, a model tissue, or organism, and whether the CNTs physically enter cells and where in the cells they reside. Acquiring this information requires imaging the sample in a way that will detect the CNTs. These matters are important for understanding the exact mechanisms of CNT toxicity, and also how to rationally design strategies to remediate or avoid CNT toxicity.

1.3. SODIUM DODECYL SULPHATE - POLYACRYLAMIDE GEL ELECTROPHORESIS (SDS-PAGE) METHOD TO MEASURE CELL ASSOCIATED MWNTS

An important parameter in a model system such as cytokine release via the inflammasome pathway is how cytokine release depends on the amount of irritant MWNTs that are actually internalized within vacuolar compartments. Both to measure toxicity and inflammation, it is essential to measure the amount of MWNTs taken up by cells. The SDS-PAGE method is a rapid and highly sensitive method to quantify CNTs extracted from cells [76-78].

Throughout projects in this thesis, the SDS-PAGE method with optical detection was used to quantify the amount of BSA-MWNTs bound and accumulated by cells [76,78]. When BSA-MWNTs in SDS sample buffer are loaded on the polyacrylamide gel, the SDS removes the BSA and binds to the MWNTs giving them a negative charge so they will migrate toward the anode, but the MWNTs are too large to enter the gel and are trapped and concentrated at the surface of the stacking gel. The optically measured band intensities are proportional to the amount of MWNTs loaded onto the gel with a detection limit of 5 ng CNTs and are digitized using a 16-bit flat-bed scanner and quantified using *ImageJ* software [76-78]. The amount of MWNTs in unknown samples is determined based on a standard curve developed from known MWNT amounts run simultaneously on the same gel and the results are expressed typically as femtograms of MWNTs per cell. The SDS-PAGE method was previously validated by a large area Raman scan technique [76,78].

As an example of the SDS-PAGE method, RAW 264.7 cells were incubated in medium containing 100 μg/mL BSA-MWNTs for 1, 2, 3, 4, 5, or 6 hours (Figure 1.3). Next, the cells were washed to remove excess MWNTs and lysed with cell lysis buffer. A standard 1 mg/mL of BSA-MWNT suspensions was used to construct the standard curve by loading increasing known amounts of BSA-MWNTs (0, 50, 150, or 250 ng BSA-MWNTs). Aliquots of the cell extracts (lane 5-10) were loaded in the gel wells with a set of varying amounts of standard MWNTs in adjacent wells (lane 1-4). The amount of MWNTs taken up by cells was determined from the linear regression plot of the measured optical density as a function of the applied amounts of the standard MWNTs. As shown in Figure 1.3, RAW 264.7 cells accumulated BSA-MWNTs as a linear function of incubation time. The SDS-PAGE method with optical detection was used in

Chapter 2 to compare the accumulation of different lots of pristine and oxidized MWNTs by cells, and it was used in Chapter 3 to study the interaction of BSA-MWNTs with macrophages and to identify the receptor(s) for BSA-MWNTs, as detailed in section 1.9.

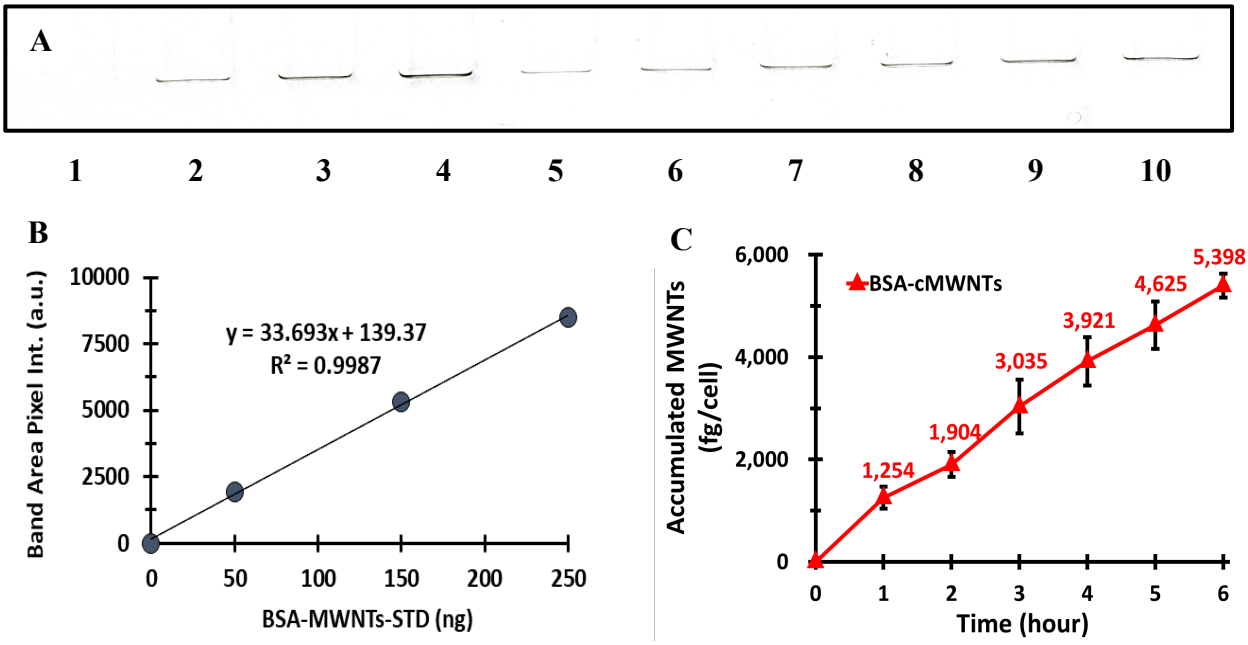

Figure 1.3. Determination of the amount of MWNTs extracted from RAW 264.7 cells cultured in media containing BSA-MWNTs as a function of incubation time. **(A)** Scanned digital image measured as pixel intensity of the BSA-MWNTs band area at the top of the stacking gel following SDS-PAGE. Lane 1-4, known amounts of 0, 50, 150, or 250 ng BSA-MWNTs respectively; lane 5-6, cell extracts after incubation in media containing BSA-MWNTs for 1, 2, 3, 4,5, or 6 hours, respectively. **(B)** Calibration standard curve developed from known MWNT amounts run simultaneously on the gel (lane 1-4). **(C)** Plot of MWNT accumulation in cell lysate samples as a function of incubation time determined using the standard curve. Data is the mean of ≥3 independent experiments ± SD.

1.4. INTERACTIONS OF CNTS AND MACROPHAGES

1.4.1. What are Macrophages?

Macrophages are a key cell type in the inflammatory response to invaders, whether the invader is a biological material or a manufactured nanomaterial. Macrophages interact with

foreign invaders by binding to a wide range of macrophage surface receptors such as scavenger receptors, toll-like receptors (TLR), Fc receptors, complement receptors, mannose receptors, and C type lectin receptors [79,80]. Macrophages phagocytose bacteria and apoptotic cells, and endocytose various polyanionic particles and modified proteins through class A scavenger receptors and class B scavenger receptors such as SR-B1 and SR-B2 (CD36) [81-85]. Table 1.2 lists the major scavenger receptor ligands and their expression profiles [81]. Fc receptors bind monomeric IgG and include three classes: FcRI, FcRII, and FcRIII [86,87]. Complement receptors recognize complement opsonized particles and interact with the ligands Mycobacterium tuberculosis and zymosan [88-90]. Toll-like receptors such as TLR4 recognize microbial ligands and bind to peptidoglycan and lipopolysaccharide (LPS) [80,91-93]. Mannose receptors, also called β glucan receptors, bind to mannose and fucose [94]. Macrophage responses initially involve interaction of the invader with either a protein or a lipid receptor, followed by an active or passive formation of an endocytic or phagocytic vesicle. Once taken up by the cell, acidification of the vesicle contents occurs and the delivery of lysosomal enzymes to the phagosome takes place as the vesicle matures into a phagolysosome [95,96]. In the phagolysosome, oxidative enzymes may be activated that aid in the destruction of the invading microorganisms. There is a superoxide/peroxynitrite oxidative pathway in macrophages that has been shown to chemically breakdown oxidized CNTs [97-100]. Finally, leakage of the lysosomal protease cathepsin B from the phagolysosomes can activate the NALP3 inflammasome, which in turn may drive growth factor release and cell proliferation resulting in fibrosis and possibly mesothelioma [63,73].

Table 1.2. The major scavenger receptor ligands and expression profiles, reproduced with permission from *Annals of the New York Academy of Sciences* [81].

Class	Scavenger Receptor	Ligands	Expression profile
A	SR-A	AcLDL, oxLDL, β-amyloid, molecular chaperones, EMC, AGE, apoptotic cells, activated B-cell, bacteria.	Macrophages, mast, dendritic, endothelial and smooth muscle cells.
A	MARCO	AcLDL, oxLDL, Apoptotic cells, B-cells, bacteria.	Macrophages, dendritic cells.
B	SR-B	HDL, LDL, oxLDL, apoptotic cells.	Monocytes/macrophages, hepatocytes and adipocytes.
B	CD36	AcLDL, oxLDL, HDL, LDL, VLDL, β-amyloid, AGE, apoptotic cells.	Macrophages, platelets, adipocytes, epithelial and endothelial cells.
E	LOX-1	oxLDL, molecular chaperones, EMC, AGE, apoptotic cells, activated platelets, bacteria.	Endothelial and smooth muscle cells, macrophages, and platelets.
F	SRECI/II	AcLDL, OxLDL, molecular chaperones, apoptotic cells.	Endothelial cells and macrophages.
G	SR-PSOX	OxLDL and bacteria.	Macrophages, smooth muscle, dendritic, endothelial cells, B- and T-cells.
H	FEEL-I/II	AcLDL, molecular chaperones, ECM, AGE, bacteria.	Monocytes/macrophages, endothelial cells.

Table 1.2 abbreviations: SR-A: scavenger receptor class A, AcLDL: acetylated low density lipoprotein, OxLDL: oxidised low density lipoprotein, ECM: extracellular matrix, AGE: advanced glycation end products, MARCO: macrophage receptor with collagenous structure, HDL: high density lipoprotein, LDL: low density lipoprotein, VLDL: very low density lipoprotein, LOX-1:

lectin-like oxidized low density lipoprotein receptor-1, FEEL-I/II: fasciclin, epidermal growth factor (EGF)-like, laminin-type EGF-like, and link domain-containing scavenger receptor-1.

1.4.2. CNT Uptake Mechanisms of Macrophages

Endocytosis and passive diffusion (nano-needle effects) are two main CNT uptake mechanisms as shown in Figure 1.4 [101,102]. Endocytosis is an active process that involves the capture of material bound to the surface of a cell and brought into the cell inside a membrane-bound endocytic vesicle that is formed from the phospholipid bilayer of the cell's plasma membrane. This process is energy dependent and hindered at low temperatures and low ATP environments. Endocytosis includes phagocytosis, receptor-mediated endocytosis, and pinocytosis. Phagocytosis is a process in which a cell engulfs or ingests large particles (>0.5 μm) or other cells using its plasma membrane to engulf the particles and bring them into the cells where a phagolysosome is formed. Receptor-mediated endocytosis is the process in which a cell transports specific substances such as proteins, hormones, and metabolites into the cells through binding to specific cell surface receptors. Pinocytosis is the process where small molecules in the extracellular fluid are taken into the cells by forming small vesicles that include molecules in the extracellular fluid. In contrast, passive diffusion is a process that allows direct translocation through the plasma membrane. Exocytosis is an energy-dependent process in which a cell transports the contents of a vacuole out of the cell by secretion.

There are three outcomes for a CNT taken up by cell: it persists in the cell, or is broken down in the phagolysosome, or it is exocytosed out of the cell. Once CNTs are internalized, the formation of endocytic or phagocytic vesicles occur and early phagosomal/endosomal vesicles remodel their membranes in transit by maturing into a phagolysosome and the pH within the

vesicles drops as a result of active proton pumping by the V-type ATPase. Biodegradation and exocytosis of CNTs were reported as cell elimination mechanisms of CNTs [102]. Oxidized CNTs are degraded in the phagolysosome through a superoxide/peroxynitrite oxidative pathway [95-98]. Marangon et al. reported that macrophages and endothelial cells can release CNT content of vesicles when exposed to stress [103]. Using ultraviolet visible near infrared (UV-Vis NIR) spectroscopy, Cui et al. found that cell-associated SWNTs were released over time after removal of the SWNT containing media [104].

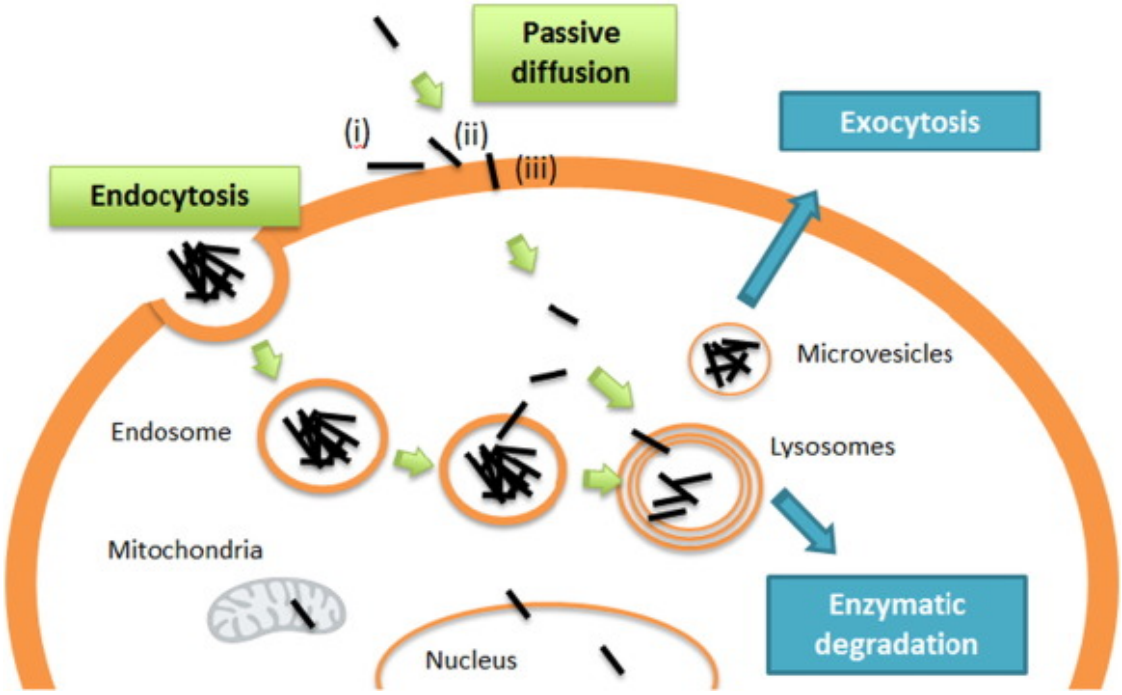

Figure 1.4. Schematic representation of the two main mechanisms of CNT cellular uptake: endocytosis and passive diffusion, and exocytosis. In one mechanism MWNTs are internalized by the endocytosis pathway. In a proposed second pathway individual MWNTs **(i)** contact the cellular membrane **(ii)** penetrate the cellular membrane and **(iii)** cross the cellular membrane by passive diffusion. Once internalized macrophages and endothelial cells can release their CNT content in vesicles by the exocytosis pathway. Macrophages have a superoxide/peroxynitrite oxidative pathway that has been shown to chemically degrade oxidized CNTs [102], image reproduced with permission from *Elsevier*.

Each CNT uptake mechanism can be influenced by several features and parameters, including length, diameter, synthetic method, surface functionalization of the CNTs, and agglomeration state. Pantarotto et al. [105] and Liu et al. [106] reported that SWNTs in dispersions can enter the cytoplasm of cells by directly crossing the cellular membrane, a conclusion exactly opposite that reached by Yaron et al. who confirmed that SWNTs enter the cells by endocytosis and not by membrane penetration [107]. Zhao et al. stated that CNTs that were greater than 1 μm in length were internalized by phagocytosis [108]; shorter CNTs, from a few to several hundred nanometers, were taken up by pinocytosis, or receptor-mediated endocytosis [101,108]. On the other hand, Antonelli et al. reported that macrophages internalized functionalized SWNTs with lengths greater than 400 nm by endocytosis and those that were shorter than 400 nm penetrated the cellular membrane [109]. Cui et al. reported that the uptake of SWNTs was a length independent process and involved several pathways: micropinocytosis, caveolae mediated endocytosis, and receptor mediated endocytosis [104]. Thus, it is difficult to conclude that different responses to long and short MWNTs were due only to length differences. The different cellular responses may also be due to numerous other features, including diameter, synthetic method, the amount of carbonaceous and metallic contaminants and agglomeration state. In studies by Nel and co-workers, all the MWNTs were derived from the product of one vendor that was either purified or carboxylated by the researchers, which should help to control differences [71,73,110]. However, the MWNTs were then either shortened by sonication and mixed with BSA and lipid as co-dispersants, or not sonicated and directly added to culture medium in a non-dispersed agglomerated state. It is not clear what differences between the two BSA-coated MWNT preparations is responsible for the difference seen in the pro-fibrogenic effects [73]. Wang et al.

and Kam et al. reported that mammalian cells internalized SWNTs and MWNTs, mainly by receptor mediated uptake [111,112]. In conclusion, the existing literature reveals many examples of knowledge gaps and conflicting results regarding the interaction of CNTs with cells and their receptors.

In this project, we have observed that BSA-coated pMWNTs and carboxylated MWNTs (cMWNTs) exposed to RAW 264.7 cells for 24 h at 37 °C accumulated inside the cells within punctate vesicles, most likely in the endosome/lysosome system, but not in the cytoplasm using laser scanning confocal Raman microscopy (Figure 1.5). Furthermore, Raman imaging of the surface binding of BSA-cMWNTs in RAW 264.7 at 4 ºC shows that the cMWNT signals are only found on the peripheral membrane of the cell (Figure 1.6). Our data suggests that the uptake of BSA-MWNTs involves an energy-dependent receptor-mediated endocytosis pathway. Due to the fact that BSA-coated MWNTs are discussed throughout this thesis and macrophages have the ability to recognize negatively charged ligands and modified proteins, the effect of a protein corona on the binding and accumulation of MWNTs are discussed in section 1.5.

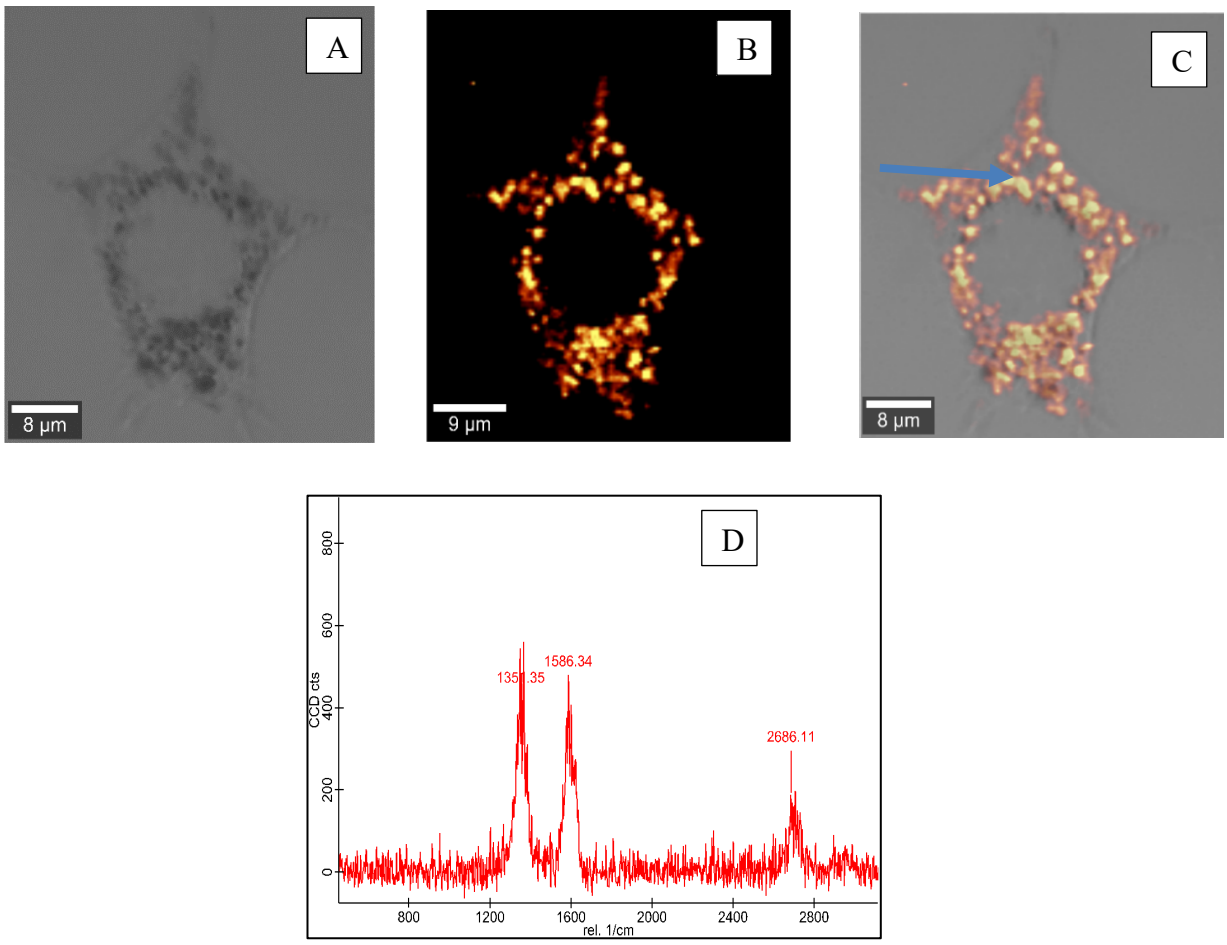

Figure 1.5. Detecting MWNTs inside cultured cells by laser scanning confocal Raman microscopy. **(A)** Optical image of a typical RAW 264.7 cell that was incubated with 100 µg/mL of MWNTs for 3 h at 37 ºC, followed by a 30-minute chase and then fixed on the imaging dish. **(B)** Raman scan of the cell where the Raman signal of MWNTs (1480 – 1580 cm^{-1}) at every pixel was mapped to a color profile with yellow being the highest intensity and red a lower intensity. **(C)** Overlay of panels A and B to show co-localization of the MWNTs Raman signals with vesicles in the cell. **(D)** Background subtracted Raman spectrum taken from one pixel in the hot spot indicated by the blue arrow in C to verify the presence of the intense MWNTs peak G band (~1585 cm^{-1}) and D band (~1350 cm^{-1}).

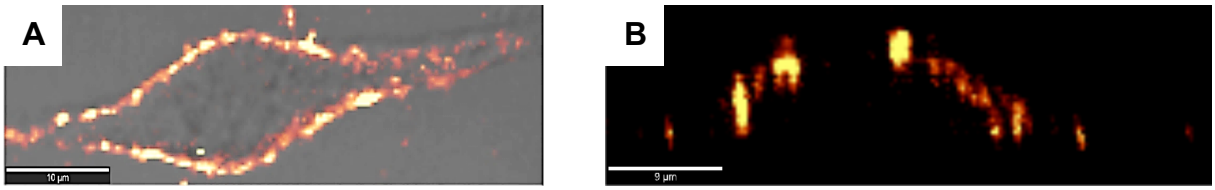

Figure 1.6. Raman imaging of BSA-cMWNTs binding to a RAW 264.7 cell at 4 ºC. The low temperature inhibits phagocytosis of the MWNTs so that data interpretation only considers interaction of ligands with the plasma membrane. **(A)** Overlay of bright-field and G-band of the cMWNT to show MWNTs signals are only found on the membrane at the periphery of the cell. **(B)** Raman scan of x-z slice through the center of the same cell where the Raman signal of MWNTs (1480 – 1580 cm^{-1}) at every pixel was mapped to a color profile with yellow being the highest intensity.

1.5. EFFECT OF PROTEIN CORONA ON THE BINDING AND INTERNALIZATION OF MWNTS

In 1964, Vroman and his colleagues first published a series of articles revealing that when synthetic materials, especially ENMs are in biological fluid, they are quickly coated by proteins [113-115]. This protein adsorbed to ENMs is called a protein corona. The types of proteins adsorbed depends on the composition of the biological substrate and on the ENM surface charge, structure, hydrophilicity/hydrophobicity, size, and shape [116-120]. What proteins are adsorbed to the surface of ENMs influences ENM stability, biodistribution, toxicity, clearance, and especially their interactions with specific cell surface binding sites. Thus, the protein corona formed on ENMs in a biological fluid may have profound effects on their interaction with cells. There is evidence that the compositions of protein coronas can be affected by structural defects, surface chemistry, surface curvature, and the surface area of the MWNTs [121,122]. The formation of protein coronas formed on different functionalized MWNTs are complex and unique. For example, Mu et al. [123] and Bai et al. [124] reported that pMWNTs mainly bind BSA through

π-π stacking interactions between the MWNTs and aromatic residues (Trp, Phe, Tyr) of the protein, whereas the negative charges of carboxyl groups on cMWNTs increase the ability to bind BSA compared to pMWNTs, and this can lead to more BSA binding to cMWNTs compared to pMWNTs [123,124]. However, Lou et al. [125] and Du et al. [126] conclude that hydrophobic and π-π stacking interactions are the major driving forces for binding of BSA to cMWNTs. Zhao et al. also conclude that the hydrophobic surfaces of pMWNTs and cMWNTs interact with hydrophobic and aromatic residues in the hydrophobic pocket of BSA [127]. In fact, the presence of carboxyl groups on the surface of cMWNTs would make the surface of cMWNTs less hydrophobic which could lead to less BSA binding to cMWNTs. Complications are introduced when CNTs are in a complex biological fluid such as serum, pulmonary surfactant, or lymph because there are many different proteins competing for CNT binding and it is difficult to control or model the composition of the protein corona that may have profound effects on the interaction of the CNTs with cells [122,128,129]. Using liquid chromatography-tandem mass spectrometry, Muller et al. showed that cMWNTs bound a greater overall number of proteins and different types of proteins from cell culture medium than pMWNTs [69]. The presence of a protein corona is important because the biological response of cells to MWNTs typically starts with their binding to the plasma membrane, generally via a membrane receptor, followed by consequent internalization inside a vesicle and ultimately into the cell [122,130-132].

1.6. MACROPHAGE RECEPTORS IMPLICATED IN THE INTERNALIZATION OF MWNTS

The effects of a large number of possible CNT surface modifications on many different biological endpoints implies that there could be multiple effects on potential receptors (Table 1.3).

Li et al. stated that MWNTs carrying a variety of covalent functionalities were taken up by macrophages to different levels and provoked different levels of pro-fibrogenic cytokines and growth factors; however, no data on direct binding to specific receptors was presented [110]. In another example, Zhang et al. prepared a combinatorial library of covalently modified MWNTs to screen the library for effects on different signaling pathways [133]. The same group also noted that cMWNTs enhanced the differentiation of the mouse myoblast C2C12 cell line to muscle cells, which was attributed to the binding of cMWNTs to bone morphogenetic protein receptor 2 (BMPR2) using a fluorescence resonance energy transfer (FRET) assay [134]. This indirect evidence suggests that cMWNTs bind to a specific receptor on myoblasts. In addition, the non-covalent modification of CNTs surfaces can also alter the interaction of CNTs with cells. Proteins and surfactant polymers are commonly used to coat the CNT surfaces to improve CNT solubility and biocompatibility. Proteins adsorbed to CNTs are likely to be critical when interacting with macrophages because these cells have many receptors for recognizing opsonized ligands: for example, complement receptors, the Fc receptor family, and integrins [135-137], as well as, receptors recognizing modified proteins such as class A and class B scavenger receptors [138-140].

Table 1.3. Partial list of receptors for CNTs

Functional Group or Structure	Type of receptors	Cell Type	References
PF68-coated MWNTs	MARCO	J774.1 mouse macrophage	Hirano et al. 2008 [141]
Short MWNTs (0.6 μm)	MARCO, SR-A1, CD36	Human alveolar macrophage	Sweeney et al. 2015 [142]
Long MWNTs (20 μm)	MARCO	Human alveolar macrophage	Sweeney et al. 2015 [142]
MWNTs	SR-As	THP-1	Gao et al. 2011 [143]
BSA-coated SWNTs	SR-As	THP-1	Dutta et al. 2007 [140]
HSA-coated MWNTs	Albondin (Gp60)	HepG2	Iancu et al. 2011 [144]
cMWNTs	Bone morphogenetic protein receptor 2 (BMPR2)	Differentiation of the mouse myoblast C2C12 cell line to muscle cells	Zhang et al 2012b [134]

1.7. WHAT ARE SCAVENGER RECEPTORS? ROLE OF SR-AS IN UPTAKE AND BINDING OF MWCNTS

1.7.1. What are Scavenger Receptors?

Macrophage scavenger receptors, first discovered by Brown and Goldstein in 1979, were found to bind and remove modified low-density lipoproteins [145]. Macrophage scavenger receptors are involved in a variety of pathogenic pathways, such as apoptosis, inflammation, and pathogen clearance. They are mainly found on the surface of phagocytic cells such as macrophages, microglia, and dendritic cells and are grouped into twelve classes (Class A-L) as shown in Figure 1.7 [84].

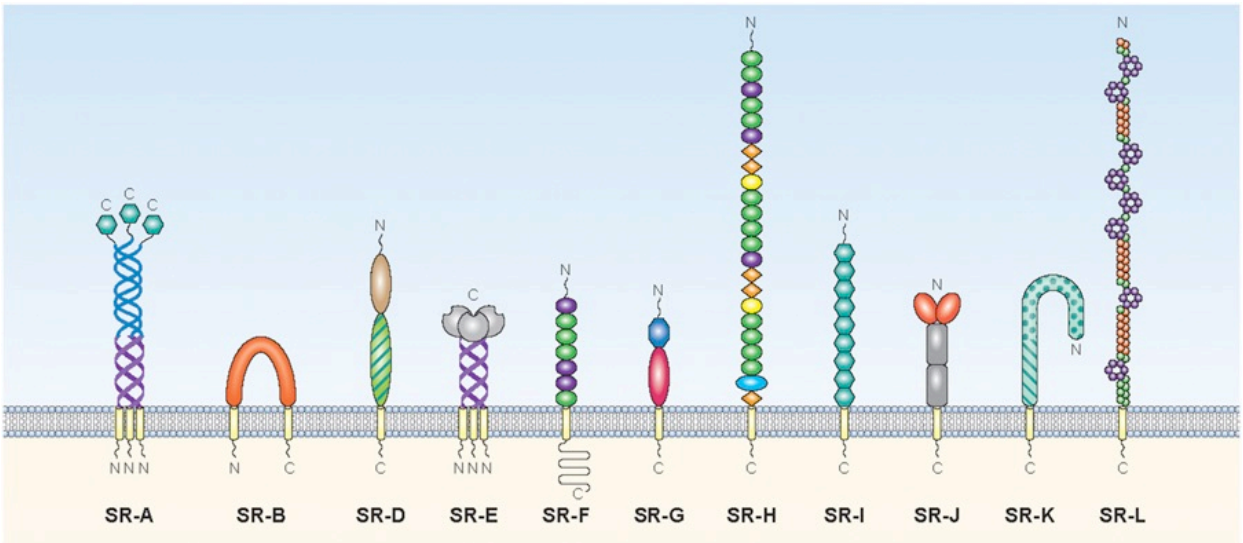

Figure 1.7. Schematic representation of different classes of scavenger receptors. Mammalian scavenger receptors are divided into 12 classes. Class C is not represented here because it is present only in Drosophila melanogaster, reproduced with permission from *the Journal of Immunology* [84].

1.7.2. What are Class A Scavenger Receptors?

Class A scavenger receptors (SR-As) are membrane glycoproteins that bind a variety of polyanionic compounds and modified proteins as listed in Table 1.4. SR-As are usually expressed

on macrophages, endothelial cells, and dendritic cells and include five members: SR-A1, SR-A3, SR-A4, SR-A5, SR-A6 (MARCO) as shown in Figure 1.8 [82,84,146]. There are two forms of SR-A1 referred to SR-A1 and SR-A1.1 [84]. SR-A1.1, a spliced form of SR-A1, is characterized by missing the C-terminal scavenger receptor cystine rich domain (SRCR) [84]. The SR-As share a similar structure that includes an N-terminal cytoplasmic tail, a transmembrane domain, a spacer region, an α-helical coiled coil domain, a collagenous domain, and the SRCR [84].

Table 1.4. SR-A ligands, reproduced with permission from *Immunology* [82]

SR-A ligands	
Acetyl LDL	Maleylated high density lipoprotein
Advance glycation end product modified proteins	Maleylated LDL
Apolipoproteins Al and E	Oxidized LDL
Apoptotic cells	Poly I: Poly C
Beta-amyloid	Polyguanylic acid
Carragreenan	Polyinosinic acid
Collagen	Polyvinyl sulfate
Crocidoloite Asbestos	Polyxanthinylic acid
Cytomegalovirus-human	Proteoglycans
Dextran Sulfate	Ribonucleic acid, double-stranded
Fucoidin	Silica
Glucan	Sulfatides
Heat shock proteins	Lipoteichoic acid
Lipopolysaccharide	Major vault protein

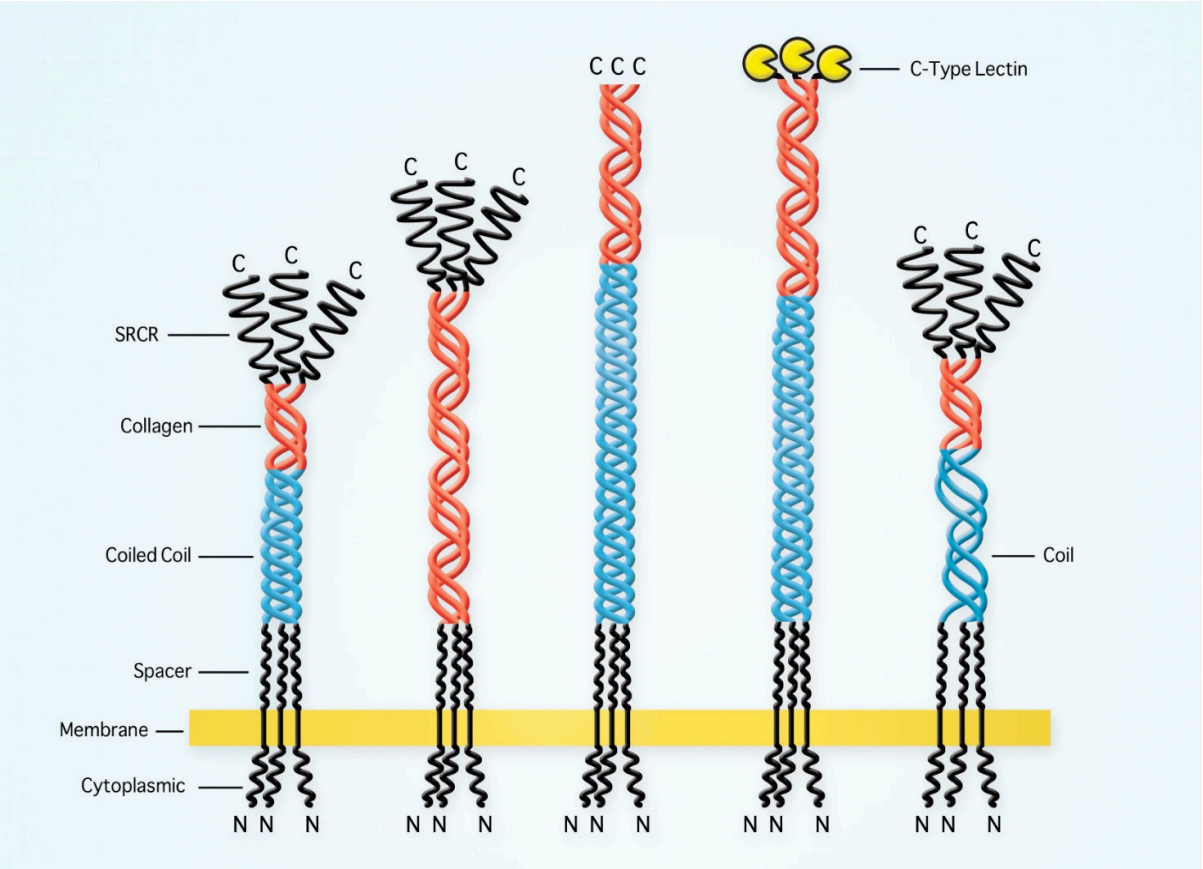

Figure 1.8. The structures of SR-As. SR-As include five members: SR-A1, SR-A3, SR-A4, SR-A5, SR-A6 (MARCO). The SR-As share a similar structure that includes an N-terminal cytoplasmic tail, a transmembrane domain, a spacer region, an α-helical coiled coil domain (except SR-A6), a collagenous domain, and SRCR, reproduced with permission from *Immunology* (Kelly et al. 2014).

The C-terminal SRCR domains are generally around 110 amino acids long, with 6 or 8 conserved cystines that form 3 or 4 disulfide bonds [84]. The SRCR domain has been implicated in large ligand binding and the collagenous domain has been implicated in negatively charged ligand binding to cells. Doi et al. [147] and Andersson et al. [148] reported that the collagenous domain of class A scavenger receptors contains lysine clusters that form areas of positive charge that recognize a wide range of negatively charge ligands, such as clusters of carboxyl groups. Chen

et al. [149], Ojala et al. [150] reported that the SRCR domain has an important role in the ligand binding mechanism of MARCO, a member of the class A scavenger receptors that shares a highly conserved SRCR domain with SR-A1 [151]. The authors also revealed that acetylated low density lipoprotein (acLDL), a 20 nm modified form of LDL, binds to cells expressing full-length MARCO, but not to cells overexpressing MARCO lacking the SRCR domain [149,150]. The authors stated that if each SRCR domain of the trimer in MARCO interact, this can lead to the formation of large oligomeric structures easily capable of effectively binding large objects. Goh et al. also showed that the SRCR domain is essential for large ligand binding of E. Coli DH5α and further that for binding the SRCR domains must be in a trimeric form [152]. Moreover, Brannstrom et al. prepared several MARCO variants with deletions or amino acid substitutions and reported for MARCO the primary bacteria binding region is the positively charged arginine bases in the SRCR domain [153]. Resnick et al. reported that asbestos binds to the same site as all other common ligands of SR-A1, but significantly less well to SR-A1.1 which lacks the SRCR domain. This suggests that the SRCR domain has a role in the binding of asbestos, a large asymmetric molecule [154,155]. Furthermore, Sankala et al. stated that it is possible that cooperation between the SRCR domain and the collagenous domain is needed for high-affinity bacterial binding, or that the SRCR domain has to be in a trimeric form to effectively bind to bacteria [156]. BSA-MWNTs may be considered as a large ligand because of the asymmetry and length of the MWNTs. However, each ligand has a different affinity and capacity to bind to different domains of the receptor and the binding of acLDL or bacteria to SR-A receptors may not be applicable to the binding of BSA-MWNTs. It would be interesting, and of some significance,

to identify which domain(s) of SR-A1 are responsible for the binding and accumulation of MWNTs to SR-A1.

1.7.3. Roles of SR-As in Uptake and Binding of MWNTs

There are several observations in the literature that implicate SR-As as potential carbon nanotube receptors. For example, in an early report BSA absorbed onto SWNTs was shown to bind to scavenger receptors [140]. In later work, the accumulation and the rate of apoptosis among RAW 264.7 cells treated with MWNTs was inhibited by dextran sulfate and poly I, known SR-A antagonists, suggesting that SR-As were involved [138,139]. Hirano et al. reported that MWNTs suspended in the surfactant Pluronic® F68 binds to MARCO with collagenous structure in Chinese Hamster Ovary (CHO) cells that overexpress MARCO [157]. Previous work in our lab with MWNTs suspended in the surfactant PF108 directly demonstrated that macrophages bind and accumulate cMWNTs but not pMWNTs [158,159]. This is true in the absence of fetal bovine serum (FBS) at 4 °C, a condition that avoids any interference by physiological cell processes active at 37 °C or by the presence of serum proteins, suggesting that the Class A scavenger receptor is selective for cMWNTs but not pMWNTs [158,159]. In a previous study, Wang et al. confirmed that macrophages selectively bind Pluronic coated cMWNTs via SR-A1 receptors using a macrophage cell line derived from knockout mice lacking the SR-A1 receptor and by showing that SR-A1 overexpression in CHO cells allowed for MWNT uptake [159]. Another approach to studying receptors is to directly knockout SR-A1 in an established macrophage cell line such as RAW 264.7 cells, and do comparative studies with wild-type and knockout RAW 264.7 cells, as described in Section 1.8.

1.8. PREPARATION AND CHARACTERIZATION OF SR-A1 KNOCK OUT MACROPHAGES USING CRISPR-CAS9 TECHNOLOGY

1.8.1. What is CRISPR-Cas9?

The clustered regularly interspaced short palindromic repeats (CRISPR) and the CRISPR associated protein (Cas) system (CRISPR-Cas9) is a naturally occurring genome editing system in select bacteria and archaea that enables the organisms to respond to and eliminate invading genetic material. CRISPR was first discovered in *E.coli* by Ishino in 1987 [160]. Barrangou et al. stated that *S. thermophilus* can acquire resistance against a bacteriophage by integrating a genome fragment of an infectious virus into its CRISPR locus [161].

CRISPR-Cas has become a unique genetic engineering tool for removing, adding or altering sections of a DNA sequence. It is a simple and precise method of genetic manipulation that has a wide range of applications from basic biology to biotechnology and medicine [162,163]. The 2020 Nobel Prize in Chemistry was awarded to Emmanuelle Charpentier and Jennifer A. Doudna for their work on Crispr-Cas9.

1.8.2. The Components of CRISPR-Cas9

The CRISPR-Cas system consists of a CRISPR-associated endonuclease (Cas9 protein) and one or several guide RNAs (gRNA) that form a ribonucleoprotein (RNP) complex as shown in Figure 1.9. Cas9 is an enzyme with DNA endonuclease activity that cuts two strands of DNA at a specific location so that part of the genome can be added or removed. The gRNA is a pre-designed RNA sequence fragment located within a longer RNA scaffold. The gRNA contains about a 20-base pair sequence that is complimentary to the genomic target. It is designed to find and bind to a specific sequence in the target DNA. The Protospacer Adjacent Motif (PAM) is a

short sequence of nucleotides downstream of the target DNA and is required for the gRNA to bind to the target sequence. The PAM for Cas9 is 5'-NGG-3', where N is any nucleotide. If the gRNA successfully binds to the target DNA, it directs Cas9 to the right part of the target DNA sequence and makes sure that Cas9 cleaves at the correct point in both DNA strands 3-4 nucleotides upstream of the PAM site [164].

1.8.3. CRISPR-Cas9 Editing Mechanism

The CRISPR-Cas9 genome editing mechanism is shown in Figure 1.9. The specific gRNA sequence is designed to find and bind the target DNA in the nucleus of the cell. The Cas9 follows the gRNA to the same location in the DNA sequence and forms an RNP complex. Cas9 then cleaves both strands of the DNA. This creates a double strand break at the genomic target. At this stage, the cell recognizes that there is an error and DNA repair mechanisms are activated. There are two endogenous repair mechanisms that are used to edit genes: non-homologous end joining and homology-directed repair. The cell usually repairs the break by ligating the DNA ends back together called non-homologous end joining repair. During this process it may insert or delete nucleotides. If the number of nucleotides inserted or deleted is not divisible by three, it will create a frameshift mutation that will likely disrupt the gene so that no functional protein is made (this is called a knock-out) [164]. If a DNA template containing the desired sequence is provided along with CRISPR-Cas components to the cells, the cells will use this template to repair the broken sequence via homology-directed repair. It will incorporate the desired changes into the target region (this is called a knock-in) [164].

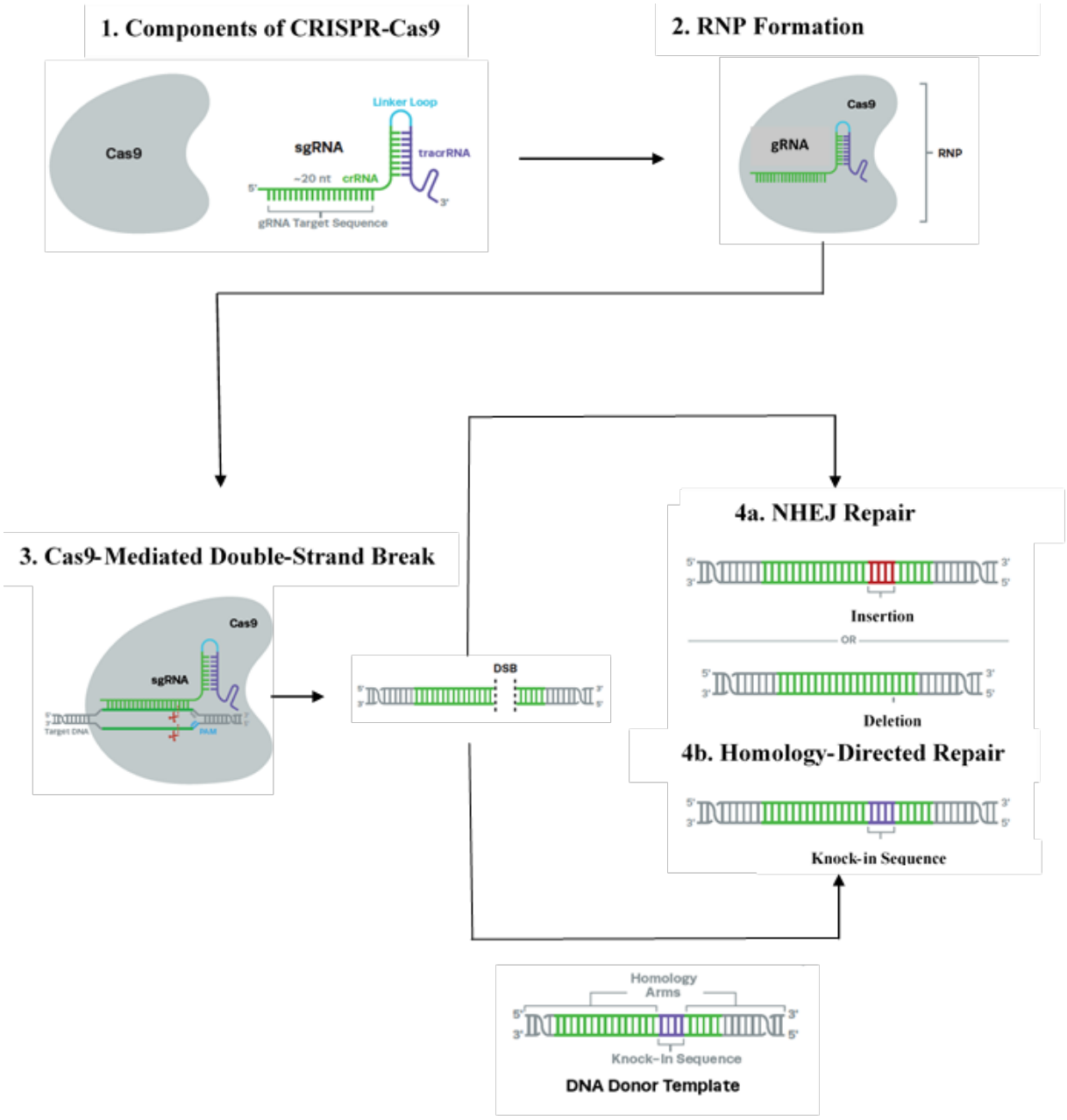

Figure 1.9. CRISPR-Cas9 genome editing mechanism. **1.** The components of CRISPR-Cas9 consists of a Cas9 protein and gRNA. The Cas9 is an enzyme with DNA endonuclease activity that act as a pair of molecular scissors that cut two strands of DNA at a specific location so that part of the genome can be added or removed. The gRNA is a pre-designed RNA sequence fragment located within a longer RNA scaffold. The gRNA contains about a 20-base pair sequence that is complimentary to the genomic target and is designed to find and bind to a specific sequence in the target DNA. The Protospacer Adjacent Motif (PAM) is a short sequence of nucleotides downstream of the target DNA and is required for the gRNA to bind to the target sequence. The

PAM for Cas9 is 5'-NGG-3', where N is any nucleotide. **2.** The RNP complex formation: Cas9 protein and gRNA form RNP. **3.** Cas-mediated double-strand break: the specific gRNA sequence is designed to find and bind the target DNA in the nucleus of the cell. The Cas9 follows the gRNA to the same location in the DNA sequence and forms an RNP complex. Cas9 then cleaves both strands of the DNA. This creates a double strand break at the genomic target. At this stage, the cell recognizes that there is a problem and DNA repair mechanisms are activated. **4.** Two endogenous repair mechanisms: 4a. NHEJ repair is the process that insert or delete nucleotides. 4b. Homology-directed repair is the process that add a desired DNA template to the broken sequence via homology-directed repair, reproduced with permission from *Synthego* [164].

1.8.4. Preparation and Characterization of SR-A1 Knockout Macrophages Using CRISPR-Cas9

A SR-A1 knockout RAW 264.7 cell pool was generated using CRISPR-Cas9 technologies with the guide RNA sequence CAGCAUCCUCUCGUUCAUGA and PAM sequence GGG. Synthego validated, via an inference CRISPR edits (ICE) method, that 70% of the SR-A1 knockout pool of RAW 264.7 cells had an insertion(s) or deletion(s) between the base pairs 41 and 42 of the SR-A1 gene. Because the site of alteration is at the beginning of the gene, expression of SR-A1.1, which is a splice variant of SR-A1, would also be affected, an advantage as both forms of SR-A1 would likely be nonfunctional. A dilution scheme was used to clone cells that did not express SR-A1 receptors on their surface. Serial dilutions of the SR-A1 knockout RAW 264.7 cell pool were plated in 96-well plates and incubated for 7 days. Cells that had arisen from a single colony were grown for several passages before selecting clones that lacked surface SR-A1 expression using immunofluorescence microscopy and flow cytometry. SR-A1 knockout RAW 264.7 cell clones were used in Chapter 3 to study the interaction of BSA-MWNTs with macrophages and to identify the receptor(s) for BSA-MWNTs, as detailed in section 1.9.

1.9. OVERVIEW OF DOCTORAL RESEARCH PROJECTS

The purpose of this research project was to assess the physicochemical properties of NanoAmor CVD-synthesized pMWNTs and cMWNTs and to study the biological responses of macrophages to cMWNTs and pMWNTs. Chapter 2 presents a comprehensive physicochemical characterization of two lots of commercial, CVD-synthesized pMWNTs and cMWNTs. In Chapter 3, these well-characterized MWNTs were coated with BSA and their interaction with macrophages was studied using a direct binding assay under highly controlled conditions where the influence of MWNT functionalization and the protein coat could be investigated. The binding and uptake of MWNTs by macrophages was investigated, and most importantly, on whether the MWNT receptors present on macrophages have critical roles in the pathogenesis of MWNTs. More detailed overviews of Chapters 2 and 3 are presented next.

Chapter 2, published in 2020 (Huynh, M.T., et al, 2020. The Importance of Evaluating the Lot-to-Lot Batch Consistency of Commercial Multi-Walled Carbon Nanotube Products. *Nanomaterials*. 10:1930.), describes a comprehensive physicochemical characterization of two lots of NanoAmor CVD-synthesized pMWNTs and cMWNTs (one lot of each type purchased in 2015 and the second one in 2018) that were used to study the biological response of macrophages to MWNTs. It was important to evaluate the two different production lots of the same MWNT product since the high degree of variability in the physicochemical properties of MWNTs (e.g., composition and impurity content, dimensions and surface topography, crystallinity and types of defects, and agglomeration states to name a few) makes it difficult to assess the EH&S risks of MWNTs and other carbon nanomaterials [130,165-168]. In this study, a detailed physicochemical characterization of two commercial lots of CVD-synthesized pMWNTs and cMWNTs revealed

many similarities between the two cMWNT products and several key differences between the two pMWNT products. The 2018-pMWNTs displayed less oxidative stability, a higher defect density, and had a smaller amount of surface oxygen species relative to the 2015-pMWNTs. Additionally, the concentration of pMWNTs that could be suspended by BSA with the 2018-pMWNTs was significantly lower than for the 2015-pMWNTs. Most importantly, whereas the 24-h proliferation of RAW 264.7 macrophages cultured with BSA-suspensions of 2015-pMWNTs were statistically similar to the proliferation of cells observed with the two BSA-cMWNT suspensions, the 24-h proliferation of RAW 264.7 cells incubated with BSA-suspensions of 2018-pMWNTs was not. Specifically, the 24-h proliferation of cells incubated with BSA-suspensions of 2018-pMWNTs at 100 μg/mL was ~20% lower relative to the BSA-suspensions of 2015-pMWNTs at 100 μg/mL, even though the amount of the 2018-pMWNTs accumulated by cells was ~16% less relative to the amount of 2015-pMWNTs accumulated by cells. Also, a 72-h IC-50 of ~90 μg pMWNTs/mL was determined for RAW 264.7 cells with BSA-suspensions of 2018-pMWNTs, making the 2018-pMWNTs significantly more toxic than the 2015-pMWNTs. Furthermore, the data from this chapter would assist in providing evidence for Chapter 3 that the major similarities of the pMWNTs and cMWNTs were their outer and inner diameters, and the only major difference between the pMWNTs and cMWNTs used was the surface oxygen groups. These results demonstrate that subtle physicochemical differences can lead to significantly dissimilar cellular responses, and that production-lot consistency must be considered when assessing the toxicity of MWNTs.

Chapter 3, published in 2021 (Huynh, M.T.; et al., 2021. Scavenger Receptor A1 Mediates the Uptake of Carboxylated and Pristine Multi-Walled Carbon Nanotubes Coated with Bovine

Serum Albumin. *Nanomaterials.* 11: 539.), focuses on the interaction of BSA-coated cMWNTs and pMWNTs with CHO cells that ectopically express SR-A1 and with RAW 264.7 cells that were deleted for SR-A1 expression by CRISPR-Cas9 technology using a direct binding assay under highly controlled conditions. The major finding was that whereas PF108-coated pMWNTs do not bind to macrophages, BSA-pMWNTs do bind, suggesting that a BSA corona confers the ability of pMWNTs to bind to macrophages. The binding and accumulation of both BSA-pMWNTs and BSA-cMWNTs to the cell surface was a dose-dependent and saturable function of the applied MWNT concentration. Wild-type RAW 264.7 cells bound and accumulated approximately 2 times more BSA-cMWNTs than BSA-pMWNTs. These data suggest that there are more binding sites on the cell surface for BSA-cMWNTs than BSA-pMWNTs. However, SR-A1 knockout RAW 264.7 cells did not bind and accumulate a significant amount of either BSA-pMWNTs or cMWNTs. Further, CHO cells expressing SR-A1, but not wild-type CHO cells, accumulated both BSA-coated cMWNTs and pMWNTs. Together, these data strongly suggest that SR-A1 significantly contributes to the binding and uptake of both BSA-coated pMWNTs and cMWNTs. A model is presented that accounts for the differences in binding capacity and explains how BSA-pMWNTs and cMWNTs interact with SR-A1.

1.10. REFERENCES

1. Ramos, A.P.; Cruz, M.A.; Tovani, C.B.; Ciancaglini, P. Biomedical applications of nanotechnology. *Biophys. Rev.* **2017**, *9*, 79-89.

2. Bhardwaj, V.; Kaushik, A. Biomedical applications of nanotechnology and nanomaterials. *Micromachines*: **2017,** *8***,** 298 (3 pp.)**.**

3. Barui, A.K.; Kotcherlakota, R.; Patra, C.R. Biomedical applications of zinc oxide nanoparticles. In *Inorganic frameworks as smart nanomedicines*, Elsevier: **2018**; pp. 239-278.

4. Zahin, N.; Anwar, R.; Tewari, D.; Kabir, M.T.; Sajid, A.; Mathew, B.; Uddin, M.S.; Aleya, L.; Abdel-Daim, M.M. Nanoparticles and its biomedical applications in health and diseases: special focus on drug delivery. *Environ. Sci. Pol. Res.* **2019**, 1-18.

5. Bharathala, S.; Sharma, P. Biomedical Applications of Nanoparticles. In *Nanotechnology in Modern Animal Biotechnology*, Elsevier: **2019**; pp. 113-132.

6. Bhat, M.A.; Nayak, B.; Nanda, A.; Lone, I.H. Nanotechnology, metal nanoparticles, and biomedical applications of nanotechnology. In *Oncology: Breakthroughs in Research and Practice*, IGI Global: **2017**; pp. 311-341.

7. Chauhan, V.; Singh, V.; Tiwari, A. Applications of nanotechnology in forensic investigation. *Int. J. Life-Sci. Sci. Res.* **2017**, *3*, 1047-1051.

8. Liu, X.; Dai, L. Carbon-based metal-free catalysts. *Nat. Rev. Mater.* **2016**, *1*, 1-12.

9. Paul, R.; Zhu, L.; Chen, H.; Qu, J.; Dai, L. Recent Advances in Carbon-Based Metal-Free Electrocatalysts. *Adv. Mater.* **2019**, *31*, 1806403.

10. Zhao, S.; Lu, X.; Wang, L.; Gale, J.; Amal, R. Carbon-based metal-free catalysts for electrocatalytic reduction of nitrogen for synthesis of ammonia at ambient conditions. *Adv. Mater.* **2019**, *31*, 1805367 (9 pp.).

11. Iijima, S. Helical microtubules of graphitic carbon. *Nature* **1991**, *354*, 56-58.

12. Green, M.J.; Behabtu, N.; Pasquali, M.; Adams, W.W. Nanotubes as polymers. *Polymer* **2009**, *50*, 4979-4997.

13. Grobert, N. Carbon nanotubes–becoming clean. *Mater. Today* **2007**, *10*, 28-35.

14. Grady, B.P. *Carbon nanotube-polymer composites: Manufacture, properties, and applications*; John Wiley & Sons: 2011.

15. Martins-Júnior, P.; Alcântara, C.; Resende, R.; Ferreira, A. Carbon nanotubes: Directions and perspectives in oral regenerative medicine. *J. Dent. Res.* **2013**, *92*, 575-583.

16. Thess, A.; Lee, R.; Nikolaev, P.; Dai, H.; Petit, P.; Robert, J.; Xu, C.; Lee, Y.H.; Kim, S.G.; Rinzler, A.G. Crystalline ropes of metallic carbon nanotubes. *Science* **1996**, *273*, 483-487.

17. Chico, L.; Crespi, V.H.; Benedict, L.X.; Louie, S.G.; Cohen, M.L. Pure carbon nanoscale devices: nanotube heterojunctions. *Phys. Rev. Lett.* **1996**, *76*, 971.

18. Ajayan, P.; Ebbesen, T. Nanometre-size tubes of carbon. *Reports on Progress in Physics* **1997**, *60*, 1025-1062.

19. Duesberg, G.; Burghard, M.; Muster, J.; Philipp, G. Separation of carbon nanotubes by size exclusion chromatography. *Chem. Commun.* **1998**, 435-436.

20. De Volder, M.F.; Tawfick, S.H.; Baughman, R.H.; Hart, A.J. Carbon nanotubes: present and future commercial applications. *Science* **2013**, *339*, 535-539.

21. Ganesh, E. Single walled and multi walled carbon nanotube structure, synthesis and applications. *Int. J. Innovative Technol. Explor. Eng.* **2013**, *2*, 311-320.

22. Dresselhaus, G.; Dresselhaus, M.S.; Saito, R. Physical properties of carbon nanotubes; *World Scientific*: **1998**.

23. Baughman, R.H.; Zakhidov, A.A.; De Heer, W.A. Carbon nanotubes--the route toward applications. *Science* **2002**, *297*, 787-792.

24. Dresselhaus, M.; Thomas, I. Alternative energy technologies. *Nature* **2001**, *414*, 332-337.

25. Hamadan, N.; Sawada, S.; Oshjyama, A. New one-dimensional conductors: Graphitic microtubules. *Phys. Rev. Lett.* **1992**, *68*, 1579-1581.

26. Pop, E.; Mann, D.; Wang, Q.; Goodson, K.; Dai, H. Thermal conductance of an individual single-wall carbon nanotube above room temperature. *Nano Lett.* **2006**, *6*, 96-100.

27. Berber, S.; Kwon, Y.-K.; Tománek, D. Unusually high thermal conductivity of carbon nanotubes. *Phys. Rev. Lett.* **2000**, *84*, 4613.

28. Che, J.; Cagin, T.; Goddard III, W.A. Thermal conductivity of carbon nanotubes. *Nanotechnology* **2000**, *11*, 65-69.

29. Zhang, Q.; Chen, G.; Yoon, S.; Ahn, J.; Wang, S.; Zhou, Q.; Wang, Q.; Li, J. Thermal conductivity of multiwalled carbon nanotubes. *Phys. Rev. B* **2002**, *66*, 165440 (6 pp.).

30. Hone, J.; Whitney, M.; Piskoti, C.; Zettl, A. Thermal conductivity of single-walled carbon nanotubes. *Phys. Rev. B* **1999**, *59*, R2514-2516.

31. Muralidharan, N.; Teblum, E.; Westover, A.S.; Schauben, D.; Itzhak, A.; Muallem, M.; Nessim, G.D.; Pint, C.L. Carbon nanotube reinforced structural composite supercapacitor. *Sci. Reports* **2018**, *8*, 1-9.

32. Yadav, M.D.; Dasgupta, K.; Patwardhan, A.W.; Joshi, J.B. High Performance Fibers from Carbon Nanotubes: Synthesis, Characterization, and Applications in Composites: A Review. *Indus. Eng. Chem. Res.* **2017**, *56*, 12407-12437.

33. Li, M.; Wang, Z.; Liu, Q.; Wang, S.; Gu, Y.; Li, Y.; Zhang, Z. Carbon nanotube film/epoxy composites with high strength and toughness. *Polym. Compos.* **2017**, *38*, 588-596.

34. Janas, D.; Koziol, K. A review of production methods of carbon nanotube and graphene thin films for electrothermal applications. *Nanoscale* **2014**, *6*, 3037-3045.

35. Zaporotskova, I.V.; Boroznina, N.P.; Parkhomenko, Y.N.; Kozhitov, L.V. Carbon nanotubes: Sensor properties. A review. *Modern Electron. Mater.* **2016**, *2*, 95-105.

36. Camilli, L.; Passacantando, M. Advances on sensors based on carbon nanotubes. *Chemosensors* **2018**, *6*, 62.

37. Schroeder, V.; Savagatrup, S.; He, M.; Lin, S.; Swager, T.M. Carbon nanotube chemical sensors. *Chem. Rev.* **2018**, *119*, 599-663.

38. Sun, L.; Wang, X.; Wang, Y.; Zhang, Q. Roles of carbon nanotubes in novel energy storage devices. *Carbon* **2017**, *122*, 462-474.

39. Kumar, S.; Nehra, M.; Kedia, D.; Dilbaghi, N.; Tankeshwar, K.; Kim, K.-H. Carbon nanotubes: A potential material for energy conversion and storage. *Progress in Energy and Combustion Science* **2018**, *64*, 219-253.

40. Lu, Z.; Raad, R.; Safaei, F.; Xi, J.; Liu, Z.; Foroughi, J. Carbon nanotube based fiber supercapacitor as wearable energy storage. *Front. Mater.* **2019**, *6*, 138 (14 pp.).

41. Kaur, J.; Gill, G.S.; Jeet, K. Applications of carbon nanotubes in drug delivery: a comprehensive review. In *Characterization and biology of nanomaterials for drug delivery*, Elsevier: **2019**; pp. 113-135.

42. Sharma, P.; Kumar Mehra, N.; Jain, K.; Jain, N. Biomedical applications of carbon nanotubes: a critical review. *Curr. Drug Delivery* **2016**, *13*, 796-817.

43. Saliev, T. The advances in biomedical applications of carbon nanotubes. *J. Carbon Res.* **2019**, *5*, 29 (22 pp.).

44. Guo, Q.; Shen, X..; Li, Y.; Xu, S. Carbon nanotubes-based drug delivery to cancer and brain. *Curr. Med. Sci.* **2017**, *37*, 635-641.

45. Negri, V.; Pacheco-Torres, J.; Calle, D.; López-Larrubia, P. Carbon nanotubes in biomedicine. *Topics Curr. Chem.* **2020**, *378*, 15 (41 pp.).

46. Dizaji, B.F.; Khoshbakht, S.; Farboudi, A.; Azarbaijan, M.H.; Irani, M. Far-reaching advances in the role of carbon nanotubes in cancer therapy. *Life Sci.* **2020**, *257*, 118059 (27 pp.).

47. Pei, B.; Wang, W.; Dunne, N.; Li, X. Applications of Carbon Nanotubes in Bone Tissue Regeneration and Engineering: Superiority, Concerns, Current Advancements, and Prospects. *Nanomaterials* **2019**, *9*, 1501(39 pp.).

48. Redondo-Gómez, C.; Leandro-Mora, R.; Blanch-Bermúdez, D.; Espinoza-Araya, C.; Hidalgo-Barrantes, D.; Vega-Baudrit, J. Recent Advances in Carbon Nanotubes for Nervous Tissue Regeneration. *Adv. Polym. Technol.* **2019**, 2020 (16 pp.).

49. Schadler, L.S. Polymer-based and polymer-filled nanocomposites. *Nanocompos. Sci. Technol.* **2003**, 77-153.

50. Liné, C.; Larue, C.; Flahaut, E. Carbon nanotubes: Impacts and behaviour in the terrestrial ecosystem-A review. *Carbon* **2017**, *123*, 767-785.

51. Narei, H.; Ghasempour, R.; Akhavan, O. Toxicity and safety issues of carbon nanotubes. In *Carbon Nanotube-Reinforced Polymers*, Elsevier: **2018**; pp. 145-171.

52. Chen, M.; Zhou, S.; Zhu, Y.; Sun, Y.; Zeng, G.; Yang, C.; Xu, P.; Yan, M.; Liu, Z.; Zhang, W. Toxicity of carbon nanomaterials to plants, animals and microbes: Recent progress from 2015-present. *Chemosphere* **2018**, *206*, 255-264.

53. Kane, A.B.; Hurt, R.H.; Gao, H. The asbestos-carbon nanotube analogy: an update. *Toxicol. Appl. Pharmacol.* **2018**, *361*, 68-80.

54. Francis, A.P.; Devasena, T. Toxicity of carbon nanotubes: A review. *Toxicol. Indus. Health* **2018**, *34*, 200-210.

55. Mohanta, D.; Patnaik, S.; Sood, S.; Das, N. Carbon nanotubes: Evaluation of toxicity at biointerfaces. *J. Pharm. Anal.* **2019**, *9*, 293-300.

56. Prajapati, S.K.; Malaiya, A.; Kesharwani, P.; Soni, D.; Jain, A. Biomedical applications and toxicities of carbon nanotubes. *Drug Chem. Toxicol.* **2020**, 1-16.

57. Takagi, A.; Hirose, A.; Nishimura, T.; Fukumori, N.; Ogata, A.; Ohashi, N.; Kitajima, S.; Kanno, J. Induction of mesothelioma in p53+/- mouse by intraperitoneal application of multi-wall carbon nanotube. *J. Toxicol. Sci.* **2008**, *33*, 105-116.

58. Poland, C.A.; Duffin, R.; Kinloch, I.; Maynard, A.; Wallace, W.A.; Seaton, A.; Stone, V.; Brown, S.; MacNee, W.; Donaldson, K. Carbon nanotubes introduced into the abdominal cavity of mice show asbestos-like pathogenicity in a pilot study. *Nat. Nanotechnol.* **2008**, *3*, 423-428.

59. Manke, A.; Luanpitpong, S.; Dong, C.; Wang, L.; He, X.; Battelli, L.; Derk, R.; Stueckle, T.A.; Porter, D.W.; Sager, T. Effect of fiber length on carbon nanotube-induced fibrogenesis. *Int. J. Mol. Sci.* **2014**, *15*, 7444-7461.

60. Chen, T.; Nie, H.; Gao, X.; Yang, J.; Pu, J.; Chen, Z.; Cui, X.; Wang, Y.; Wang, H.; Jia, G. Epithelial–mesenchymal transition involved in pulmonary fibrosis induced by multi-

walled carbon nanotubes via TGF-beta/Smad signaling pathway. *Toxicol. Lett.* **2014**, *226*, 150-162.

61. Fukushima, S.; Kasai, T.; Umeda, Y.; Ohnishi, M.; Sasaki, T.; Matsumoto, M. Carcinogenicity of multi-walled carbon nanotubes: challenging issue on hazard assessment. *J. Occupat. Health* **2017**, *60*, 10-30.

62. Brown, D.; Kinloch, I.; Bangert, U.; Windle, A.; Walter, D.; Walker, G.; Scotchford, C.; Donaldson, K.; Stone, V. An in vitro study of the potential of carbon nanotubes and nanofibres to induce inflammatory mediators and frustrated phagocytosis. *Carbon* **2007**, *45*, 1743-1756.

63. Donaldson, K.; Murphy, F.A.; Duffin, R.; Poland, C.A. Asbestos, carbon nanotubes and the pleural mesothelium: a review of the hypothesis regarding the role of long fibre retention in the parietal pleura, inflammation and mesothelioma. *Part. and Fibre Toxicol.* **2010**, *7*, 5 (17 pp.).

64. Murphy, F.A.; Poland, C.A.; Duffin, R.; Al-Jamal, K.T.; Ali-Boucetta, H.; Nunes, A.; Byrne, F.; Prina-Mello, A.; Volkov, Y.; Li, S. Length-dependent retention of carbon nanotubes in the pleural space of mice initiates sustained inflammation and progressive fibrosis on the parietal pleura. *The American J. Pathol.* **2011**, *178*, 2587-2600.

65. Love, S.A.; Maurer-Jones, M.A.; Thompson, J.W.; Lin, Y.-S.; Haynes, C.L. Assessing nanoparticle toxicity. *Annu. Rev. of Anal. Chem.* **2012**, *5*, 181-205.

66. Shvedova, A.; Kagan, V. The role of nanotoxicology in realizing the 'helping without harm paradigm of nanomedicine: lessons from studies of pulmonary effects of single-walled carbon nanotubes. *J. Inter. Med.* **2010**, *267*, 106-118.

67. Wang, J.; Ma, X.; Fang, G.; Pan, M.; Ye, X.; Wang, S. Preparation of iminodiacetic acid functionalized multi-walled carbon nanotubes and its application as sorbent for separation and preconcentration of heavy metal ions. *J. Hazard. Mater.* **2011**, *186*, 1985-1992.

68. Fenoglio, I.; Greco, G.; Tomatis, M.; Muller, J.; Raymundo-Pinero, E.; Béguin, F.; Fonseca, A.; Nagy, J.B.; Lison, D.; Fubini, B. Structural defects play a major role in the acute lung toxicity of multiwall carbon nanotubes: physicochemical aspects. *Chem. Res. Toxicol.* **2008**, *21*, 1690-1697.

69. Muller, J.; Huaux, F.; Fonseca, A.; Nagy, J.B.; Moreau, N.; Delos, M.; Raymundo-Pinero, E.; Béguin, F.; Kirsch-Volders, M.; Fenoglio, I. Structural defects play a major role in the acute lung toxicity of multiwall carbon nanotubes: toxicological aspects. *Chem. Res. Toxicol.* **2008**, *21*, 1698-1705.

70. Zhang, T.; Tang, M.; Kong, L.; Li, H.; Zhang, T.; Zhang, S.; Xue, Y.; Pu, Y. Comparison of cytotoxic and inflammatory responses of pristine and functionalized multi-walled

carbon nanotubes in RAW 264.7 mouse macrophages. *J. Hazard. Mater.* **2012**, *219*, 203-212.

71. Wang, X.; Xia, T.; Addo Ntim, S.; Ji, Z.; Lin, S.; Meng, H.; Chung, C.-H.; George, S.; Zhang, H.; Wang, M. Dispersal state of multiwalled carbon nanotubes elicits profibrogenic cellular responses that correlate with fibrogenesis biomarkers and fibrosis in the murine lung. *ACS Nano* **2011**, *5*, 9772-9787.

72. Wang, L.; Castranova, V.; Mishra, A.; Chen, B.; Mercer, R.R.; Schwegler-Berry, D.; Rojanasakul, Y. Dispersion of single-walled carbon nanotubes by a natural lung surfactant for pulmonary in vitro and in vivo toxicity studies. *Part. Fibre Toxicol.* **2010**, *7*, 1-10.

73. Wang, X.; Xia, T.; Duch, M.C.; Ji, Z.; Zhang, H.; Li, R.; Sun, B.; Lin, S.; Meng, H.; Liao, Y.-P. Pluronic F108 coating decreases the lung fibrosis potential of multiwall carbon nanotubes by reducing lysosomal injury. *Nano Lett.* **2012**, *12*, 3050-3061.

74. Tabet, L.; Bussy, C.; Setyan, A.; Simon-Deckers, A.; Rossi, M.J.; Boczkowski, J.; Lanone, S. Coating carbon nanotubes with a polystyrene-based polymer protects against pulmonary toxicity. *Part. Fibre Toxicol.* **2011**, *8*, 3 (13 pp.).

75. Holt, B.D.; Dahl, K.N.; Islam, M.F. Differential sub-cellular processing of single-wall carbon nanotubes via interfacial modifications. *J. Mater. Chem. B* **2015**, *3*, 6274-6284.

76. Wang, R.; Mikoryak, C.; Chen, E.; Li, S.; Pantano, P.; Draper, R.K. Gel electrophoresis method to measure the concentration of single-walled carbon nanotubes extracted from biological tissue. *Anal. Chem.* **2009**, *81*, 2944-2952.

77. Draper, R.K.; Pantano, P.; Wang, R.-H.; Mikoryak, C. Method for measuring carbon nanotubes taken-up by a plurality of living cells. Google Patents: **2014**.

78. Pantano, P.; Draper, R.K.; Mikoryak, C.; Wang, R. Electrophoretic methods to quantify carbon nanotubes in biological cells. *Handbook of Carbon Nano Materials* **2012**, 83-106.

79. Gordon, S. Pattern recognition receptors: doubling up for the innate immune response. *Cell* **2002**, *111*, 927-930.

80. Grassin-Delyle, S.; Abrial, C.; Salvator, H.; Brollo, M.; Naline, E.; Devillier, P. The role of toll-like receptors in the production of cytokines by human lung macrophages. *J. Innate Immunity* **2020**, *12*, 63-73.

81. Valacchi, G.; Sticozzi, C.; Lim, Y.; Pecorelli, A. Scavenger receptor class B type I: a multifunctional receptor. *Annals of the New York Academy of Sciences* **2011**, *1229*, E1-E7.

82. Kelley, J.L.; Ozment, T.R.; Li, C.; Schweitzer, J.B.; Williams, D.L. Scavenger receptor-A (CD204): a two-edged sword in health and disease. *Critical Rev. in Immunol.* **2014**, *34*, 241-261.

83. Zani, I.A.; Stephen, S.L.; Mughal, N.A.; Russell, D.; Homer-Vanniasinkam, S.; Wheatcroft, S.B.; Ponnambalam, S. Scavenger receptor structure and function in health and disease. *Cells* **2015**, *4*, 178-201.

84. PrabhuDas, M.R.; Baldwin, C.L.; Bollyky, P.L.; Bowdish, D.M.; Drickamer, K.; Febbraio, M.; Herz, J.; Kobzik, L.; Krieger, M.; Loike, J. A consensus definitive classification of scavenger receptors and their roles in health and disease. *J. Immunol.* **2017**, *198*, 3775-3789.

85. Shen, W.-J.; Asthana, S.; Kraemer, F.B.; Azhar, S. Scavenger receptor B type 1: expression, molecular regulation, and cholesterol transport function. *J. Lipid Res.* **2018**, *59*, 1114-1131.

86. Bournazos, S.; DiLillo, D.J.; Ravetch, J.V. The role of Fc–FcγR interactions in IgG-mediated microbial neutralization. *J. Experiment. Med.* **2015**, *212*, 1361-1369.

87. Bournazos, S.; Gupta, A.; Ravetch, J.V. The role of IgG Fc receptors in antibody-dependent enhancement. *Nature Rev. Immunol.* **2020**, *20*, 633-643.

88. Ross, G.D. Regulation of the Adhesion versus Cytotoxic Functions of the Mac-1/CR3/α M β 2-lntegrin Glycoprotein. *Critical Reviews™ in Immunology* **2000**, 20.

89. Ricklin, D.; Reis, E.S.; Lambris, J.D. Complement in disease: a defence system turning offensive. *Nature Rev. Nephrol.* **2016**, *12*, 383-401.

90. Vorup-Jensen, T.; Jensen, R.K. Structural immunology of complement receptors 3 and 4. *Front. in Immunol.* **2018**, *9*, 2716 (20 pp.).

91. Triantafilou, M.; Triantafilou, K. Lipopolysaccharide recognition: CD14, TLRs and the LPS-activation cluster. *Trends in Immunol.* **2002**, *23*, 301-304.

92. Vaure, C.; Liu, Y. A comparative review of toll-like receptor 4 expression and functionality in different animal species. *Front. in Immunol.* **2014**, *5*, 316 (15 pp.).

93. Kawasaki, T.; Kawai, T. Toll-like receptor signaling pathways. *Front. in Immunol.* **2014**, *5*, 461 (8 pp.).

94. Van Die, I.; Cummings, R.D. The mannose receptor in regulation of helminth-mediated host immunity. *Front. in Immunol.* **2017**, *8*, 1677 (9 pp.).

95. Underhill, D.M.; Goodridge, H.S. Information processing during phagocytosis. *Nature Rev. Immunol.* **2012**, *12*, 492-502.

96. Flannagan, R.S.; Jaumouillé, V.; Grinstein, S. The cell biology of phagocytosis. *Annual Review of Pathology: Mechanisms of Disease* **2012**, *7*, 61-98.

97. Kotchey, G.P.; Zhao, Y.; Kagan, V.E.; Star, A. Peroxidase-mediated biodegradation of carbon nanotubes in vitro and in vivo. *Adv. Drug Delivery Rev.* **2013**, *65*, 1921-1932.

98. Kagan, V.E.; Kapralov, A.A.; St. Croix, C.M.; Watkins, S.C.; Kisin, E.R.; Kotchey, G.P.; Balasubramanian, K.; Vlasova, I.I.; Yu, J.; Kim, K. Lung macrophages "digest" carbon nanotubes using a superoxide/peroxynitrite oxidative pathway. *ACS Nano* **2014**, *8*, 5610-5621.

99. Hou, J.; Wan, B.; Yang, Y.; Ren, X.-M.; Guo, L.-H.; Liu, J.-F. Biodegradation of single-walled carbon nanotubes in macrophages through respiratory burst modulation. *Int. J. Mol. Sci.* **2016**, *17*, 409 (18 pp.).

100. Yang, M.; Zhang, M.; Nakajima, H.; Yudasaka, M.; Iijima, S.; Okazaki, T. Time-dependent degradation of carbon nanotubes correlates with decreased reactive oxygen species generation in macrophages. *Int. J. Nanomed.* **2019**, *14*, 2797 (11 pp.).

101. Lee, Y.; Geckeler, K.E. Carbon nanotubes in the biological interphase: the relevance of noncovalence. *Adv. Mater.* **2010**, *22*, 4076-4083.

102. Costa, P.M.; Bourgognon, M.; Wang, J.T.; Al-Jamal, K.T. Functionalised carbon nanotubes: From intracellular uptake and cell-related toxicity to systemic brain delivery. *J. Controlled Release* **2016**, *241*, 200-219.

103. Marangon, I.; Boggetto, N.; Ménard-Moyon, C.c.; Venturelli, E.; Béoutis, M.-L.; Péchoux, C.; Luciani, N.; Wilhelm, C.; Bianco, A.; Gazeau, F. Intercellular carbon nanotube translocation assessed by flow cytometry imaging. *Nano Lett.* **2012**, *12*, 4830-4837.

104. Cui, X.; Wan, B.; Yang, Y.; Ren, X.; Guo, L.-H. Length effects on the dynamic process of cellular uptake and exocytosis of single-walled carbon nanotubes in murine macrophage cells. *Scientific Reports* **2017**, *7*, 1-13.

105. Pantarotto, D.; Briand, J.-P.; Prato, M.; Bianco, A. Translocation of bioactive peptides across cell membranes by carbon nanotubes. *Chem. Commun.* **2004**, 16-17.

106. Liu, S.; Wei, L.; Hao, L.; Fang, N.; Chang, M.W.; Xu, R.; Yang, Y.; Chen, Y. Sharper and faster "nano darts" kill more bacteria: a study of antibacterial activity of individually dispersed pristine single-walled carbon nanotube. *ACS Nano* **2009**, *3*, 3891-3902.

107. Yaron, P.N.; Holt, B.D.; Short, P.A.; Lösche, M.; Islam, M.F.; Dahl, K.N. Single wall carbon nanotubes enter cells by endocytosis and not membrane penetration. *J. Nanobiotechnol.* **2011**, *9*, 45 (15 pp.).

108. Zhao, F.; Zhao, Y.; Liu, Y.; Chang, X.; Chen, C.; Zhao, Y. Cellular uptake, intracellular trafficking, and cytotoxicity of nanomaterials. *Small* **2011**, *7*, 1322-1337.

109. Antonelli, A.; Serafini, S.; Menotta, M.; Sfara, C.; Pierigé, F.; Giorgi, L.; Ambrosi, G.; Rossi, L.; Magnani, M. Improved cellular uptake of functionalized single-walled carbon nanotubes. *Nanotechnology* **2010**, *21*, 425101 (14 pp.).

110. Li, R.; Wang, X.; Ji, Z.; Sun, B.; Zhang, H.; Chang, C.H.; Lin, S.; Meng, H.; Liao, Y.-P.; Wang, M. Surface charge and cellular processing of covalently functionalized multiwall carbon nanotubes determine pulmonary toxicity. *ACS Nano* **2013**, *7*, 2352-2368.

111. Wang, M.; Yu, S.; Wang, C.; Kong, J. Tracking the endocytic pathway of recombinant protein toxin delivered by multiwalled carbon nanotubes. *ACS Nano* **2010**, *4*, 6483-6490.

112. Kam, N.W.S.; Dai, H. Carbon nanotubes as intracellular protein transporters: generality and biological functionality. *J. American Chem. Soc.* **2005**, *127*, 6021-6026.

113. Vroman, L.; Adams, A.; Fischer, G.; Munoz, P. Interaction of high molecular weight kininogen, factor XII, and fibrinogen in plasma at interfaces. *Blood* **1980**, *55*, 156-159.

114. Vroman, L.; Adams, A.L. Identification of rapid changes at plasma–solid interfaces. *J. Biomed. Mater. Res.* **1969**, *3*, 43-67.

115. Vroman, L.; Lukosevicius, A. Ellipsometer recordings of changes in optical thickness of adsorbed films associated with surface activation of blood clotting. *Nature* **1964**, *204*, 701-703.

116. Walczyk, D.; Bombelli, F.B.; Monopoli, M.P.; Lynch, I.; Dawson, K.A. What the cell "sees" in bionanoscience. *J. American Chem. Soc.* **2010**, *132*, 5761-5768.

117. Monopoli, M.P.; Walczyk, D.; Campbell, A.; Elia, G.; Lynch, I.; Baldelli Bombelli, F.; Dawson, K.A. Physical− chemical aspects of protein corona: relevance to in vitro and in vivo biological impacts of nanoparticles. *J. American Chem. Soc.* **2011**, *133*, 2525-2534.

118. Westmeier, D.; Stauber, R.H.; Docter, D. The concept of bio-corona in modulating the toxicity of engineered nanomaterials (ENM). *Toxicol. Appl. Pharmacol.* **2016**, *299*, 53-57.

119. Alberg, I.; Kramer, S.; Schinnerer, M.; Hu, Q.; Seidl, C.; Leps, C.; Drude, N.; Möckel, D.; Rijcken, C.; Lammers, T. Polymeric Nanoparticles with Neglectable Protein Corona. *Small* **2020**, *16*, 1907574 (13 pp.).

120. Rampado, R.; Crotti, S.; Caliceti, P.; Pucciarelli, S.; Agostini, M. Recent Advances in Understanding the Protein Corona of Nanoparticles and in the Formulation of "Stealthy" Nanomaterials. *Front. in Bioeng. and Biotechnol.* **2020**, *8* (19 pp.).

121. Allegri, M.; Perivoliotis, D.K.; Bianchi, M.G.; Chiu, M.; Pagliaro, A.; Koklioti, M.A.; Trompeta, A.-F.A.; Bergamaschi, E.; Bussolati, O.; Charitidis, C.A. Toxicity determinants of multi-walled carbon nanotubes: the relationship between functionalization and agglomeration. *Toxicology Reports* **2016**, *3*, 230-243.

122. Shannahan, J.H.; Brown, J.M.; Chen, R.; Ke, P.C.; Lai, X.; Mitra, S.; Witzmann, F.A. Comparison of nanotube–protein corona composition in cell culture media. *Small* **2013**, *9*, 2171-2181.

123. Mu, Q.; Liu, W.; Xing, Y.; Zhou, H.; Li, Z.; Zhang, Y.; Ji, L.; Wang, F.; Si, Z.; Zhang, B. Protein binding by functionalized multiwalled carbon nanotubes is governed by the surface chemistry of both parties and the nanotube diameter. *J. Phys. Chem. C* **2008**, *112*, 3300-3307.

124. Bai, W.; Raghavendra, A.; Podila, R.; Brown, J.M. Defect density in multiwalled carbon nanotubes influences ovalbumin adsorption and promotes macrophage activation and cD4+ T-cell proliferation. *Int. J. Nanomed.* **2016**, *11*, 4357-4371.

125. Lou, K.; Zhu, Z.; Zhang, H.; Wang, Y.; Wang, X.; Cao, J. Comprehensive studies on the nature of interaction between carboxylated multi-walled carbon nanotubes and bovine serum albumin. *Chemico-biol. Interact.* **2016**, *243*, 54-61.

126. Du, P.; Zhao, J.; Mashayekhi, H.; Xing, B. Adsorption of bovine serum albumin and lysozyme on functionalized carbon nanotubes. *J. Phys. Chem. C* **2014**, *118*, 22249-22257.

127. Zhao, X.; Liu, R.; Chi, Z.; Teng, Y.; Qin, P. New insights into the behavior of bovine serum albumin adsorbed onto carbon nanotubes: Comprehensive spectroscopic studies. *J. Phys. Chem. B* **2010**, *114*, 5625-5631.

128. Cai, X.; Ramalingam, R.; San Wong, H.; Cheng, J.; Ajuh, P.; Cheng, S.H.; Lam, Y.W. Characterization of carbon nanotube protein corona by using quantitative proteomics. *Nanomed.: Nanotechnol., Biol. and Med.* **2013**, *9*, 583-593.

129. De Paoli, S.H.; Diduch, L.L.; Tegegn, T.Z.; Orecna, M.; Strader, M.B.; Karnaukhova, E.; Bonevich, J.E.; Holada, K.; Simak, J. The effect of protein corona composition on the interaction of carbon nanotubes with human blood platelets. *Biomaterials* **2014**, *35*, 6182-6194.

130. Podila, R.; Brown, J.M. Toxicity of engineered nanomaterials: a physicochemical perspective. *J. Biochem. Mol. Toxicol.* **2013**, *27*, 50-55.

131. Jiang, W.; Wang, Q.; Qu, X.; Wang, L.; Wei, X.; Zhu, D.; Yang, K. Effects of charge and surface defects of multi-walled carbon nanotubes on the disruption of model cell membranes. *Sci. Total Environ.* **2017**, *574*, 771-780.

132. Ajdary, M.; Moosavi, M.A.; Rahmati, M.; Falahati, M.; Mahboubi, M.; Mandegary, A.; Jangjoo, S.; Mohammadinejad, R.; Varma, R.S. Health concerns of various nanoparticles: A review of their in vitro and in vivo toxicity. *Nanomaterials* **2018**, *8*, 634.

133. Zhang, Y.; Wu, L.; Jiang, C.; Yan, B. Reprogramming cellular signaling machinery using surface-modified carbon nanotubes. *Chem. Res. Toxicol.* **2015**, *28*, 296-305.

134. Zhang, Y.; Mu, Q.; Zhou, H.; Vrijens, K.; Roussel, M.; Jiang, G.; Yan, B. Binding of carbon nanotube to BMP receptor 2 enhances cell differentiation and inhibits apoptosis via regulating bHLH transcription factors. *Cell Death & Disease* **2012**, *3*, e308-e308.

135. Rybak-Smith, M.J.; Pondman, K.M.; Flahaut, E.; Salvador-Morales, C.; Sim, R.B. Recognition of carbon nanotubes by the human innate immune system. In *Carbon nanotubes for biomedical applications*, Springer: **2011**; pp. 183-210.

136. Rybak-Smith, M.J.; Sim, R.B. Complement activation by carbon nanotubes. *Adv. Drug Delivery Rev.* **2011**, *63*, 1031-1041.

137. Orecchioni, M.; Bedognetti, D.; Sgarrella, F.; Marincola, F.M.; Bianco, A.; Delogu, L.G. Impact of carbon nanotubes and graphene on immune cells. *J. Translational Med.* **2014**, *12*, 138 (11 pp.).

138. Singh, R.P.; Das, M.; Thakare, V.; Jain, S. Functionalization density dependent toxicity of oxidized multiwalled carbon nanotubes in a murine macrophage cell line. *Chem. Res. Toxicol.* **2012**, *25*, 2127-2137.

139. Wang, X.; Guo, J.; Chen, T.; Nie, H.; Wang, H.; Zang, J.; Cui, X.; Jia, G. Multi-walled carbon nanotubes induce apoptosis via mitochondrial pathway and scavenger receptor. *Toxicology in Vitro* **2012**, *26*, 799-806.

140. Dutta, D.; Sundaram, S.K.; Teeguarden, J.G.; Riley, B.J.; Fifield, L.S.; Jacobs, J.M.; Addleman, S.R.; Kaysen, G.A.; Moudgil, B.M.; Weber, T.J. Adsorbed proteins influence the biological activity and molecular targeting of nanomaterials. *Toxicol. Sci.* **2007**, *100*, 303-315.

141. Hirano, S.; Kanno, S.; Furuyama, A. Multi-walled carbon nanotubes injure the plasma membrane of macrophages. *Toxicol. Appl. Pharmacol.* **2008**, *232*, 244-251.

142. Sweeney, S.; Grandolfo, D.; Ruenraroengsak, P.; Tetley, T.D. Functional consequences for primary human alveolar macrophages following treatment with long, but not short, multiwalled carbon nanotubes. *Int. J. Nanomed.* **2015**, *10*, 3115-3129.

143. Gao, N.; Zhang, Q.; Mu, Q.; Bai, Y.; Li, L.; Zhou, H.; Butch, E.R.; Powell, T.B.; Snyder, S.E.; Jiang, G. Steering carbon nanotubes to scavenger receptor recognition by nanotube

surface chemistry modification partially alleviates NFκB activation and reduces its immunotoxicity. *ACS Nano* **2011**, *5*, 4581-4591.

144. Iancu, C.; Mocan, L.; Bele, C.; Orza, A.I.; Tabaran, F.A.; Catoi, C.; Stiufiuc, R.; Stir, A.; Matea, C.; Iancu, D. Enhanced laser thermal ablation for the in vitro treatment of liver cancer by specific delivery of multiwalled carbon nanotubes functionalized with human serum albumin. *Int. J. Nanomed.* **2011**, *6*, 129-141.

145. Goldstein, J.L.; Ho, Y.; Basu, S.K.; Brown, M.S. Binding site on macrophages that mediates uptake and degradation of acetylated low-density lipoprotein, producing massive cholesterol deposition. *Proceedings of the National Academy of Sciences* **1979**, *76*, 333-337.

146. Vetter, S.W. Glycated serum albumin and AGE receptors. In *Advances in Clinical Chemistry*, Elsevier: **2015**; *72*, pp. 205-275.

147. Doi, T.; Higashino, K.-I.; Kurihara, Y.; Wada, Y.; Miyazaki, T.; Nakamura, H.; Uesugi, S.; Imanishi, T.; Kawabe, Y.; Itakura, H. Charged collagen structure mediates the recognition of negatively charged macromolecules by macrophage scavenger receptors. *J. Biol. Chem.* **1993**, *268*, 2126-2133.

148. Andersson, L.; Freeman, M.W. Functional changes in scavenger receptor binding conformation are induced by charge mutants spanning the entire collagen domain. *J. Biol. Chem.* **1998**, *273*, 19592-19601.

149. Chen, Y.; Sankala, M.; Ojala, J.R.; Sun, Y.; Tuuttila, A.; Isenman, D.E.; Tryggvason, K.; Pikkarainen, T. A phage display screen and binding studies with acetylated low density lipoprotein provide evidence for the importance of the scavenger receptor cysteine-rich (SRCR) domain in the ligand-binding function of MARCO. *J. Biol. Chem.* **2006**, *281*, 12767-12775.

150. Ojala, J.R.; Pikkarainen, T.; Tuuttila, A.; Sandalova, T.; Tryggvason, K. Crystal structure of the cysteine-rich domain of scavenger receptor MARCO reveals the presence of a basic and an acidic cluster that both contribute to ligand recognition. *J. Biol. Chem.* **2007**, *282*, 16654-16666.

151. Whelan, F.J.; Meehan, C.J.; Golding, G.B.; McConkey, B.J.; Bowdish, D.M. The evolution of the class A scavenger receptors. *BMC Evol. Biol.* **2012**, *12*, 227 (11 pp.).

152. Goh, J.W.; Tan, Y.S.; Dodds, A.W.; Reid, K.B.; Lu, J. The class A macrophage scavenger receptor type I (SR-AI) recognizes complement iC3b and mediates NF-κB activation. *Protein & Cell* **2010**, *1*, 174-187.

153. Brännström, A.; Sankala, M.; Tryggvason, K.; Pikkarainen, T. Arginine residues in domain V have a central role for bacteria-binding activity of macrophage scavenger receptor MARCO. *Biochem. Biophys.l Res. Commun.* **2002**, *290*, 1462-1469.

154. Resnick, D.; Freedman, N.; Xu, S.; Krieger, M. Secreted extracellular domains of macrophage scavenger receptors form elongated trimers which specifically bind crocidolite asbestos. *J. Biol. Chem.* **1993**, *268*, 3538-3545.

155. Resnick, D.; Chatterton, J.E.; Schwartz, K.; Slayter, H.; Krieger, M. Structures of class A macrophage scavenger receptors electron microscopic study of flexible, multidomain, fibrous proteins and determination of the disulfide bond pattern of the scavenger receptor cysteine-rich domain. *J. Biol. Chem.* **1996**, *271*, 26924-26930.

156. Sankala, M.; Brännström, A.; Schulthess, T.; Bergmann, U.; Morgunova, E.; Engel, J.; Tryggvason, K.; Pikkarainen, T. Characterization of recombinant soluble macrophage scavenger receptor MARCO. *J. Biol. Chem.* **2002**, *277*, 33378-33385.

157. Hirano, S.; Fujitani, Y.; Furuyama, A.; Kanno, S. Macrophage receptor with collagenous structure (MARCO) is a dynamic adhesive molecule that enhances uptake of carbon nanotubes by CHO-K1 cells. *Toxicol. Appl. Pharmacol.* **2012**, *259*, 96-103.

158. Wang, R.; Lee, M.; Kinghorn, K.; Hughes, T.; Chuckaree, I.; Lohray, R.; Chow, E.; Pantano, P.; Draper, R. Quantitation of cell-associated carbon nanotubes: selective binding and accumulation of carboxylated carbon nanotubes by macrophages. *Nanotoxicology* **2018**, *12*, 677-698.

159. Wang, R.; Lohray, R.; Chow, E.; Gangupantula, P.; Smith, L.; Draper, R. Selective Uptake of Carboxylated Multi-Walled Carbon Nanotubes by Class A Type 1 Scavenger Receptors and Impaired Phagocytosis in Alveolar Macrophages. *Nanomaterials* **2020**, *10*, 2417 (29 pp.).

160. Ishino, Y.; Shinagawa, H.; Makino, K.; Amemura, M.; Nakata, A. Nucleotide sequence of the iap gene, responsible for alkaline phosphatase isozyme conversion in Escherichia coli, and identification of the gene product. *J. Bacteriol.* **1987**, *169*, 5429-5433.

161. Barrangou, R.; Fremaux, C.; Deveau, H.; Richards, M.; Boyaval, P.; Moineau, S.; Romero, D.A.; Horvath, P. CRISPR provides acquired resistance against viruses in prokaryotes. *Science* **2007**, *315*, 1709-1712.

162. Hsu, P.D.; Lander, E.S.; Zhang, F. Development and applications of CRISPR-Cas9 for genome engineering. *Cell* **2014**, *157*, 1262-1278.

163. Xiao, Q.; Guo, D.; Chen, S. Application of CRISPR/Cas9-based gene editing in HIV-1/AIDS therapy. *Front. Cellul. Infect. Microbiol.* **2019**, *9*, 69 (15 pp.).

164. Synthego. 'CRISPR 101: Your guide to understing CRISPR', *Synthego Corporation*. **2019**.

165. Boverhof, D.R.; David, R.M. Nanomaterial characterization: considerations and needs for hazard assessment and safety evaluation. *Anal. Bioanal. Chem.* **2010**, *396*, 953-961.

166. Fadeel, B.; Fornara, A.; Toprak, M.S.; Bhattacharya, K. Keeping it real: The importance of material characterization in nanotoxicology. *Biochem. and Biophys. Res.* Commun. **2015**, *468*, 498-503.

167. Gunsolus, I.L.; Haynes, C.L. Analytical aspects of nanotoxicology. *Anal. Chem.* **2016**, *88*, 451-479.

168. DeLoid, G.M.; Cohen, J.M.; Pyrgiotakis, G.; Demokritou, P. Preparation, characterization, and in vitro dosimetry of dispersed, engineered nanomaterials. *Nature Protocols* **2017**, *12*, 355-371.

169. Krug, H.F. The uncertainty with nanosafety: Validity and reliability of published data. *Colloids Surf. B: Biointerfaces* **2018**, *172*, 113-117.

CHAPTER 2

THE IMPORTANCE OF EVALUATING THE LOT-TO-LOT BATCH CONSISTENCY OF COMMERCIAL MULTI-WALLED CARBON NANOTUBE PRODUCTS

Authors – Mai T. Huynh [1], Jean Francois Veyan [2], Hong Pham [1], Raina Rahman [1], Samad Yousuf [1], Alexander Brown [1], Jason Lin [1], Kenneth J. Balkus, Jr. [1], Shashini D. Diwakara [1], Ronald A. Smaldone [1], Bryanna LeGrand [1], Carole Mikoryak [3], Rockford Draper [1,3], and Paul Pantano [1]

[1] Department of Chemistry and Biochemistry, BE 26
The University of Texas at Dallas
800 West Campbell Road, Richardson, Texas, 75080-3021

[2] Department of Materials Science and Engineering, RL 10
The University of Texas at Dallas
800 West Campbell Road, Richardson, Texas, 75080-3021

[3] Department of Biological Sciences, BSB 12
The University of Texas at Dallas
800 West Campbell Road, Richardson, Texas, 75080-3021

This chapter has been reproduced from *Nanomaterials* **2020**, *10*, 1930, doi:10.3390/nano10101930.

2.1. ABSTRACT

The biological response of multi-walled carbon nanotubes (MWNTs) is related to their physicochemical properties and a thorough MWNT characterization should accompany an assessment of their biological activity, including their potential toxicity. Beyond characterizing the physicochemical properties of MWNTs from different sources or manufacturers, it is also important to characterize different production lots of the same MWNT product from the same vendor (i.e., lot-to-lot batch consistency). Herein, we present a comprehensive physicochemical characterization of two lots of commercial pristine MWNTs (pMWNTs) and carboxylated MWNTs (cMWNTs) used to study the response of mammalian macrophages to MWNTs. There were many similarities between the physicochemical properties of the two lots of cMWNTs and neither significantly diminished the 24-h proliferation of RAW 264.7 macrophages up to the highest concentration tested (200 μg cMWNTs/mL). Conversely, several physicochemical properties of the two lots of pMWNTs were different; notably, the newer lot of pMWNTs displayed less oxidative stability, a higher defect density, and a smaller amount of surface oxygen species relative to the original lot. Furthermore, a 72-h half maximal inhibitory concentration (IC-50) of ~90 μg pMWNTs/mL was determined for RAW 264.7 cells with the new lot of pMWNTs. These results demonstrate that subtle physicochemical differences can lead to significantly dissimilar cellular responses, and that production-lot consistency must be considered when assessing the toxicity of MWNTs.

2.2. INTRODUCTION

The unique physicochemical properties of multi-walled carbon nanotubes (MWNTs) lend themselves to a variety of industrial and biomedical applications (for recent reviews, see [1–15]). However, there are environmental health and safety (EH&S) concerns associated with MWNTs because of consistent reports that they can be toxic (for recent reviews, see [16–22]). Moreover, anthropogenic MWNTs have been found in the lungs of asthmatic Parisian children not known to have been exposed to a source of MWNTs, suggesting that MWNTs may be a previously unrecognized air pollutant [23].

MWNTs are synthesized in a range of facilities from small-scale research laboratories to industrial-scale manufacturing plants whose annual production capacities can exceed hundreds of metric tons. Chemical vapor deposition (CVD) processes are the dominant modes of high-volume production because of low energy consumption, low waste generation, and the ability to tailor MWNT properties such as their outer diameters [24]. Even so, commercially available MWNTs with similar product descriptions can have varying physicochemical properties depending on the scale and parameters of the synthetic process, the stringency of quality control measures, and post-production treatments designed to remove contaminants [25–27]. For example, MWNTs are frequently purified after synthesis by oxidative treatments to remove metal particles and amorphous carbons, which can generate sp^3-defect sites and change physicochemical properties based on the exact method and conditions of the post-production treatment used [28]. Unfortunately, the high degree of variability in the physicochemical properties of MWNTs (e.g., composition and impurity content, dimensions and surface topography, crystallinity and types of defects, and agglomeration states to name a few) makes it difficult to assess the EH&S risks of

MWNTs and other carbon nanomaterials [29–34]. It is therefore not surprising that there are a large number of conflicting reports and knowledge gaps in the nanotoxicity literature concerning MWNTs (for reviews, see [20,35–40]). Toward gaining a more thorough understanding of the structure-activity relationships of MWNTs, one mantra that has gained acceptance in the nanotoxicity community is that thorough MWNT characterizations should accompany toxicity investigations, especially since no one analytical technique can probe all aspects of MWNT physicochemical properties that may correlate with a biological response [25,29,31,32,41].

For these reasons, it is not uncommon for researchers to perform extensive material characterizations of commercially obtained MWNTs and to compare their findings with the manufacturer's product specifications [26,42–45]. However, beyond the idea of assessing the physicochemical properties of MWNTs from different sources or manufacturers, is the equally important aspect of evaluating different production lots of the same MWNT product (i.e., lot-to-lot batch consistency). While this important aspect has long been endorsed for engineered nanomaterials [32,46,47], to our knowledge, there has only been one report that presents any material characterization data for different production lots of MWNTs; specifically, lots used to prepare MWNT-modified graphite electrodes [48].

Herein, we present a comprehensive physicochemical characterization of two lots of commercial, CVD-synthesized pristine MWNTs (pMWNTs) and carboxylated MWNTs (cMWNTs) used to study the biological responses of mammalian macrophages to MWNTs. There were many similarities between the physicochemical properties of the two lots of cMWNT powders and of bovine serum albumin (BSA)-coated cMWNT suspensions prepared with each cMWNT powder. Equally importantly, BSA-cMWNT suspensions prepared with the two

cMWNT powders did not significantly diminish the 24-h proliferation of RAW 264.7 macrophages up to the highest concentration tested (200 μg cMWNTs/mL). The new production lot of cMWNTs is therefore a strong candidate to be a suitable replacement for the original lot of cMWNTs when it is exhausted. Conversely, several physicochemical properties of the two lots of pMWNT powders and of the BSA-coated pMWNT suspensions prepared with each powder were different. The new pMWNTs displayed less oxidative stability, a higher defect density, and a smaller amount of surface oxygen species relative to the original lot of pMWNTs. Also, the concentration of pMWNTs that could be suspended by BSA with the new lot of pMWNTs was significantly lower relative to the original lot of pMWNTs. Most importantly, while the 24-h proliferation of RAW 264.7 macrophages cultured with the original BSA-pMWNT suspensions were statistically similar to the proliferation of cells observed with the two BSA-cMWNT suspensions, the 24-h proliferation of RAW 264.7 cells incubated with BSA-pMWNT suspensions prepared with the new pMWNTs was not. Specifically, the 24-h proliferation of cells incubated with BSA-suspensions of the new pMWNTs at 100 μg/mL was ~20% lower relative to BSA-suspensions of the original pMWNTs at 100 μg/mL, even though the amount of the new pMWNTs accumulated by cells was ~16% less relative to the amount of original pMWNTs accumulated by cells. Furthermore, a 72-h half maximal inhibitory concentration (IC-50) of ~90 μg pMWNTs/mL was determined for RAW 264.7 cells with the new lot of BSA-pMWNTs, making the 2018-pMWNTs significantly more toxic than the original pMWNT lot. These results demonstrate that subtle physicochemical differences can have a significant effect on the response of biological cells to a MWNT product, and that production-lot consistency must be considered when assessing the toxicity or biomedical performance of MWNTs.

2.3. MATERIALS AND METHODS

2.3.1. Nanomaterials, Chemicals, and Solutions

CVD-synthesized pMWNTs and cMWNTs were purchased directly from the manufacturer. The original pMWNT and cMWNT powders were acquired in 2015 and a second purchase of the exact same products was obtained in 2018; herein, they are denoted as 2015-pMWNTs, 2015-cMWNTs, 2018-pMWNTs, and 2018-cMWNTs. All MWNTs were stored at room temperature in the dark. Caution, a fine-particulate respirator and other appropriate personal protective equipment should be worn when handling dry MWNT powders. Dulbecco's modified Eagle medium (DMEM) was purchased from Gibco (Grand Island, NY, USA), fetal bovine serum (FBS) was purchased from Atlanta Biologicals (Flowery Branch, GA, USA), and BSA, penicillin (10,000 U/mL), streptomycin (10 mg/mL), and all other chemicals were purchased from Millipore Sigma (Burlington, MA); all chemicals were used as-received. Deionized water (18.3 MΩ-cm) was obtained using a Milli-Q® Integral water purification system (Billerica, MA, USA). Phosphate buffered saline (PBS; 0.8 mM phosphate, 150 mM NaCl, pH 7.4) was sterilized by autoclaving at 121 °C for 45 min. Stock solutions of 100 mg/mL BSA were prepared by dissolving 10 g of BSA in 100 mL of deionized water and adjusting the pH to 7.4. Working solutions of 0.10 mg/mL BSA were prepared by diluting stock BSA solutions with aqueous 10 mM HEPES and filtering the solutions through a 0.22-μm pore membrane; stock and working solutions of BSA were stored at 4 °C in the dark.

2.3.2. CHN/O Analyses

The elemental content of each MWNT powder was determined according to a previously described combustion analysis technique with the exception that all samples were vacuum dried

for 4 h at 100 °C prior to analysis [49]. The CHN/O analyses were performed by Micro-Analysis, Inc. (Wilmington, DE, USA) using a Perkin Elmer 2400 Series II CHN/O Analyzer. The CHN analyses were based on the Pregl-Dumas technique using a furnace temperature of 1100 °C in a 100% oxygen atmosphere. The results were reported as the percent by weight of each element with a precision of ±0.30% and a limit of detection (LOD) of <0.10%. The oxygen analysis was based on the Unterzaucher technique using a pyrolysis furnace temperature of 1100 °C and an atmosphere of 95% helium and 5% hydrogen. The results for oxygen were reported as the percent by weight with a precision of ±0.30% and a LOD of <0.10%.

2.3.3. Preparation of BSA-MWNT Suspensions

The sonication and centrifugation protocol described in our previous works [50,51] was used with slight modifications to prepare purified BSA-coated MWNT suspensions. First, 10.0 mg of pMWNT or cMWNT powder was weighed into a pre-cleaned 20-mL glass vial and baked at 200 °C for 2 h to inactivate potential endotoxin contaminants [52]. Next, 10 mL of a 0.10 mg/mL BSA working solution was added to the vial and the mixture was sonicated. Specifically, a single vial was secured in a hanging rack and sonicated for 240 min using an ultrasonic bath sonicator (Elmasonic P30H; Elma Ultrasonic, Singen, Germany) that was operated at 120 W and 37 kHz in a 4 °C cold room. During sonication, the temperature of the bath water was maintained below 18 °C by using a refrigerated water bath circulator (Isotemp 1006S). After sonication, the solution was divided by transferring 1-mL aliquots into ten 1.5-mL centrifuge tubes. One of the 1-mL aliquots of each non-centrifuged BSA-pMWNT or BSA-cMWNT suspension was set aside as the standard suspension, and the MWNT concentrations in these standards were determined by measuring the absorbance at 500 nm using a BioTek Synergy Mx plate reader (Winooski, VT,

USA). Next, each standard was serially diluted with a 0.10 mg/mL-BSA working solution to construct pMWNT or cMWNT calibration curves. The remaining nine aliquots were centrifuged at 20,000 RCF for 5 min at 4 °C using an Eppendorf 5417R centrifuge to remove heavier metal-containing MWNTs and bundles, as demonstrated in our previous work [53,54]. The top 900 µL from each supernatant was collected without disturbing the pellet and combined in a sterile vial to afford ~9 mL of a purified BSA-pMWNT or BSA-cMWNT suspension. The concentration of MWNTs in each purified suspension pool was determined using the measured absorbance at 500 nm and the calibration curves described above. Purified BSA-MWNT suspensions were stored at 4 °C in the dark.

2.3.4. Characterization of MWNT Suspensions

Dynamic light scattering (DLS) and zeta potential analyses were used as part of a quality control routine for the preparation of all MWNT suspensions, as previously described [50,51,54]. The particle size distributions, in terms of hydrodynamic diameter, of the BSA-MWNT suspensions were determined by DLS. In brief, aliquots of purified pMWNT or cMWNT suspensions were diluted 1:10 in a 0.10 mg/mL BSA working solution and analyzed with a Zetasizer Nano-ZS 3600 (Malvern Instruments, Worcestershire, UK) using a 633-nm laser and a backscatter measurement angle of 173°. The instrument was calibrated with Polybead® standards (Polysciences, Warrington, PA, USA) and ten consecutive 30-s runs were taken per measurement at 25 °C. The hydrodynamic diameter was calculated using a viscosity and refractive index of 0.8872 cP and 1.330, respectively for deionized water, and an absorption and refractive index of 0.010 and 1.891, respectively, for MWNTs. Zeta potential values were also determined for purified BSA-coated MWNT suspensions that were diluted 1:10 with deionized water. In addition,

DLS and zeta potential analyses were performed periodically on purified MWNT suspensions stored at 4 °C. Typically, MWNT suspensions were stable in storage for months, indicated by the lack of aggregates detected by DLS and constant zeta potential results.

2.3.5. Cell Culture

Abelson murine leukemia-virus transformed RAW 264.7 macrophages were purchased from the American Type Culture Collection (ATCC® TIB-71™; Manassas, VA, USA). RAW 264.7 cells were grown in DMEM supplemented with 1.5 mg/mL sodium bicarbonate, 10 mM HEPES (pH 7.4), and 10% (v/v) FBS; the standard incubation conditions were 37 °C in a 5% CO_2 and 95% air environment.

2.3.6. Crystal Violet Cell Proliferation Assay

Purified BSA-MWNT suspensions were first diluted with a freshly prepared 0.10 mg/mL-BSA working solution to a concentration twice the desired MWNT concentration to be tested. The diluted MWNT suspensions were then mixed 1:1 in equal volumes with 2X-concentrated medium that contained 3.0 mg/mL sodium bicarbonate, 20 mM HEPES (pH 7.4), 20% (*v/v*) FBS, 200 units/mL penicillin, and 0.2 mg/mL streptomycin. The result is a test medium with the same concentration of 10 mM HEPES and 10% FBS as the control medium. ~3.5×10^4 RAW 264.7 cells/well were seeded in 48-well plates and incubated at 37 °C overnight before the medium was replaced with freshly prepared control medium or test medium containing MWNTs at a specified concentration, and incubated for 24 or 72 h. At the end of the incubation, cells were washed three times with fresh medium, two times with PBS, air-dried, and fixed with 4% (*w/v*) paraformaldehyde in PBS. Cell proliferation was determined using a BioTek Synergy Mx plate reader and the standardized crystal violet assay as detailed in our previous work, where it was

demonstrated that MWNTs do not interfere with the assay [55]. The dose-response cell proliferation assay with Co^{2+} was identical to the 24-h procedure described above except that $CoCl_2$ was first diluted with a freshly prepared 0.10 mg/mL-BSA working solution to a concentration twice the desired $CoCl_2$ concentration to be tested. Statistical analyses were performed using a Student's *t*-test where $p < 0.05$ was considered statistically significant.

2.3.7. Accumulation of pMWNTs by Cells

The following procedure was used to detect the accumulation of pMWNTs by RAW 264.7 cells at 37 °C for 24 h. BSA-pMWNT suspensions were first diluted in a freshly prepared 0.10 mg/mL BSA working solution to twice the desired final MWNT concentrations specified in the experiment. The diluted BSA-pMWNT samples were then mixed 1:1 with 2X-concentrated medium. Total of ~3.5×10^5 cells/well were seeded in 6-well plates and incubated in medium at 37 °C overnight to allow the cells to adhere to the plates. The medium was removed the next day and 2 mL of the appropriate freshly prepared control medium that contained no MWNTs, or test medium that contained a 100 μg/mL pMWNT suspension, was added to each well. Cells were incubated in control or test medium at 37 °C for 24 h. At the end of the incubation, the control and test media were removed by aspiration and the cells were washed three times with fresh medium followed by two washes with PBS. Cells were then lifted off the well using 0.5 mL Accumax™, transferred to a centrifuge tube, and the well was rinsed with 1.5 mL PBS that was subsequently added to the tube to make a final cell suspension of 2 mL/well/tube. Three aliquots of cell suspension, 100 μL each, were used to determine cell counts in each sample using a Beckman Coulter particle counter (Miami, FL, USA) and the cells in the remaining 1.7-mL cell suspension were collected by centrifugation at 1000× g for 5 min at 4 °C. The cells in the pellet

were lysed in 200 μL of cell lysis buffer that contained 0.25 M Tris-HCl (pH 6.8), 8% (*w/v*) sodium dodecyl sulfate (SDS), and 20% (*v/v*) 2-mercaptoethanol. To ensure complete lysis of the cells, the lysate samples were heated in a boiling water bath for 2 h and then stored at 4 °C. The amounts of pMWNTs in the cell lysate samples were determined using a previously established SDS-polyacrylamide gel electrophoresis (SDS-PAGE) method [56], described next.

2.3.8. Quantitation of pMWNTs Extracted from Cell Lysates by SDS-PAGE

The SDS-PAGE method with optical detection, recently validated by a large-area Raman scan technique [51], was used for quantifying pMWNTs extracted from RAW 264.7 cells. In brief, aliquots of known amounts of pMWNT standard suspensions, lysates of control cells, and lysates of cells treated with BSA-pMWNTs were mixed with 5% 2-mercaptoethanol, 10% glycerol, 62.5 mM Tris-HCl, and 2X-concentrated SDS sample loading buffer to a final concentration of 2% SDS, and boiled for 3 min. Samples at various dilutions and volumes were subsequently loaded into the wells of a SDS-polyacrylamide gel composed of a 4% stacking gel on top of a 10% resolving gel. An electric current was applied at a constant 100 V for 2 h. MWNTs in standard suspensions and in the lysates bind SDS in the sample loading buffer to become negatively charged, and migrate toward the anode upon electrophoresis. The large aspect ratio of MWNTs prevents them from sieving through the pores of a 4% polyacrylamide gel mesh, thus, the MWNTs accumulate at the bottom of the sample loading well during electrophoresis and form a sharp dark band. Following electrophoresis, optical images of the gels were obtained using a flatbed scanner (HP Scanjet G3110), and the pixel intensity of each dark band was quantified using *ImageJ* software. The known amount of pMWNTs in the standards and their corresponding pixel intensities form a linear calibration curve that was used to determine the unknown amount of

pMWNTs in cell lysates, based on the pixel intensities of lysate bands loaded in the same gel as the standards. The resultant femtograms of cell-associated pMWNTs/cell were statistically analyzed using a Student's t-Test where $p < 0.05$ was considered statistically significant.

2.3.9. Inductively Coupled Plasma-Mass Spectrometry (ICP-MS)

All ICP-MS analyses were performed by Precilab, Inc. (Carrollton, TX, USA) using our previously reported acid digestion protocol [49,53]. In brief, a solution of 300 µL of 37% HCl and 100 µL of 69% HNO_3 was added to ~3.1 mg of a MWNT powder (or to 25.0 mL of a BSA-pMWNT suspension) and bath sonicated for 20 min. Next, the sample was diluted with a 2% HNO_3 blank solution to a total volume of 50.0 mL and was allowed to settle for 2 h. All metals were calibrated using blanks and standards of 0.050 ppb, 0.100 ppb, 0.250 ppb, and 0.500 ppb concentrations of the respective metals prepared from 1000 ppm standard solutions (Inorganic Ventures); the internal standard was rhodium 103. The samples and standard solutions were aspirated through a nebulizer into a torch chamber and then injected into the plasma through argon gas flow. The determination of Al, Ca, Co, Cr, Fe, Li, Mg, Mn, Ni, K, and Na was performed using a Thermo-Fisher iCap RQ ICP mass spectrometer in cool mode with a 600 W plasma energy. The determination of Ag, As, Au, B, Ba, Be, Bi, Cd, Cu, Ga, Ge, Mo, Nb, Pb, Pt, Sb, Sn, Sr, Ta, Ti, Tl, V, W, Zn, and Zr was performed using a Thermo-Fisher iCap Qs ICP mass spectrometer in hot mode with a 1550 W plasma energy and a kinetic energy discrimination collision cell to remove the chloride interference for As and V. Values are reported in ppm as the mean of n = 2 independent sub-samples and analyses.

2.3.10. Transmission Electron Microscopy (TEM)

TEM was performed using a JEOL JEM 1400 Plus transmission electron microscope (JEOL USA Inc, Peabody, MA, USA) operated at 120 kV with a lanthanum hexaboride filament as the electron source. Each MWNT powder was individually suspended in methanol by bath sonication and an aliquot of the MWNT suspension was deposited on a 300-mesh Cu lacey carbon grid (>70 images were analyzed). High-resolution TEM (HR-TEM) was performed using a JEOL JEM 2100F transmission electron microscope (JEOL USA Inc, Peabody, MA, USA) operated at 200 kV with a field-emission gun as the electron source. Each MWNT powder was individually suspended in ethanol by bath sonication and an aliquot of the MWNT suspension was deposited on a 300-mesh Cu lacey carbon grid (>220 images were analyzed). In all cases, minimized apertures and exposure times were applied to ensure that MWNTs were not damaged by the electron beam. The inside and outer diameters of MWNTs were reported as the mean $\pm$ the sample standard deviation (SD).

2.3.11. Thermogravimetric Analyses (TGA)

All TGA measurements were performed using a TA Instruments Q600 thermogravimetric analyzer (TA Instruments, Newcastle, DE, USA) using methods detailed previously [53]. In brief, ~6-mg sub-samples of a thoroughly mixed MWNT powder were transferred into the pan of the analyzer and heated from 25 °C to 800 °C or 1100 °C at 5 °C/min in ultra-pure air (~20.0% O_2/~80.0% N_2) at a flow rate of 50 mL/min. A baseline was generated for each scan and buoyancy-corrected, baseline-subtracted thermograms were converted to weight percent. Thermal oxidation temperatures were identified by the peaks from the derivatives of weight percent curves.

2.3.12. Microprobe Raman Spectroscopy

Raman spectra were acquired using a Jobin Yvon Horiba HR 800 high-resolution LabRam Raman microscope (HORIBA Jobin Yvon Inc, Edison, NJ, USA) system equipped with a 250-µm entrance slit and 1100-µm pinhole as described previously [57]. The 633-nm laser excitation was provided by a Spectra-Physics model 127 helium-neon laser operating at 20 mW. A 50×/0.5 NA LM-Plan objective was used with neutral density filter of 1.0. Spectral acquisition was performed with a 1.0-s integration time, a spectral window minimum overlap of 50, and a 3-subpixel average, each spectrum was presented as an average of three scans. Wavenumber calibration was performed using the 520.5 cm^{-1} line of a crystalline silicon wafer and the spectral resolution was ~1 cm^{-1}. A 100-µL aliquot of each type of MWNT suspension was deposited on to a crystalline silicon wafer and dried at room temperature overnight; spectra were acquired from at least seven different regions of dried material across the wafer.

2.3.13. Brunauer-Emmett-Teller (BET) Surface Area Measurements

Low-pressure gas adsorption experiments (up to 760 Torr) were carried out on a Micromeritics ASAP 2020 surface area analyzer (Micromeritics Instruments Corp., Norcross, GA, USA), as described previously [58]. All samples were degassed prior to analyses and specific surface areas were determined by a multi-point BET measurement with ultra-high purity nitrogen gas as the adsorbate and liquid nitrogen as the cryogen.

2.3.14. X-ray Diffraction (XRD)

XRD patterns were acquired at room temperature using a Rigaku Ultima IV powder X-ray diffractometer (Rigaku Americas Corporation, The Woodlands, TX, USA) equipped with a Cu Kα vacuum tube and Ni filter as previously described [59]. Individual samples of MWNT powders

were placed on a zero-background Si holder (Rigaku) and measured from 2θ = 20–60° with step sizes of 0.02° and a scan rate of 0.5°/min. The Scherrer equation was used to estimate the mean crystallite size (L_C) from the C(002) Bragg reflection.

2.3.15. X-Ray Photoelectron Spectroscopy (XPS)

XPS analysis was performed with a Physical Electronics VersaProbe II surface analysis instrument (Physical Electronics, Chanhassen, MN, USA) equipped with an Al Kα monochromatic X-ray source, as described previously [60]. The base pressure was 4×10^{-8} Pa and the electron beam power was set at 50 W (under a potential difference of 15 kV) for an irradiated area at the sample surface of 200 × 200 μm^2. MWNT powders were deposited onto a gold wafer. The photoelectrons were analyzed with a pass energy of 23.5 eV and an energy step increment of 0.2 eV/step (0.8 eV/step for survey scans). The angle between the sample surface normal and the detector (take-off angle) was set at 45° and the angle between the detector and the X-ray beam was 59°. The charge was referenced to elemental carbon at 284.8 eV. Each spectrum was plotted as an average of twenty scans.

2.3.16. Fourier Transform Infrared (FTIR) Spectroscopy

FTIR spectroscopy was performed using a nitrogen-purged, modified Thermo Nicolet 6700 infrared spectrometer (Thermo Electron Corp., Madison, WI, USA) equipped with a liquid nitrogen-cooled, broadband mercury cadmium telluride (MCT-B) detector [61]. KBr powders were first ground into ultra-fine powders and then heated overnight at 120 °C. Each MWNT powder was mixed uniformly with KBr at a ratio of 1:800, and the mixture was pressed into a pellet using a manual pellet press. Pellets were mounted into a Specac Inc. P/NH 5850c high-

pressure cell, and twenty spectra were acquired for each sample and the KBr control with a resolution of 4 cm^{-1}.

2.4. RESULTS

2.4.1. CHN/O Analyses of MWNTs

The four MWNT products were reported by the manufacturer to be >95% in purity and the two cMWNT products were reported to comprise ~2% by weight carboxylic acid groups. Lot-acceptance testing was performed using a previously described combustion analysis technique [49]. Table 2.1 shows that both pMWNT products displayed 96–97% carbon, both cMWNT products displayed ~94% carbon, all products displayed trace amounts of hydrogen, and the 2018 products displayed trace amounts of nitrogen. Overall, the combined carbon, hydrogen, nitrogen, and oxygen contents of the 2015-pMWNTs, 2015-cMWNTs, 2018-pMWNTs, and 2018-cMWNTs powders were 99.52%, 98.18%, 100.26%, and 100.11%, respectively, indicative of MWNT powders that are essentially metal-free. However, while the two 2018 products displayed higher oxygen levels, it should be noted that oxygen determinations carry a higher degree of uncertainty with hygroscopic samples such as MWNTs, which are known to adsorb atmospheric gases and moisture [62]. In a qualitative assessment of dispersibility, both cMWNT products were considered to be relatively hydrophilic because they could be stably suspended in water for >24 h following 1 h of bath sonication at 100 W and 42 kHz without a surfactant. Conversely, both pMWNT products could not be suspended in water following 1 h of sonication without a surfactant (i.e., in each case the majority of pMWNTs would sediment within <2 h). Ultimately, these initial observations, most notably, the high carbon purities, led to the decision to accept each production

lot and to move forward with the characterizations of the four BSA-coated MWNT suspensions, followed by cytotoxicity assessments, as described next.

Table 2.1. CHN/O elemental (lot-acceptance) analyses of pristine multi-walled carbon nanotube (pMWNT) and carboxylated MWNT (cMWNT) powders (n = 1 each).

Element	2015-pMWNTs (%)	2015-cMWNTs (%)	2018-pMWNTs (%)	2018-cMWNTs (%)
C	96.49	94.30	97.29	94.19
H	1.06	1.08	0.06	0.11
N	0.00	0.00	0.01	0.20
O	1.97	2.80	2.90	5.60
Total	99.52	98.18	100.26	100.11

2.4.2. Characterization of BSA-MWNT Suspensions

The sonication and centrifugation protocol developed in our previous works to prepare purified BSA-coated MWNT suspensions [50,51] was modified by using a ten-fold lower concentration of BSA (0.1 mg/mL) in the BSA working solution. Normally, this procedure results in a suspension containing 400–500 μg/mL of BSA-coated MWNTs, which was the case for each MWNT product except for the 2018-pMWNTs (Table 2.2). Zeta potential and DLS analyses were part of a quality control routine for the preparation of all MWNT suspensions, as previously described [50,51,54]. Table 2.2 shows that the zeta potentials for the BSA-cMWNTs in deionized water were slightly more negative than those for the BSA-pMWNTs, as expected; and, there were only minor differences in the particle size distributions of BSA-pMWNT and BSA-cMWNT

suspensions indicating that the suspended MWNTs possessed similar dimensions with no evidence of major agglomeration. One notable discrepancy, however, was the inability to suspend the 2018-pMWNTs in BSA above a concentration of 275 µg MWNTs/mL (corresponding to a maximum concentration of 136 µg MWNTs/mL when the BSA-MWNT suspension was diluted 1:1 with cell culture medium).

Table 2.2. Particle size and zeta potential analyses of purified BSA-MWNT suspensions.

BSA–MWNT Suspension [1]	Relative MWNT Concentration (µg/mL) [2]	Dynamic Light Scattering [3]		Zeta Potential (mV) [6]
		HDD (nm) [4]	PDI [5]	
2015-pMWNTs	417 ± 19	81.4 ± 5.4	0.21	-31.8 ± 1.9
2015-cMWNTs	496 ± 34	85.7 ± 6.8	0.20	-33.8 ± 1.6
2018-pMWNTs	275 ± 18	81.3 ± 2.1	0.20	-29.1 ± 1.8
2018-cMWNTs	456 ± 15	84.1 ± 1.6	0.21	-32.8 ± 1.5

[1] Purified BSA-MWNT suspensions were prepared by a sonication and centrifugation technique. [2] Relative MWNT concentrations were measured using the absorbance at 500 nm of each respective suspension; the values are presented as the mean $\pm$ the SD of $n \geq 3$ independent samples. [3] Aliquots of purified pMWNT or cMWNT suspensions were diluted 1:10 in 0.10 mg/mL BSA working solutions. [4] Hydrodynamic diameter (HDD); the values are presented as the mean $\pm$ the SD of $n \geq 3$ independent samples. [5] Polydispersity index (PDI). [6] Aliquots of purified pMWNT or cMWNT suspensions were diluted 1:10 in deionized water; the values are presented as the mean $\pm$ the SD of $n \geq 3$ independent samples. The relative MWNT concentrations, HDDs, and zeta potentials of the 2015 MWNTs were essentially identical over the course of ~1 year.

2.4.3. Macrophage Proliferation Assays

Mammalian macrophages were chosen for this work since they are a key intermediary in nanomaterial pathology and they specialize in phagocytosing foreign particles. The cell proliferation of murine RAW 264.7 macrophages incubated with BSA-MWNT suspensions prepared with each of the four MWNT products was measured after a 24-h exposure to different concentrations of MWNTs using a previously standardized crystal violet assay [55]. Figure 2.1 shows that there was not a significant decline in the 24-h cell proliferation for RAW 264.7 cells incubated with either the 2015-pMWNTs, the 2015-cMWNTs, or the 2018-cMWNTs at the highest concentration tested (200 μg MWNTs/mL). However, the 24-h proliferation of cells exposed to the 2018-pMWNTs began to decline at 100 μg/mL and the cell count was 78% relative to the control at the highest concentration tested (136 μg pMWNTs/mL). For comparison, the 24-h cell counts for cells incubated with 150 μg/mL BSA suspensions of 2015-pMWNTs, 2015-cMWNTs, and 2018-cMWNTs were 98%, 96%, and 92%, respectively, relative to the control. A direct comparison of the BSA-pMWNT responses at 100 μg/mL revealed that the 24-h proliferation of cells incubated with BSA-suspensions of 2018-pMWNTs was statistically different ($p = 0.01$) relative to BSA-suspensions of 2015-pMWNTs. Interestingly, there were no noticeable differences in the appearance or morphologies of macrophages incubated with BSA-MWNT suspensions prepared with the 2018-pMWNTs relative to the other three MWNT products.

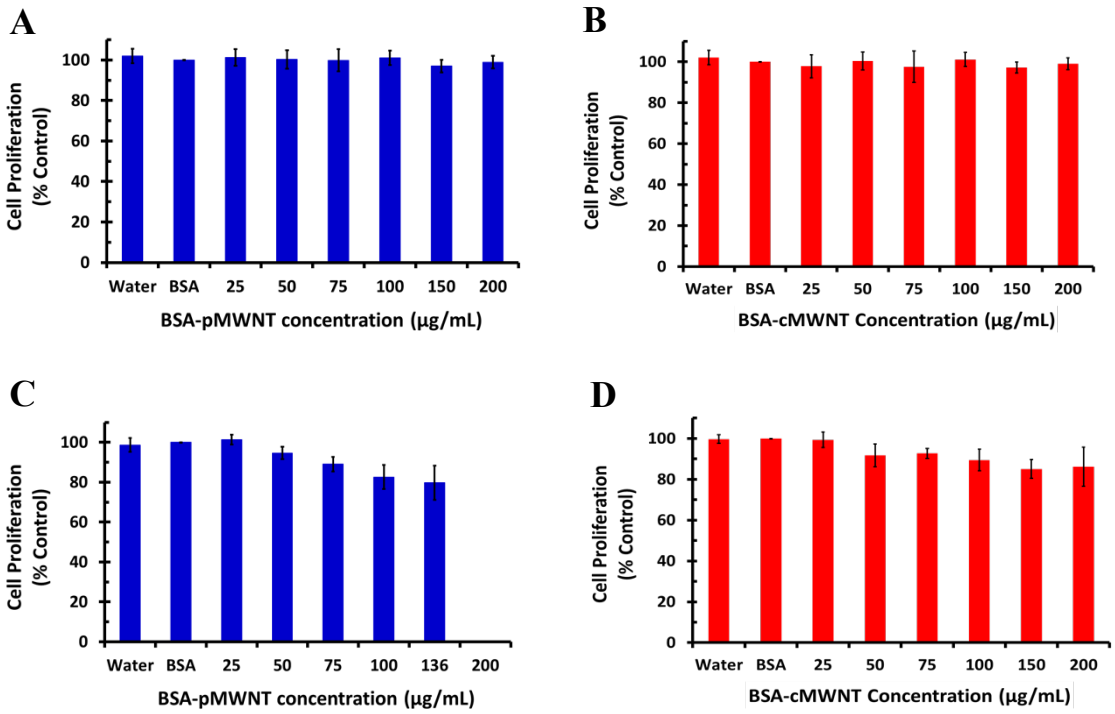

Figure 2.1. Cell proliferation of RAW 264.7 macrophages cultured with purified BSA-MWNT suspensions prepared with (**A**) 2015-pMWNTs, (**B**) 2015-cMWNTs, (**C**) 2018-pMWNTs, and (**D**) 2018-cMWNTs. MWNTs suspended in a 0.10 mg/mL BSA working solution were mixed with an equal volume of 2X-concentrated medium to produce MWNT concentrations of 0, 25, 50, 75, 100, 150, and 200 µg/mL, except for the 2018-pMWNTs where the highest MWNT concentration that could be made was 136 µg/mL. Exposure to deionized water or a BSA working solution (in the absence of MWNTs) were the controls. Equivalent number of cells were seeded in 48-well plates and incubated at 37 °C under standard cell culture conditions for 24 h prior to the experiment. Cell proliferation after incubation with control and test media for 24 h at 37 °C was determined by the crystal violet assay where the proliferation of control cells exposed to the BSA working solution in the absence of MWNTs was set to 100%. All data sets are the mean of quadruple samples in three independent experiments ± the SD. The 24-h proliferation of RAW 264.7 cells incubated with 2015 MWNTs were essentially identical over the course of ~8 months.

One hypothesis as to why BSA-coated MWNTs prepared with the 2018-pMWNT product decreased the proliferation of RAW 264.7 cells was the possibility that the 2018-pMWNTs adsorbed essential micro-nutrients, or protein growth factors, or both, provided by serum in the cell culture medium, thereby reducing cell proliferation by an indirect mechanism that did not

involve a physical nanotube–cell interaction [63,64]. To test this, RAW 264.7 cell proliferation assays were performed in medium containing twice the concentration of serum. For 125-µg/mL BSA-suspensions of 2015-pMWNTs, the 24-h proliferation of cells incubated in 20% FBS (96% relative to the control) was statistically similar to the proliferation of cells incubated in 10% FBS (95% relative to the control); and for 125-µg/mL BSA-suspensions of 2018-pMWNTs, the 24-h proliferation of cells incubated in 20% FBS (82% relative to the control) was also statistically similar to the proliferation of cells incubated in 10% FBS (80% relative to the control; data not shown). These data suggest that the potential depletion of essential serum nutrients from medium by 2018-pMWNTs was not sufficient to generate a false-positive toxicity assessment.

Since the statistical difference from the 24-h cell proliferation assays of the two BSA-pMWNT samples was slight, the response of RAW 264.7 cells as a function of the pMWNT dose was evaluated by extending the pMWNT exposure time to 72 h. While the 72-h proliferation of cells incubated with 125 µg/mL BSA suspensions of 2015-pMWNTs was reduced by ~33% relative to the control, the 72-h proliferation of cells exposed to 125 µg/mL BSA suspensions of 2018-pMWNTs was reduced by ~70% relative to the control, corresponding to an IC-50 of ~90 µg pMWNTs/mL for the 2018-pMWNT product (Figure 2.2). Moreover, while there were no noticeable differences in the appearance or morphologies of macrophages incubated for 72 h with BSA-MWNT suspensions of 2015-pMWNTs relative to controls, some RAW 264.7 cells exposed to BSA-MWNT suspensions of 2018-pMWNTs for 72 h began to round up in irregular-shapes (Figure A1), suggesting that their failure to proliferate was a result of a cytotoxic effect.

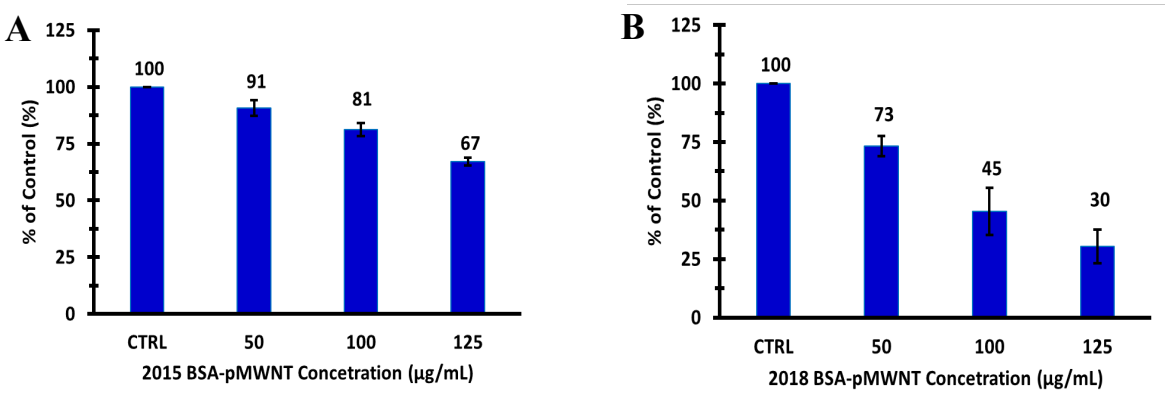

Figure 2.2. Cell proliferation of RAW 264.7 macrophages cultured with purified BSA-MWNT suspensions prepared with (**A**) 2015-pMWNTs and (**B**) 2018-pMWNTs. MWNTs suspended in a 0.10 mg/mL BSA working solution were mixed with an equal volume of 2X-concentrated medium to produce MWNT concentrations of 0, 50, 100, and 125 µg/mL. Exposure to a BSA working solution (in the absence of MWNTs) was the control. Equivalent number of cells were seeded in 48-well plates and incubated at 37 °C under standard cell culture conditions for 24 h prior to the experiment. Cell proliferation after incubation with control and test media for 72 h at 37 °C was determined by the crystal violet assay where the proliferation of control cells exposed to the BSA working solution in the absence of MWNTs was set to 100%. All data sets are the mean of quadruple samples in three independent experiments ± the SD.

2.4.4. Accumulation of pMWNTs by Macrophages

Another hypothesis as to why BSA-coated MWNTs prepared with the 2018-pMWNT product decreased the proliferation of RAW 264.7 cells was the possibility that the cells phagocytosed more 2018-pMWNTs than 2015-pMWNTs. To investigate this, RAW 264.7 cells were incubated for 24 h in media containing BSA-coated pMWNTs at 100 µg/mL prepared with 2015-pMWNTs or 2018-pMWNTs. After the incubation, the SDS-PAGE method was used to quantify cell-associated MWNTs from cell extracts as previously described [56]. The average amount of 2015-pMWNTs accumulated by cells was 9386 ± 999 fg pMWNTs/cell and that for the 2018-pMWNTs was 7856 ± 350 fg pMWNTs/cell. This data indicates that the difference in the cell proliferation between the two pMWNT products cannot be attributed to a greater amount of

2018-pMWNTs taken-up by RAW 264.7 cells. In summary, the cell accumulation and cell proliferation results were somewhat surprising since the same MWNT products were purchased from the same manufacturer, albeit three years apart; and, because there were no major differences in the carbon purities of the 2018-pMWNT and 2015-pMWNT powders, no major differences were observed in the DLS-determined particle size distributions of BSA-suspensions of 2018-pMWNTs and 2015-pMWNTs. This prompted a more comprehensive physicochemical characterization of all four MWNT products, as described next.

2.4.5. ICP-MS of MWNTs

Since the four MWNT products were synthesized by a Fe/Ni/Co-catalyzed CVD process, ICP-MS analyses were performed to assay for unusually high levels of these metals in the 2018-pMWNT powder whose presence might have affected the proliferation of RAW 264.7 cells. As shown in Table 2.3, the key findings with the 2015-pMWNT product, which did not alter the 24-h proliferation of the macrophages, were high levels of Ni (~5592 ppm) and Fe (~1690 ppm). In contrast, the unique aspect of the 2018-pMWNT product was a high level of Co (~1242 ppm) relative to the levels found in the 2015-pMWNTs. Thirty-three other metals were also assayed using ICP-MS, and Co was the only element present in the 2018-pMWNT powder at levels that were significantly higher than what was observed in any of the other three MWNT powders (Table A1). However, in this work, it is important to note that MWNT powders were not directly applied to cells, rather BSA-MWNT suspensions were applied and they were purified during preparation by a centrifugation step to remove heavier metal-containing MWNTs and bundles. Therefore, additional ICP-MS analyses of a BSA-pMWNT suspension prepared with the 2018-pMWNT powder were performed. These data revealed ~4 ppm Co, corresponding to a dramatic reduction

(>99%) in the Co level relative to the level observed in the MWNT powder, akin to our previous ICP-MS analyses of metals detected in centrifuged carbon nanotube suspensions relative to carbon nanotube powders [53,54]. The literature on the biological effects of Co cations and nanoparticles on mammalian cells was therefore examined. The most relevant finding was reported by Huk and co-workers who studied the effects of 2–10 ppm Co^{2+} ions on J774 mouse macrophages, and who observed significant mortality after a 24-h incubation with 10 ppm Co^{2+} [65]. A dose-response cell proliferation assay with Co^{2+} and RAW 264.7 macrophages was performed next, and a 24-h IC-50 of ~55 ppm Co^{2+} was determined. This result suggests that the 4 ppm Co^{2+} observed in the BSA-pMWNT suspension prepared with the 2018-pMWNT powder did not have a significant acute effect on the proliferation of RAW 264.7 cells.

Table 2.3. ICP-MS analyses of pMWNT powders.

Element	2015-pMWNTs	2018-pMWNTs
Fe (ppm)	1689.8	475.4
Ni (ppm)	5591.6	8.8
Co (ppm)	24.6	1241.8

2.4.6. TEM and HR-TEM Imaging of MWNTs

The inside and outer diameters of MWNTs were estimated from TEM and HR-TEM images. All four MWNT powders were reported by the manufacturer to contain MWNTs with outer diameters of 10–20 nm and inside diameters of 5–10 nm. As shown in Table 2.4, the observed values closely matched the reported values, and there were no significant differences for the inside and outer diameters among the four MWNT products. Somewhat surprisingly,

significant differences between the four MWNT products were not observed via HR-TEM imaging (Figures A2–A10). The majority of MWNTs displayed asymmetric, partially collapsed, open-ends (Figure A2), a small number of MWNTs displayed a relatively symmetric, open-ended nanotube architecture (Figure A6), and very few MWNTs displayed a closed-end nanotube architecture (Figure A4). This is most likely because as-synthesized pMWNTs, and, as-synthesized and oxidized cMWNTs, were reported by the manufacturer to have been shortened by milling to generate the exact lots of pMWNTs and cMWNTs used in this work. HR-TEM images of both pMWNTs and cMWNTs also revealed evidence of hollow tubular cavities (Figures A4 and A10), as well as, asymmetric (bent) sidewalls and symmetric sidewall damage (Figures A2, A3, A5, A7, and A10) as defined by Kónya and co-workers [66]. However, extreme sidewall damage, akin to that observed by Shaffer and co-workers for acid-treated CVD-synthesized MWNTs, was not observed with the two cMWNT products [67]. Additionally, fishbone-type structures (Figure A8), as defined by Su and co-workers [42], and cup-stacked architectures (Figure A9), as defined by Lehman and co-workers [68], were observed frequently for all four MWNT products. Debris-free regions and regions displaying debris of various shapes and sizes, most likely disordered or amorphous carbons akin to that observed by Shaffer and co-workers for both pristine and acid-treated CVD-synthesized MWNTs [67], were observed inside the central cavities and along the sidewalls of all four MWNT products (Figures A5 and A10). However, the extensive degree of sidewall oxidative debris observed by Fairbrother and co-workers for acid-treated MWNTs was not observed with the 2015-cMWNTs and 2018-cMWNTs [69]. Additionally, oxidative debris, defined as carboxylated carbon fragments and polycyclic aromatic hydrocarbons that can be removed by dilute base washings [70], was miniscule for both cMWNT

products, as determined by Raman and UV-Vis spectroscopic analyses (data not shown). Finally, metal inclusions, as defined by Andrews and co-workers [71] and Pourchez and co-workers [72], were rarely observed in any of the four MWNT products. Ultimately, the structural morphologies observed for all four MWNT products most closely resembled those presented by Kónya and co-workers who used HR-TEM to study the effects of shortening MWNTs by a ball milling process [66]. It is therefore hypothesized that the similarities observed in the HR-TEM images of the pMWNTs and cMWNTs stemmed primarily from the manufacturer's milling process, and that the oxidative treatment applied to the cMWNTs did not impart additional structural changes of a significant nature.

Table 2.4. TEM analyses of pMWNT and cMWNT powders.

MWNT Product	Outer Diameter (nm)	Inner Diameter (nm)
2015-pMWNTs	18 ± 3	5.6 ± 1.3
2015-cMWNTs	19 ± 5	5.7 ± 1.7
2018-pMWNTs	21 ± 4	5.3 ± 0.6
2018-cMWNTs	21 ± 4	5.6 ± 2.1

2.4.7. TGA of MWNTs

The TGA weight-percentage and derivative curves of the four MWNT powders are shown in Figure 2.3. Three of the derivative curves (i.e., the 2015-pMWNTs, the 2015-cMWNTs, and the 2018-cMWNTs) very closely match the profile of the pMWNT derivative curve provided by the manufacturer; specifically, an upward sloping, sharp first peak near 600 °C followed by a

closely adjoined, rapidly decaying second peak. The similarities of the main oxidation temperature peaks for these MWNT powders (ranging from 602 °C for the 2015-pMWNTs to 630 °C and 601 °C for the 2015-cMWNTs and 2018-cMWNTs, respectively) is akin to the slight oxidation temperature differences observed by Yim and co-workers for pristine vs. acid-oxidized MWNTs [73]. Oxidation temperatures observed at ~600 °C have also been associated with well-graphitized MWNT structures, which have been reported by Galiotis and co-workers to oxidize between 600 and 700 °C depending on the exact type of MWNT analyzed [74]. In contrast, the derivative curve of the 2018-pMWNTs not only displayed a broader and more Gaussian-like peak profile, the oxidation temperature of this peak occurred ~80 °C earlier than that observed for the 2015-pMWNTs. Defects in carbon nanotube walls are well-known to increase local reactivity, leading to lower oxidation temperatures as observed in TGA mass-loss profiles [75,76]. The main oxidation peak for the 2018-pMWNTs at 518 °C is akin to the oxidation of amorphous or disordered carbons, which typically oxidize at ~500 °C owing to their lower activation energies for oxidation and/or to the presence of reactive defect sites [74,76]. Note, while caution should be exercised in comparing the oxidation temperatures of different MWNTs since these temperatures will vary based on nanotube diameters and ring strain, the similarities in the inside and outer diameters observed via HR-TEM (Table 2.4) supports an interpretation that the 2018-pMWNTs display less oxidative stability than the 2015-pMWNTs. Moreover, the main oxidation peak for the 2018-pMWNTs at 518 °C very closely matches the Gaussian-like peak profile at ~490 °C observed for 19-nm diameter MWNTs synthesized by a Co-catalyzed CVD process [76], which

correlates with the high amount of Co found in the 2018-pMWNT powder by ICP-MS relative to that observed in the 2015-pMWNT powder (Table 2.3).

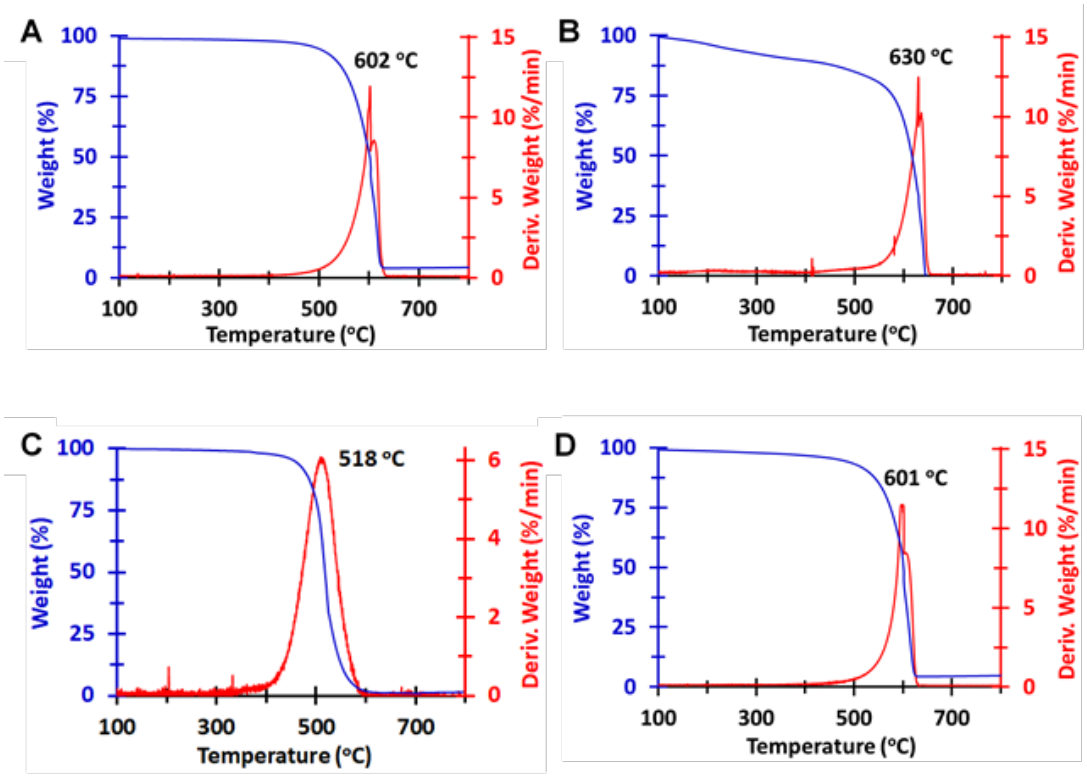

Figure 2.3. Representative thermograms (in air) showing the weight percent (blue) and derivative of weight percent (red) of the (**A**) 2015-pMWNT, (**B**) 2015-cMWNT, (**C**) 2018-pMWNT, and (**D**) 2018-cMWNT powders.

In addition to displaying a slight (≤3%) loss of mass at temperatures below 180 °C, corresponding to the release of chemically or physically absorbed gases and moisture [62,74], the next key region of interest in the weight-percentage plots of the four MWNT powders was that between 180 and 450 °C (Figure 2.3). Weight losses in this region have been attributed to the decomposition of MWNT functional groups, such as surface oxides that evolve CO_2 and CO gases [62,74,77,78]. As shown in Figures 2.3 A,B for the 2015-MWNT products, weight losses of 1.7% and 9.3% were observed between 180 and 450 °C for the pMWNT and cMWNT powders,

respectively, suggesting that the cMWNTs possess more surface oxides than the pMWNTs, as would be expected. As shown in Figures 2.3 C,D for the 2018-MWNT products, a weight loss of 1.9% was observed between 180 and 350 °C for the pMWNT powder and a weight loss of 3.0% was observed between 180 and 450 °C for the cMWNT powder. In summary, it is noteworthy that both pMWNT products displayed only a small amount of surface oxides, which supports the observation that they could not be stably suspended in water following 1 h of sonication. Additionally, it is interesting to note that the 2018-cMWNTs did not qualitatively display as much surface oxides as the 2015-cMWNTs. Finally, while it could be surmised that the 2015-pMWNTs might have been used to generate 2015-cMWNTs, it is safe to conclude that the manufacturer did not use the 2018-pMWNTs to generate 2018-cMWNTs.

2.4.8. Raman Spectroscopy of MWNTs

The Raman spectra of the four MWNT powders are shown in Figure 2.4. Each displayed characteristic carbon nanomaterial Raman bands such as the disorder-induced D-band at ~1328 cm^{-1}, the tangential graphitic G-band at ~1577 cm^{-1}, the disorder-induced G2- or D′-band at ~1604 cm^{-1}, and the second-order 2D- or G′-band at ~2652 cm^{-1} [79,80]. The D- and D′-bands are attributed to lattice defects, finite graphene sheets inside carbon nanotube walls, and amorphous or disordered carbons, the G-band is representative of ideal sp^2-bonded carbon structures, and the G′-band infers long range order in carbon-based structures [42,45]. The mean intensity ratio of the D- and G-bands (I_D/I_G) of the four MWNT powders is shown in the Figure 2.4 inset. This intensity ratio has long been used as a qualitative metric of purity and quality for CVD-synthesized MWNTs of similar diameters with a decrease in the ratio being an indicator of less defect sites (i.e., higher crystallinity) and less amorphous carbon in the sample [69,81]. The I_D/I_G ratio of the

2015-pMWNTs and 2015-cMWNTs (1.57 and 1.78, respectively) follows the expected trend for MWNTs following an oxidative treatment. Specifically, Cui and co-workers and Gogotsi and co-workers both reported I_D/I_G-ratio increases of similar magnitudes for CVD-synthesized MWNTs following acid oxidization [82,83]. However, while the 1.78-I_D/I_G ratio of the 2018-cMWNTs was identical to that observed for the 2015-cMWNTs, the 1.87-I_D/I_G ratio for the 2018-pMWNTs was the highest of the four MWNT products. This suggests an increase in defect density and a lower degree of crystallinity of graphitic structures for the 2018-pMWNTs, which is consistent with the lower oxidative stability observed in its TGA profile relative to the three other MWNT products (Figure 2.3).

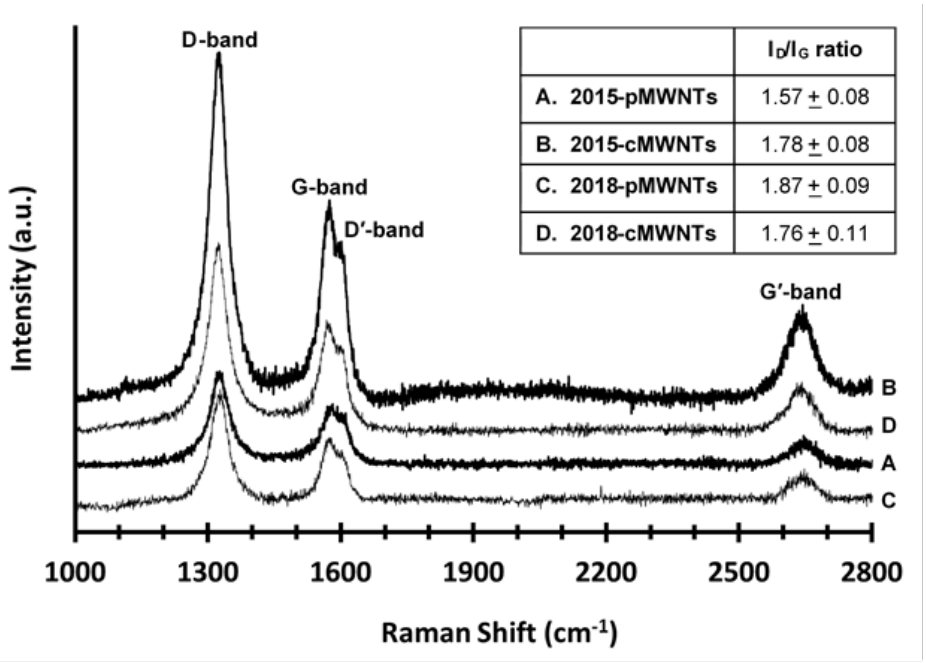

Figure 2.4. Representative baseline-corrected Raman spectra (632.8-nm laser excitation) of the (**A**) 2015-pMWNT, (**B**) 2015-cMWNT, (**C**) 2018-pMWNT, and (**D**) 2018-cMWNT powders showing characteristic carbon nanomaterial Raman bands (e.g., D-bands at ~1328 cm^{-1}, G-bands at ~1577 cm^{-1}, D′-bands at ~1604 cm^{-1}, and G′-bands at ~2652 cm^{-1}). The spectra were offset for clarity. **Inset:** Mean I_D/I_G ratios $\pm$ SDs of $n \geq 7$ analyzed regions for each powder.

2.4.9. XRD Analyses of MWNTs

XRD was performed to analyze the crystallinity of the four MWNT powders. As shown in Figure A11, the main features in the powder X-ray diffraction patterns were peaks located near the (002), (100), and (004) reflections of graphite. Specifically, the intense diffraction peaks at 2θ ≈ 26° can be attributed to the (002) reflection of graphite, the asymmetric diffraction peaks at 2θ ≈ 43° can be assigned to the (100) reflection of graphite, and the high-order diffraction peaks at 2θ ≈ 53° can be assigned to the (004) reflection of graphite that are typically observed with MWNTs [62,71]. For the 2015 products, the (002) reflections for the pMWNTs and cMWNTs were observed at 2θ = 25.98° and 26.02°, respectively, while the (002) reflections for the 2018-pMWNTs and 2018-cMWNTs were observed at 2θ = 25.86° and 25.92°, respectively. In both cases, the (002) reflections for the cMWNTs were shifted by 0.04–0.06°, which was similar to the 2θ-shift of 0.05° observed by Mohanapriya et al. for the (002) reflection of pMWNTs following an oxidative treatment with nitric acid [84]. The (002) reflections were also used to determine the average coherence length (L_C), the mean crystalline size along the c-axis perpendicular to the long MWNT axis, through the use of the Scherrer equation. The calculated L_C values for the two pMWNTs were 9.7 nm and those for the two cMWNTs were 8.8 nm, similar to the 1-nm decrease in L_C values observed by Malikov et al. for pMWNTs following an oxidative treatment with nitric acid [85]. Since these values represent an average stacking height of graphitic planes in MWNT walls, a decrease in the L_C value for pMWNTs following an oxidative treatment can be attributed to the partial loss of the outermost graphitic layers and the introduction of defects, which reduces the symmetry of the plane [28]. Finally, for all four MWNT powders, there is also a weak reflection observed at 2θ ≈ 44.7° (denoted by the asterisk in Figure A11), which is slightly more

pronounced in the XRD pattern of the 2018-pMWNTs. This broad feature could be an amalgamation of the (101) reflection of graphite ($2\theta \approx 44.4°$), the (111) reflection of Co F$m\overline{3}m$ ($2\theta \approx 44.6°$), and/or a reflection from other metal-based structures [86,87].

2.4.10. BET Surface Area Measurements of MWNTs

A number of physicochemical characteristics of MWNTs are known to influence BET-determined specific surface areas (SSAs); for example, the number of nanotube walls, nanotube diameters, nanotube bundling, the fraction of open nanotubes, surface functionalization with hydroxyl and carboxyl groups, and types and amounts of metal and amorphous carbon impurities [26,42]. Consequently, there are numerous forewarnings with respect to the use of the BET SSA method with carbon nanotubes because reported SSAs of similar materials frequently differ, and measured SSAs are not always congruent with product specifications [26,68]. Nonetheless, increases in BET-SSAs for acid-oxidized CVD-synthesized MWNTs relative to their pristine counterparts are the norm regardless of the exact oxidant(s) and oxidation reaction conditions employed. This is because oxidative treatments are known to create cavities by opening nanotube ends and by damaging/distorting MWNT sidewalls in the process of removing metal catalysts and amorphous carbon impurities, resulting in an increase in the measured BET-SSA [26,62,70,82]. Additionally, oxidative treatments have been shown to increase BET-SSAs through the generation of functional groups that de-bundle MWNTs by disrupting π–π interactions between pristine nanotube surfaces [26]. Herein, the BET-determined SSAs of the 2015-pMWNT and 2015-cMWNT powders were 91 and 145 m^2/g, respectively, corresponding to a SSA-increase of ~60%; and, the BET-determined SSAs of the 2018-pMWNT and 2018-cMWNT powders were 191 and 286 m^2/g, respectively, corresponding to a SSA-increase of ~50%. While the exact reaction

conditions of the oxidative treatment performed by the manufacturer are not known, the increases in SSAs measured by the BET measurement for the 2015- and 2018-MWNT product pairs are consistent with the 11–62% increases in BET-SSAs measured by others who evaluated CVD-synthesized pMWNTs and cMWNTs [26,42,70,82,88]. However, it is noteworthy that both of the 2018 products had significantly higher BET-SSAs than the 2015 products.

2.4.11. XPS Analyses of MWNTs

XPS is a method that can be used to determine the elemental composition of a MWNT surface by measuring the binding energy of photoelectrons ejected when the MWNTs are irradiated with X-rays; it is a surface sensitive technique because the escape depth of the photoelectrons amounts to only a few atomic layers [69,89]. Table 2.5 shows the XPS elemental analyses of the pMWNT and cMWNT powders determined from the C1s and O1s spectra shown in Figures A12 and A13, respectively. The percentages of carbon and oxygen determined by the high-spatial resolution XPS method were consistent with the elemental analysis results shown in Table 2.1 that were obtained using a bulk method of analysis, except for the lower amount of surface oxygen detected by XPS for the 2018-pMWNTs. As expected, the XPS-determined oxygen-to-carbon ratios of both cMWNT products were greater than their corresponding pMWNT products (Table 2.5), akin to the increases in XPS-determined oxygen-to-carbon ratios reported by a number of groups who studied the effects of various oxidation reactions on pMWNTs [73,82,90,91].

Table 2.5. XPS elemental analyses of pMWNT and cMWNT powders.

MWNT Powder	% Carbon [1]	% Oxygen [2]	Subtotal [3]	O/C [4]
2015-pMWNTs	96.4	3.6	100.0	0.04
2015-cMWNTs	94.4	5.6	100.0	0.06
2018-pMWNTs	99.1	0.9	100.0	0.01
2018-cMWNTs	95.6	4.4	100.0	0.05

[1] Percentage of atomic carbon determined from the area of the respective C1s peak at ~284 eV, normalized to 100% of the elements detected. [2] Percentage of atomic oxygen determined from the respective area of the O1s peak at ~532 eV normalized to 100% of the elements detected. [3] All four samples were composed of carbon and oxygen; no other elements were observed in the respective survey scans noting however that XPS cannot detect H or He. [4] Ratio of the atomic percentages of oxygen to carbon.

XPS can be further applied to determine the chemical or electronic state of elements. For example, analysis of the C1s spectra of the four MWNTs shown in Figure A12 indicates that the predominant features at ~284.2 eV correspond to carbons in the sp^2 hybridization state [73,92]. These peaks resemble the C1s peak of graphite that is typically observed at 284.6 eV, further noting that it is common to see a negative shift of 0.3 eV in the binding energy of MWNTs owing to weaker C–C bonding due to the curvature of graphene sheets and larger interlayer spacings [93]. The presence of functional groups and other defects of MWNTs will influence the full width at half maximum (FWHM) of the sp^2-hybridized carbon C1s peak [92]. The FWHM values of the graphitic C1s peaks at ~284.2 eV observed for the four MWNTs were all relatively narrow, ranging from 0.9–1.1 eV (Figure A12), and were comparable to 1.2 eV-FWHM values reported for graphite and hydrogen-terminated graphene [92].

Further analysis of the C1s spectra shown in Figure A12 indicates the presence of defects in graphitic structures between 285.1 and 285.7 eV, as well as, satellite peaks between 290.8 and 294.0 eV stemming from π–π* electronic transitions that are representative of disordered sp^2 carbons [73,91,94]. In addition, there are possibly phenolic, alcohol, and/or ether groups at ~286.5 eV; carbonyl, quinone, carboxyl, and/or lactone groups at ~287.8 eV; and atmospheric contaminants such as O_2 and carbonates associated with adsorbed CO_2 between 289–291 eV [91,94]. Unfortunately, the differences in binding energies for these various functional groups are quite small, which is typical for electronegative elements such as oxygen; additionally, discrepancies in the literature regarding the positions of these peaks further contributes to the complexity of the spectral analyses. For example, reported XPS C1s assignments for phenolic and/or alcohol groups on MWNTs span across the range of 285.2–286.8 eV; assignments for ether functional groups on MWNTs span across the range of 286.1–288.0 eV; assignments for carbonyl and/or quinone functional groups on MWNTs span across the range of 286.4–288.1 eV; and assignments for carboxyl and/or lactone functional groups on MWNTs span across the range of 288.0–289.8 eV [69,73,90,91]. While deconvolution of the overlapping peaks is possible, the results of the curve fitting can be ambiguous and will be influenced to some extent by the somewhat arbitrary inputs for the number, shape, and width of the peaks [69,89]. Therefore, the only firm conclusions drawn from these data were that there were no major differences in the C1s spectral profiles of the four MWNTs, except for the slight distinctions with the 2018-pMWNTs in the sp^3-carbon region and the π–π* region (as denoted by the symbols in Figure A12).

Analysis of the O1s XPS peaks of the four MWNT products revealed notable differences in the spectral profiles. As shown in Figure A13, the O1s peak of the 2015-pMWNTs could be fit

well with a single Gaussian peak centered at ~532 eV, while the other MWNTs could not. Instead, the other three MWNT products were best fit with two Gaussian peaks centered at ~531 eV and ~533 eV. Table A2 shows the exact peak positions and the areas under each curve. The O1s spectral profile of the 2015-cMWNTs was broader than that of the 2015-pMWNTs, as expected, and the spectral profile of the 2015-cMWNTs was quite similar to the profile of the 2018-cMWNTs. However, the broader O1s profile of the 2018-pMWNTs did not match that of the 2015-pMWNTs. These data suggest that a variety of surface oxygen functionalities are likely present on the four MWNT products, including but not limited to: (i) physically adsorbed oxygen and/or water, (ii) isolated hydroxyl groups, (iii) carbonyl oxygen atoms in carbonyl, quinone, carboxyl, anhydride, and/or lactone groups, (iv) oxygen atoms from hydroxyl, phenolic, and/or ether groups, and (v) oxygen atoms from carboxylic acids, all of which roughly span the O1s spectral range of 530–535 eV [82,90,91]. Again, it was therefore difficult to distinguish the specific oxygen-containing groups from the O1s spectra with high confidence because unambiguous deconvolution was complicated by the presence of different species with similar and over-lapping binding energies, because of the low amount of oxygen atoms present, and because of discrepancies in the literature regarding the assignments of peak positions [69,95]. Therefore, the only conclusions drawn from these data were that the 2015-cMWNTs, 2018-pMWNTs, and 2018-cMWNTs had slightly different populations of graphitic C–O and C=O species relative to the 2015-pMWNTs (Figure A13 and Table A2).

2.4.12. FTIR Spectroscopy of MWNTs

FTIR spectroscopy was employed to gain more specific insight into the surface oxygen species present on the four MWNT products. The FTIR spectra shown in Figure 2.5 display two

intense bands for all four MWNTs. The first is the broad band at ~3330 cm^{-1} that is attributed to hydroxyl vibrational stretching modes [υ(O–H)] of surface -O–H groups, -O–H moieties in carboxylic acid groups, water chemisorbed to MWNTs, and/or residual moisture in the KBr pellet [91,96,97]. The second is the band at ~1576 cm^{-1}, associated with the carbon skeleton of MWNTs, which is assigned to aromatic carbon–carbon vibrational stretching modes [υ(C=C)] that are polarized by adjacent oxygenated groups [89,91,96–98]. It was therefore interesting to note that both of these bands were more intense for the cMWNT products relative to the pMWNTs, as would be expected since it is well-known that treating pMWNTs with oxidizing agents such as the sulfuric acid/permanganate mixture reported by the manufacturer will generate a variety of surface oxygen species, most notably, carboxylic acid and hydroxyl groups. Accordingly, a third band at ~1724 cm^{-1} was also observed only in the spectra of the two cMWNT products, which has been attributed, in general, to the carbonyl vibrational stretching mode [υ(C=O)] of carbonyls and carboxyl groups [91,97], as well as, specifically, to non-conjugated carboxyl carbonyl groups [96,98]. Regardless of this nuance, the overall findings from the FTIR data support the manufacturer's claim that the cMWNTs were carboxylated. Finally, since milling MWNTs in air can generate surface oxygen functionalities [99], the FTIR data also lend credence to the idea that pMWNTs possess surface hydroxyl groups (likely at defect sites), in part due to the manufacturer's milling process, and that the milled cMWNTs additionally contain carbonyl groups because only they were treated with oxidizing agents.

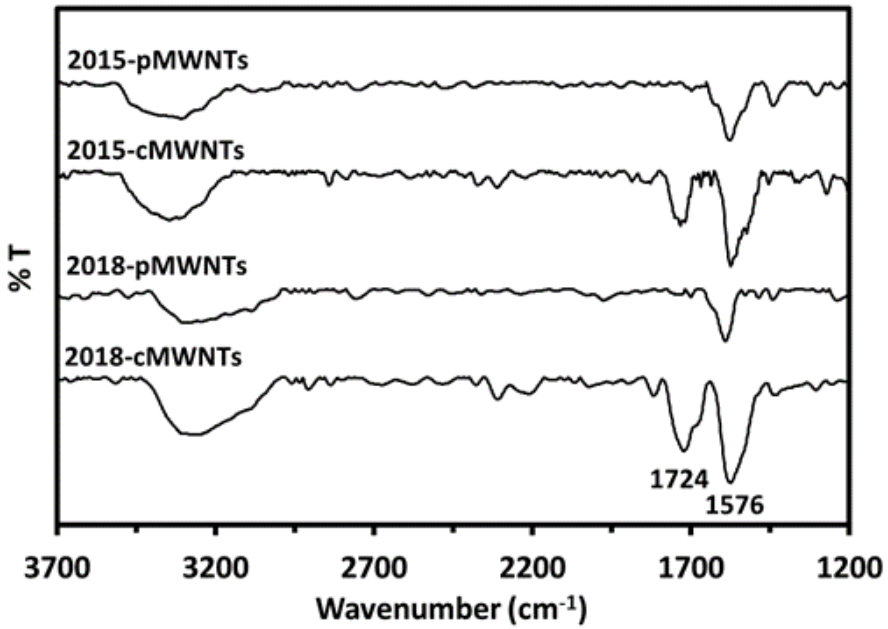

Figure 2.5. Normalized FTIR spectra of the four MWNT powders; from top to bottom: 2015-pMWNTs, 2015-cMWNTs, 2018-pMWNTs, and 2018-cMWNTs.

2.5. DISCUSSION

2.5.1. Physicochemical Properties of 2018-pMWNTs that Correlate with Reduced Cell Proliferation

A set of pMWNTs and cMWNTs with similar dimensions and purities was purchased in 2015 for evaluating the response of functionalized MWNTs to mammalian macrophages. Lot-acceptance testing was performed using a combustion analysis technique to evaluate the carbon purity of the pMWNTs and cMWNTs. As shown in Table 2.1, the carbon purity of the 2015 lots of pMWNTs and cMWNTs closely matched the 95% specifications of the manufacturer. Next, purified BSA-coated suspensions of pMWNTs and cMWNTs were prepared for proliferation assays with RAW 264.7 macrophages. As shown in Figures 2.1A,B, there was not a significant decline in the 24-h proliferation of RAW 264.7 cells with either sample up to the highest

concentration tested (200 μg MWNTs/mL). In 2018, as supplies of the 2015 MWNT powders began to run low, a new set of the exact same pMWNT and cMWNT products was purchased. Lot-acceptance testing was performed and both of these 2018 materials closely matched the 95% carbon purity levels stated by the manufacturer (Table 2.1). Next, purified BSA-suspensions of pMWNTs and cMWNTs were prepared for proliferation assays with RAW 264.7 cells. As shown in Figures 2.1 C,D, while there was not a significant decline in the 24-h proliferation of RAW 264.7 cells with the 2018-cMWNTs up to the highest concentration tested (200 μg MWNTs/mL), the proliferation of RAW 264.7 macrophages decreased to 78% of the control when incubated with 136 μg/mL of the 2018-pMWNTs, the highest concentration of BSA-suspended MWNTs that could be prepared in cell culture medium using the 2018-pMWNT powder. It should also be noted that when freshly prepared samples of 2015 BSA-MWNTs were tested ~8 months apart, the 24-h proliferation of RAW 264.7 cells incubated with 2015 MWNTs were essentially identical, indicating that potential aging of the 2015 MWNT powders was not a source of variability (*vide infra*). Moreover, as shown in Figure 2.2, a 72-h IC-50 of ~90 μg pMWNTs/mL was determined for BSA-suspensions of 2018-pMWNTs and some RAW 264.7 cells exposed to BSA-MWNT suspensions prepared with the 2018-pMWNTs were rounded after 72 h (Figure A1), consistent with their failure to proliferate being a result of a cytotoxic effect.

Suspensions of all four BSA-coated MWNTs were characterized before the cell proliferation assays were performed, and as shown in Table 2.2, the DLS-determined dimensions of particles were quite similar, indicating that discrepancies in the agglomeration of MWNTs was not the cause of the biological response observed with the 2018-pMWNTs. It should also be noted that when freshly prepared samples of 2015 BSA-MWNTs were tested ~1 year apart, the relative

MWNT concentrations, HDDs, and zeta potential values were essentially identical, indicating that potential aging of the 2015 MWNT powders was not a source of variability (*vide infra*). Additionally, TEM and HR-TEM imaging did not reveal any significant differences in the inside and outside diameters of the four MWNTs (Table 2.4), and HR-TEM imaging did not reveal any major morphological differences among the four MWNTs (Figures A2–A10). Furthermore, the amounts of 2015-pMWNTs and 2018-pMWNTs taken up by RAW 264.7 cells did not correlate with the 24-h cell proliferation results; in other words, the reduced cell proliferation observed with the 2018-pMWNTs was not because the cells accumulated more 2018-pMWNTs than 2015-pMWNTs. In fact, the accumulated amount of BSA-pMWNTs prepared with the 2018 product was ~16% less than the accumulated amount of BSA-pMWNTs prepared with the 2015 product.

ICP-MS analyses revealed ~50× more Co in the 2018-pMWNT powder relative to the Co levels found in the 2015-pMWNTs (Table 2.3), and ~4 ppm Co was observed in BSA-pMWNT suspensions prepared with the 2018-pMWNT powder. A dose-response cell proliferation assay with Co^{2+} and RAW 264.7 macrophages yielded a 24-h IC-50 of ~55 ppm Co^{2+}, indicating that exposure to 4 ppm Co^{2+} should not have a significant acute effect on the proliferation of RAW 264.7 cells. While Liu and co-workers observed that Co nanoparticles had a more significant effect on RAW 264.7 cells than Co^{2+} ions [100], Co was not observed in the XPS survey scans of any MWNT powder and HR-TEM imaging rarely revealed metal inclusions in any MWNT sample. Therefore, the presence of Co was ruled out as the causation of the reduced proliferation of RAW 264.7 cells incubated with BSA-suspension of 2018-pMWNTs.

A perfect crystalline carbon nanotube comprises only hexagonal rings of sp^2-hybridized carbons. However, synthesized MWNTs are far from perfect and various amounts and types of

defects are generated during MWNT growth and subsequent post-synthetic treatments [30,99]. Defective MWNT structures have been classified into four main groups: topological differences in shape due to ring sizes other than hexagons, sp^3-hybridized carbon atoms, incomplete bonding defects (e.g., vacancies and dislocations), and doping with elements other than carbon [101]. Both the TGA (Figure 2.3) and Raman analyses (Figure 2.4) indicated an increased density of defect sites with the 2018-pMWNTs relative to the 2015-pMWNTs; specifically, the 2018-pMWNTs displayed lower oxidative stability and a higher I_D/I_G ratio.

The percentages of carbon and oxygen determined by XPS were consistent with the elemental analysis results obtained using a combustion analysis technique, except for the lower amount of surface oxygen detected by XPS for the 2018-pMWNTs (Tables 2.1 and 2.5). Analysis of the C1s spectral profiles of the four MWNTs revealed no major differences except for the slight distinctions for the 2018-pMWNTs in the sp^3-carbon region and the π–π^* region (Figure A12), whereas analysis of the O1s spectral profiles revealed that the 2015-cMWNTs, 2018-pMWNTs, and 2018-cMWNTs had slightly different populations of graphitic C–O and C=O species relative to the 2015-pMWNTs (Figure A13 and Table A2). FTIR spectroscopy, however, provided more specific functional group information, namely, that both cMWNT products were indeed functionalized with carbonyl groups whereas the pMWNTs were not (Figure 2.5). XPS and FTIR spectroscopic analyses were also used to assess whether atmospheric aging had any effect on the physicochemical properties of the 2015 MWNTs. For example, Liu et al. simulated atmospheric aging by studying the oxidation (by O_3 or $OH\cdot$) of single-walled carbon nanotubes, and observed increases in surface carboxylic acids or esters (i.e., an enhancement of the O/C ratio), but they did not observe any changes in toxicity with human A549 adenocarcinoma-derived alveolar epithelial

cells and THP-1 leukemia-derived peripheral blood monocytes [102]. Herein, all MWNTs were stored in the dark to avoid UV-catalyzed reactions, and increases in the O/C ratios as a function of time were not observed, most notably, with the older 2015 MWNTs. In fact, it was the newer 2018 pMWNTs that possessed the lowest O/C ratio (Table 2.5), and, as shown by the FTIR spectra in Figure 2.5, there was no evidence of carboxylic acids in either of the pMWNT materials.

Determining the fundamental origin(s) of a cytotoxic response to a MWNT sample is a complex endeavor because many MWNT physicochemical determinants are interrelated and it is difficult to systematically decouple them [30]; for example, milling MWNTs to modulate defect densities will also shorten MWNTs [99]. MWNT defects are a physicochemical property that have been proposed to affect the toxicity of mammalian cells [72,103–107]. Unfortunately, many toxicity reports focusing on defects were not limited to this single physicochemical parameter, rather, studies involved MWNTs with structural defects additionally had differences in other determinants such as lengths, BET-SSAs, and/or surface functionalization. One compelling in vivo study was reported by Lison and co-workers who progressively and selectively modified MWNTs by grinding and heating pMWNTs to introduce and modify structural defects [108]. Their results with Wistar rats indicated that the presence of MWNT structural defects mediated pulmonary toxicity, and they postulated that the toxic potential of MWNTs could be partially abolished by the elimination of surface defects. While additional well-designed studies to predict toxic responses based on individual physicochemical properties are warranted, the premise that structural defects are a key determinant of toxicity might help to explain the reduced proliferation of RAW 264.7 cells incubated with the 2018-pMWNTs that possessed more defects relative to the 2015-pMWNTs.

A more established tenet is that structural defects, surface chemistry, surface curvature, and the surface area of a MWNT are decisive factors involved in the dynamic formation of a protein corona [62,109]. In the present case, the protein corona is first given a coating of BSA that adsorbs onto MWNTs in the process of preparing BSA-MWNT suspensions, followed by an additional layer of macromolecules, primarily proteins that coat BSA-MWNTs (and compete with BSA for MWNT surface sites) once BSA-MWNTs are mixed with cell culture medium that contains serum. Thus, a protein corona, whose formation is governed in part by MWNT surface properties, can partially screen the intrinsic properties of a MWNT surface, and provide a BSA-MWNT with a new biological identity [30,109]. The compositions of protein coronas formed on different functionalized MWNTs are complex and unique; for example, liquid chromatography-tandem mass spectrometry was used to show that cMWNTs bound a greater overall number of proteins (and different types of proteins) from cell culture medium relative to pMWNTs [108]. This is important because the biological response of cells to MWNTs typically starts with their binding to the plasma membrane, sometimes via a membrane receptor, and consequent internalization inside a vesicle and ultimately into the cell [30,106,109,110].

2.5.2. The Unsuitability of the 2018-pMWNTs as a Replacement for the 2015-pMWNTs

TGA and Raman analyses suggest the 2018-pMWNTs had more defects relative to the 2015-pMWNTs (Figures 2.3 and 2.4), and the XPS elemental analysis of the 2018-pMWNTs revealed the lowest surface oxygen levels of the four MWNT products (Table 2.5). The differences in the surface chemistry and structural defects of the 2018-pMWNTs (relative to the 2015-pMWNTs) could therefore have an effect on the protein corona formed when each BSA-pMWNT suspension was prepared. In fact, the relative concentration of MWNTs observed in BSA-MWNT

suspensions prepared with the 2018-pMWNTs was ~34% less than that for the 2015-pMWNT suspension (Table 2.2). The differences in the surface chemistry and structural defects could also have had an effect on the protein corona formed when each BSA-pMWNT suspension was mixed with the DMEM/FBS cell culture medium and then presented to cells. However, further studies would be required to quantify protein corona differences with these two pMWNT lots and their effects on RAW 264.7 cell proliferation and accumulation. Nonetheless, it is straight-forward to conclude that RAW 264.7 macrophages respond differently to BSA-pMWNT suspensions prepared with the 2018-pMWNT powder, and that the lot of 2018-pMWNTs is not a suitable replacement for the lot of 2015-pMWNTs.

2.5.3. The Suitability of the 2018-cMWNTs as a Replacement for the 2015-cMWNTs

There are many similarities in the physicochemical properties of the 2015-cMWNT and 2018-cMWNT powders. The carbon purities of the 2015-cMWNTs and 2018-cMWNTs determined by combustion analyses (94.30% and 94.19%, respectively) were in close agreement (Table 2.1), as were the carbon purities (94.37% and 95.57%, respectively) determined by XPS (Table 2.5). The XPS-determined surface oxygen percentages of the 2015-cMWNTs and 2018-cMWNTs were similar (5.63% and 4.43%, respectively), and the 0.060-oxygen/carbon ratio of the 2015-cMWNTs was only slightly greater than the 0.046-oxygen/carbon ratio of the 2018-cMWNTs (Table 2.5). The TGA-determined weight loss observed between 180 and 450 °C corresponding to surface oxides was also greater for the 2015-cMWNTs relative to the 2018-cMWNTs (Table 2.2; 9.3% and 3.0%, respectively). However, the shapes of the predominant TGA peaks of the 2015-cMWNTs and 2018-cMWNTs were quite similar (Figure 2.3), as were their oxidation temperatures (630 °C and 601 °C, respectively). Substantial differences in the

levels of elements determined by ICP-MS were not observed between the 2015-cMWNTs and 2018-cMWNTs (Table A1). The TEM-determined outside diameters of the 2015-cMWNTs and 2018-cMWNTs (19 ± 5 nm and 21.4 ± 4 nm, respectively) and inside diameters (5.7 ± 1.7 nm and 5.6 ± 2.1 nm, respectively) were also comparable (Table 2.3). Additionally, HR-TEM imaging of the 2015-cMWNTs and 2018-cMWNTs did not reveal any striking differences in morphologies (Figures A6-A10). Somewhat surprisingly, the BET-determined SSA of the 2018-cMWNTs (~286 m^2/g) was roughly twice that of the 2015-cMWNTs (~144 m^2/g). However, the Raman spectral profiles and the I_D/I_G ratios of the 2015-cMWNTs and 2018-cMWNTs (1.78 and 1.76, respectively) were highly comparable (Figure 2.4), as were their XRD patterns (Figure A11) and XPS C1s and O1s spectral profiles (Figures A12 and A13). Finally, both the 2015-cMWNTs and 2018-cMWNTs displayed a carbonyl vibrational stretching mode at ~1724 cm^{-1} in their FTIR spectra supporting the manufacturer's claim that the cMWNTs were carboxylated (Figure 2.5).

Suspensions of BSA-coated cMWNTs prepared with the 2015-cMWNT and 2018-cMWNT powders were also quite similar. As shown in Table 2.2, the relative concentrations of suspended MWNTs (~496 and ~456 μg/mL, respectively), the DLS-determined hydrodynamic diameters (~86 and ~84 nm, respectively), and the zeta potentials (~34 and ~33 mV, respectively) of the two BSA-cMWNT suspensions were quite comparable. Most importantly, Figure 2.1 shows that the 24-h proliferation of RAW 264.7 macrophages cultured with BSA-cMWNT suspensions prepared with the 2015-cMWNT and 2018-cMWNT powders were statistically similar up to the highest concentration tested (200 μg cMWNTs/mL). Ultimately, while every physicochemical parameter was not identical, the combined results indicate that the 2018 production lot of cMWNTs is a strong candidate as a suitable replacement for the 2015 lot of cMWNTs for the

purpose of studying the biological response of mammalian macrophages to functionalized MWNTs.

2.6. CONCLUSIONS

A comprehensive physicochemical characterization of two commercial lots of CVD-synthesized pMWNTs and cMWNTs revealed many similarities between the two cMWNT products and several key differences between the two pMWNT products. The 2018-pMWNTs displayed less oxidative stability, a higher defect density, and a smaller amount of surface oxygen species relative to the 2015-pMWNTs. Additionally, the concentration of pMWNTs that could be suspended by BSA with the 2018-pMWNTs was significantly lower relative to the 2015-pMWNTs. Most importantly, while the 24-h proliferation of RAW 264.7 macrophages cultured with BSA-suspensions of 2015-pMWNTs were statistically similar to the proliferation of cells observed with the two BSA-cMWNT suspensions, the 24-h proliferation of RAW 264.7 cells incubated with BSA-suspensions of 2018-pMWNTs was not. Specifically, the 24-h proliferation of cells incubated with BSA-suspensions of 2018-pMWNTs at 100 μg/mL was ~20% lower relative to BSA-suspensions of 2015-pMWNTs at 100 μg/mL, even though the amount of the 2018-pMWNTs accumulated by cells was ~16% less relative to the amount of 2015-pMWNTs accumulated by cells. Furthermore, a 72-h IC-50 of ~90 μg pMWNTs/mL was determined for RAW 264.7 cells with BSA-suspensions of 2018-pMWNTs, making the 2018-pMWNTs significantly more toxic than the 2015-pMWNTs.

The differences in the surface chemistry and structural defects of the 2018-pMWNTs relative to the 2015-pMWNTs likely influenced the protein corona that was formed when BSA-

pMWNT suspensions were prepared, which in turn could affect the binding and subsequent accumulation of the 2018-pMWNTs by RAW 264.7 cells. Reactive structural defects, a key determinant of toxicity, also likely influenced the diminished 24-h proliferation of RAW 264.7 cells, as well as, the 72-h toxicity observed with the 2018-pMWNTs. This work therefore demonstrates (i) the difficulty in assessing the role of a single physicochemical property of a MWNT product to an observed biological response, (ii) that subtle physicochemical differences can have a significant effect on the response of biological cells to a MWNT product, and (iii) that production-lot consistency must be considered when assessing the toxicity or biological activity of MWNTs and other carbon nanomaterials.

2.7. REFERENCES

1. Shen, H.; Liu, T.; Qin, D.; Bo, X.; Wang, L.; Wang, F.; Yuan, Q.; Wagberg, T.; Hu, G.; Zhou, M. Wearable carbon nanotube devices for sensing. In *Industrial Applications of Carbon Nanotubes*; Elsevier: Amsterdam, The Netherlands, 2017; pp. 179–199.

2. Rashid, M.; Ralph, S.F. Carbon nanotube membranes: Synthesis, properties, and future filtration applications. *Nanomaterials* **2017**, *7*, 99 (28 pp).

3. Jafari, S. Engineering applications of carbon nanotubes. In *Carbon Nanotube-Reinforced Polymers*; Elsevier: Amsterdam, The Netherlands, 2018; pp. 25–40.

4. Jayaraman, T.; Murthy, A.P.; Elakkiya, V.; Chandrasekaran, S.; Nithyadharseni, P.; Khan, Z.; Senthil, R.A.; Shanker, R.; Raghavender, M.; Kuppusami, P. Recent development on carbon based heterostructures for their applications in energy and environment: A review. *J. Ind. Eng. Chem.* **2018**, *64*, 16–59.

5. Sarkar, B.; Mandal, S.; Tsang, Y.F.; Kumar, P.; Kim, K.-H.; Ok, Y.S. Designer carbon nanotubes for contaminant removal in water and wastewater: A critical review. *Sci. Total Environ.* **2018**, *612*, 561–581.

6. Wang, R.; Xie, L.; Hameed, S.; Wang, C.; Ying, Y. Mechanisms and applications of carbon nanotubes in terahertz devices: A review. *Carbon* **2018**, *132*, 42–58.

7. Schroeder, V.; Savagatrup, S.; He, M.; Lin, S.; Swager, T.M. Carbon nanotube chemical sensors. *Chem. Rev.* **2018**, *119*, 599–663.

8. Cardenas, J.A.; Andrews, J.B.; Noyce, S.G.; Franklin, A.D. Carbon nanotube electronics for IoT sensors. *Nano Futures* **2020**, *4*, 012001 (11 pp).

9. Kumar, S.; Rani, R.; Dilbaghi, N.; Tankeshwar, K.; Kim, K.-H. Carbon nanotubes: A novel material for multifaceted applications in human healthcare. *Chem. Soc. Rev.* **2017**, *46*, 158–196.

10. Sheikhpour, M.; Golbabaie, A.; Kasaeian, A. Carbon nanotubes: A review of novel strategies for cancer diagnosis and treatment. *Mater. Sci. Eng. C* **2017**, *76*, 1289–1304.

11. Sireesha, M.; Jagadeesh Babu, V.; Kranthi Kiran, A.S.; Ramakrishna, S. A review on carbon nanotubes in biosensor devices and their applications in medicine. *Nanocomposites* **2018**, *4*, 36–57.

12. Raphey, V.; Henna, T.; Nivitha, K.; Mufeedha, P.; Sabu, C.; Pramod, K. Advanced biomedical applications of carbon nanotube. *Mater. Sci. Eng. C* **2019**, *100*, 616–630.

13. Lorite, G.S.; Pitkänen, O.; Mohl, M.; Kordas, K.; Koivisto, J.T.; Kellomäki, M.; Mendonça, M.C.P.; de Jesus, M.B. Carbon nanotube-based matrices for tissue engineering. In *Materials for Biomedical Engineering*; Elsevier: Amsterdam, The Netherlands, 2019; pp. 323–353.

14. Kaur, J.; Gill, G.S.; Jeet, K. Applications of carbon nanotubes in drug delivery: A comprehensive review. In *Characterization and Biology of Nanomaterials for Drug Delivery*; Elsevier: Amsterdam, The Netherlands, 2019; pp. 113–135.

15. Anzar, N.; Hasan, R.; Tyagi, M.; Yadav, N.; Narang, J. Carbon nanotube-A review on Synthesis, Properties and plethora of applications in the field of biomedical science. *Sens. Int.* **2020**, *1*, 100003 (10 pp).

16. Liné, C.; Larue, C.; Flahaut, E. Carbon nanotubes: Impacts and behaviour in the terrestrial ecosystem-A review. *Carbon* **2017**, *123*, 767–785.

17. Narei, H.; Ghasempour, R.; Akhavan, O. Toxicity and safety issues of carbon nanotubes. In *Carbon Nanotube-Reinforced Polymers*; Elsevier: Amsterdam, The Netherlands, 2018; pp. 145–171.

18. Chen, M.; Zhou, S.; Zhu, Y.; Sun, Y.; Zeng, G.; Yang, C.; Xu, P.; Yan, M.; Liu, Z.; Zhang, W. Toxicity of carbon nanomaterials to plants, animals and microbes: Recent progress from 2015-present. *Chemosphere* **2018**, *206*, 255–264.

19. Kane, A.B.; Hurt, R.H.; Gao, H. The asbestos-carbon nanotube analogy: An update. *Toxicol. Appl. Pharmacol.* **2018**, *361*, 68–80.

20. Francis, A.P.; Devasena, T. Toxicity of carbon nanotubes: A review. *Toxicol. Ind. Health* **2018**, *34*, 200–210.

21. Mohanta, D.; Patnaik, S.; Sood, S.; Das, N. Carbon nanotubes: Evaluation of toxicity at biointerfaces. *J. Pharm. Anal.* **2019**, *9*, 293–300.

22. Prajapati, S.K.; Malaiya, A.; Kesharwani, P.; Soni, D.; Jain, A. Biomedical applications and toxicities of carbon nanotubes. *Drug Chem. Toxicol.* **2020**, doi:10.1080/01480545.2019.1709492 (16 pp).

23. Kolosnjaj-Tabi, J.; Just, J.; Hartman, K.B.; Laoudi, Y.; Boudjemaa, S.; Alloyeau, D.; Szwarc, H.; Wilson, L.J.; Moussa, F. Anthropogenic carbon nanotubes found in the airways of Parisian children. *EBioMedicine* **2015**, *2*, 1697–1704.

24. De Volder, M.F.; Tawfick, S.H.; Baughman, R.H.; Hart, A.J. Carbon nanotubes: Present and future commercial applications. *Science* **2013**, *339*, 535–539.

25. Pettitt, M.E.; Lead, J.R. Minimum physicochemical characterisation requirements for nanomaterial regulation. *Environ. Int.* **2013**, *52*, 41–50.

26. Birch, M.E.; Ruda-Eberenz, T.A.; Chai, M.; Andrews, R.; Hatfield, R.L. Properties that influence the specific surface areas of carbon nanotubes and nanofibers. *Ann. Occup. Hyg.* **2013**, *57*, 1148–1166.

27. Rashad, A.; Noaman, R.; Mohammed, S.; Yousif, E. Synthesis of carbon nanotube: A review. *J. Nanosci. Technol.* **2016**, *2*, 155–162.

28. Malikov, E.Y.; Muradov, M.B.; Akperov, O.H.; Eyvazova, G.M.; Puskás, R.; Madarász, D.; Nagy, L.; Kukovecz, Á.; Kónya, Z. Synthesis and characterization of polyvinyl alcohol based multiwalled carbon nanotube nanocomposites. *Phys. E Low-Dimens. Syst. Nanostruct.* **2014**, *61*, 129–134.

29. Boverhof, D.R.; David, R.M. Nanomaterial characterization: Considerations and needs for hazard assessment and safety evaluation. *Anal. Bioanal. Chem.* **2010**, *396*, 953–961.

30. Podila, R.; Brown, J.M. Toxicity of engineered nanomaterials: A physicochemical perspective. *J. Biochem. Mol. Toxicol.* **2013**, *27*, 50–55.

31. Fadeel, B.; Fornara, A.; Toprak, M.S.; Bhattacharya, K. Keeping it real: The importance of material characterization in nanotoxicology. *Biochem. Biophys. Res. Commun.* **2015**, *468*, 498–503.

32. Gunsolus, I.L.; Haynes, C.L. Analytical aspects of nanotoxicology. *Anal. Chem.* **2016**, *88*, 451–479.

33. DeLoid, G.M.; Cohen, J.M.; Pyrgiotakis, G.; Demokritou, P. Preparation, characterization, and in vitro dosimetry of dispersed, engineered nanomaterials. *Nat. Protoc.* **2017**, *12*, 355–371.

34. Krug, H.F. The uncertainty with nanosafety: Validity and reliability of published data. *Colloids Surf. B Biointerfaces* **2018**, *172*, 113–117.

35. Aillon, K.L.; Xie, Y.; El-Gendy, N.; Berkland, C.J.; Forrest, M.L. Effects of nanomaterial physicochemical properties on in vivo toxicity. *Adv. Drug Deliv. Rev.* **2009**, *61*, 457–466.

36. Hussain, M.; Kabir, M.; Sood, A. On the cytotoxicity of carbon nanotubes. *Curr. Sci.* **2009**, *96*, 664–673.

37. Johnston, H.J.; Hutchison, G.R.; Christensen, F.M.; Peters, S.; Hankin, S.; Aschberger, K.; Stone, V. A critical review of the biological mechanisms underlying the in vivo and in vitro toxicity of carbon nanotubes: The contribution of physico-chemical characteristics. *Nanotoxicology* **2010**, *4*, 207–246.

38. Beg, S.; Rizwan, M.; Sheikh, A.M.; Hasnain, M.S.; Anwer, K.; Kohli, K. Advancement in carbon nanotubes: Basics, biomedical applications and toxicity. *J. Pharm. Pharmacol.* **2011**, *63*, 141–163.

39. Kaiser, J.-P.; Roesslein, M.; Buerki-Thurnherr, T.; Wick, P. Carbon nanotubes-curse or blessing. *Curr. Med. Chem.* **2011**, *18*, 2115–2128.

40. Liu, Y.; Zhao, Y.; Sun, B.; Chen, C. Understanding the toxicity of carbon nanotubes. *Acc. Chem. Res.* **2013**, *46*, 702–713.

41. Salamon, A.W. The current world of nanomaterial characterization: Discussion of analytical instruments for nanomaterial characterization. *Environ. Eng. Sci.* **2013**, *30*, 101–108.

42. Tessonnier, J.-P.; Rosenthal, D.; Hansen, T.W.; Hess, C.; Schuster, M.E.; Blume, R.; Girgsdies, F.; Pfänder, N.; Timpe, O.; Su, D.S. Analysis of the structure and chemical properties of some commercial carbon nanostructures. *Carbon* **2009**, *47*, 1779–1798.

43. Rausch, J.; Zhuang, R.-C.; Mäder, E. Surfactant assisted dispersion of functionalized multi-walled carbon nanotubes in aqueous media. *Compos. Part A Appl. Sci. Manuf.* **2010**, *41*, 1038–1046.

44. Levine, K.E.; Han, L.; McWilliams, A.C.; Essader, A.S.; Amato, K.E.; Fernando, R.A.; Browning, D.B.; Greene, L.C.; Ensor, D.S.; Walker, N.J. Characterization of an assortment

of commercially available multiwalled carbon nanotubes. *Microchim. Acta* **2014**, *181*, 171–179.

45. White, C.M.; Banks, R.; Hamerton, I.; Watts, J.F. Characterisation of commercially CVD grown multi-walled carbon nanotubes for paint applications. *Prog. Org. Coat.* **2016**, *90*, 44–53.

46. Richman, E.K.; Hutchison, J.E. The nanomaterial characterization bottleneck. *ACS Nano* **2009**, *3*, 2441–2446, doi:10.1021/nn901112p.

47. Crist, R.M.; Grossman, J.H.; Patri, A.K.; Stern, S.T.; Dobrovolskaia, M.A.; Adiseshaiah, P.P.; Clogston, J.D.; McNeil, S.E. Common pitfalls in nanotechnology: Lessons learned from NCI's nanotechnology characterization laboratory. *Integr. Biol.* **2013**, *5*, 66–73.

48. Jones, C.P.; Jurkschat, K.; Crossley, A.; Banks, C.E. Multi-walled carbon nanotube modified basal plane pyrolytic graphite electrodes: Exploring heterogeneity, electro-catalysis and highlighting batch to batch variation. *J. Iran. Chem. Soc.* **2008**, *5*, 279–285.

49. Braun, E.I.; Pantano, P. The importance of an extensive elemental analysis of single-walled carbon nanotube soot. *Carbon* **2014**, *77*, 912–919.

50. Wang, R.; Meredith, A.N.; Lee, M., Jr.; Deutsch, D.; Miadzvedskaya, L.; Braun, E.; Pantano, P.; Harper, S.; Draper, R. Toxicity assessment and bioaccumulation in zebrafish embryos exposed to carbon nanotubes suspended in Pluronic® F-108. *Nanotoxicology* **2016**, *10*, 689–698.

51. Wang, R.; Lee, M.; Kinghorn, K.; Hughes, T.; Chuckaree, I.; Lohray, R.; Chow, E.; Pantano, P.; Draper, R. Quantitation of cell-associated carbon nanotubes: Selective binding and accumulation of carboxylated carbon nanotubes by macrophages. *Nanotoxicology* **2018**, *12*, 677–698.

52. Nakata, T. Destruction of challenged endotoxin in a dry heat oven. *PDA J. Pharm. Sci. Technol.* **1994**, *48*, 59–63.

53. Yehia, H.N.; Draper, R.K.; Mikoryak, C.; Walker, E.K.; Bajaj, P.; Musselman, I.H.; Daigrepont, M.C.; Dieckmann, G.R.; Pantano, P. Single-walled carbon nanotube interactions with HeLa cells. *J. Nanobiotechnol.* **2007**, *5*, 8 (17 pp).

54. Wang, R.; Hughes, T.; Beck, S.; Vakil, S.; Li, S.; Pantano, P.; Draper, R.K. Generation of toxic degradation products by sonication of Pluronic® dispersants: Implications for nanotoxicity testing. *Nanotoxicology* **2013**, *7*, 1272–1281.

55. Wang, R.; Mikoryak, C.; Li, S.; Bushdiecker, D., II; Musselman, I.H.; Pantano, P.; Draper, R.K. Cytotoxicity screening of single-walled carbon nanotubes: Detection and removal of

cytotoxic contaminants from carboxylated carbon nanotubes. *Mol. Pharm.* **2011**, *8*, 1351–1361.

56. Wang, R.; Mikoryak, C.; Chen, E.; Li, S.; Pantano, P.; Draper, R.K. Gel electrophoresis method to measure the concentration of single-walled carbon nanotubes extracted from biological tissue. *Anal. Chem.* **2009**, *81*, 2944–2952.

57. Braun, E.I.; Huang, A.; Tusa, C.A.; Yukica, M.A.; Pantano, P. Use of Raman spectroscopy to identify carbon nanotube contamination at an analytical balance workstation. *J. Occup. Environ. Hyg.* **2016**, *13*, 915–923.

58. Thompson, C.M.; Occhialini, G.; McCandless, G.T.; Alahakoon, S.B.; Cameron, V.; Nielsen, S.O.; Smaldone, R.A. Computational and experimental studies on the effects of monomer planarity on covalent organic framework formation. *J. Am. Chem. Soc.* **2017**, *139*, 10506–10513.

59. Brown, A.T.; Thomas, M.C.; Chabal, Y.J.; Balkus, K.J., Jr. Nanocast carbon microsphere flowers from a lanthanum-based template. *Mater. Lett.* **2019**, *234*, 224–227.

60. Veyan, J.-F.; de Obaldia, E.; Alcantar-Peña, J.J.; Montes-Gutierrez, J.; Arellano-Jimenez, M.J.; Yacaman, M.J.; Auciello, O. Argon atoms insertion in diamond: New insights in the identification of carbon C 1s peak in X-ray photoelectron spectroscopy analysis. *Carbon* **2018**, *134*, 29–36.

61. Perkins, C.K.; Mansergh, R.H.; Park, D.-H.; Nanayakkara, C.E.; Ramos, J.C.; Decker, S.R.; Huang, Y.; Chabal, Y.J.; Keszler, D.A. Aqueous process to limit hydration of thin-film inorganic oxides. *Solid State Sci.* **2016**, *61*, 106–110.

62. Allegri, M.; Perivoliotis, D.K.; Bianchi, M.G.; Chiu, M.; Pagliaro, A.; Koklioti, M.A.; Trompeta, A.-F.A.; Bergamaschi, E.; Bussolati, O.; Charitidis, C.A. Toxicity determinants of multi-walled carbon nanotubes: The relationship between functionalization and agglomeration. *Toxicol. Rep.* **2016**, *3*, 230–243.

63. Guo, L.; Von Dem Bussche, A.; Buechner, M.; Yan, A.; Kane, A.B.; Hurt, R.H. Adsorption of essential micronutrients by carbon nanotubes and the implications for nanotoxicity testing. *Small* **2008**, *4*, 721–727.

64. Casey, A.; Herzog, E.; Lyng, F.; Byrne, H.; Chambers, G.; Davoren, M. Single walled carbon nanotubes induce indirect cytotoxicity by medium depletion in A549 lung cells. *Toxicol. Lett.* **2008**, *179*, 78–84.

65. Catelas, I.; Petit, A.; Zukor, D.J.; Antoniou, J.; Huk, O.L. TNF-α secretion and macrophage mortality induced by cobalt and chromium ions in vitro-Qualitative analysis of apoptosis. *Biomaterials* **2003**, *24*, 383–391.

66. Kónya, Z.; Zhu, J.; Niesz, K.; Mehn, D.; Kiricsi, I. End morphology of ball milled carbon nanotubes. *Carbon* **2004**, *42*, 2001–2008.

67. Chen, S.; Hu, S.; Smith, E.F.; Ruenraroengsak, P.; Thorley, A.J.; Menzel, R.; Goode, A.E.; Ryan, M.P.; Tetley, T.D.; Porter, A.E. Aqueous cationic, anionic and non-ionic multi-walled carbon nanotubes, functionalised with minimal framework damage, for biomedical application. *Biomaterials* **2014**, *35*, 4729–4738.

68. Lehman, J.H.; Terrones, M.; Mansfield, E.; Hurst, K.E.; Meunier, V. Evaluating the characteristics of multiwall carbon nanotubes. *Carbon* **2011**, *49*, 2581–2602.

69. Wepasnick, K.A.; Smith, B.A.; Bitter, J.L.; Fairbrother, D.H. Chemical and structural characterization of carbon nanotube surfaces. *Anal. Bioanal. Chem.* **2010**, *396*, 1003–1014.

70. Wu, Z.; Hamilton, R.F., Jr.; Wang, Z.; Holian, A.; Mitra, S. Oxidation debris in microwave functionalized carbon nanotubes: Chemical and biological effects. *Carbon* **2014**, *68*, 678–686.

71. Andrews, R.; Jacques, D.; Qian, D.; Dickey, E. Purification and structural annealing of multiwalled carbon nanotubes at graphitization temperatures. *Carbon* **2001**, *39*, 1681–1687.

72. Figarol, A.; Pourchez, J.; Boudard, D.; Forest, V.; Berhanu, S.; Tulliani, J.-M.; Lecompte, J.-P.; Cottier, M.; Bernache-Assollant, D.; Grosseau, P. Thermal annealing of carbon nanotubes reveals a toxicological impact of the structural defects. *J. Nanoparticle Res.* **2015**, *17*, 194 (14 pp).

73. Gong, H.; Kim, S.-T.; Lee, J.D.; Yim, S. Simple quantification of surface carboxylic acids on chemically oxidized multi-walled carbon nanotubes. *Appl. Surf. Sci.* **2013**, *266*, 219–224.

74. Datsyuk, V.; Kalyva, M.; Papagelis, K.; Parthenios, J.; Tasis, D.; Siokou, A.; Kallitsis, I.; Galiotis, C. Chemical oxidation of multiwalled carbon nanotubes. *Carbon* **2008**, *46*, 833–840.

75. Bom, D.; Andrews, R.; Jacques, D.; Anthony, J.; Chen, B.; Meier, M.S.; Selegue, J.P. Thermogravimetric analysis of the oxidation of multiwalled carbon nanotubes: Evidence for the role of defect sites in carbon nanotube chemistry. *Nano Lett.* **2002**, *2*, 615–619.

76. McKee, G.S.; Vecchio, K.S. Thermogravimetric analysis of synthesis variation effects on CVD generated multiwalled carbon nanotubes. *J. Phys. Chem. B* **2006**, *110*, 1179–1186.

77. Zhao, Z.; Yang, Z.; Hu, Y.; Li, J.; Fan, X. Multiple functionalization of multi-walled carbon nanotubes with carboxyl and amino groups. *Appl. Surf. Sci.* **2013**, *276*, 476–481.

78. Jain, S.; Thakare, V.S.; Das, M.; Godugu, C.; Jain, A.K.; Mathur, R.; Chuttani, K.; Mishra, A.K. Toxicity of multiwalled carbon nanotubes with end defects critically depends on their functionalization density. *Chem. Res. Toxicol.* **2011**, *24*, 2028–2039.

79. Jorio, A.; Pimenta, M.; Souza Filho, A.; Saito, R.; Dresselhaus, G.; Dresselhaus, M. Characterizing carbon nanotube samples with resonance Raman scattering. *New J. Phys.* **2003**, *5*, 139 (18 pp).

80. Dresselhaus, M.S.; Jorio, A.; Hofmann, M.; Dresselhaus, G.; Saito, R. Perspectives on carbon nanotubes and graphene Raman spectroscopy. *Nano Lett.* **2010**, *10*, 751–758.

81. Li, J.; Chen, C.; Zhang, S.; Wang, X. Surface functional groups and defects on carbon nanotubes affect adsorption–desorption hysteresis of metal cations and oxoanions in water. *Environ. Sci. Nano* **2014**, *1*, 488–495.

82. Liu, H.; Wang, J.; Wang, J.; Cui, S. Sulfonitric treatment of multiwalled carbon nanotubes and their dispersibility in water. *Materials* **2018**, *11*, 2442 (18 pp).

83. Osswald, S.; Havel, M.; Gogotsi, Y. Monitoring oxidation of multiwalled carbon nanotubes by Raman spectroscopy. *J. Raman Spectrosc. Int. J. Orig. Work in all Asp. Raman Spectrosc. Incl. High. Order Process. Brillouin Rayleigh Scatt.* **2007**, *38*, 728–736.

84. Mohanapriya, S.; Sridhar, P.; Pitchumani, S.; Shukla, A. Influence of surface pretreatment of MWNTs support on PEFC performance. *ECS Trans.* **2010**, *28*, 43–53.

85. Malikov, E.; Akperov, O.; Muradov, M.; Eyvazova, G.; Maharramov, A.; Kukovecz, A.; Konya, Z. Oxidation of multiwalled carbon nanotubes using different oxidation agents like nitric acid and potassium permanganate. *News Baku University*, 2014, Volume 4, pp. 49–59.

86. Raza, M.A.; Kanwal, Z.; Riaz, S.; Naseem, S. Synthesis, characterization and antibacterial properties of nano-sized cobalt particles. In Proceedings of the 2016 World Congress on Advances in Civil, Enviromental, and Materials Research (ACEM16), Jeju Island, Korea, 28 August–1 September 2016; Volume 28, 6 pp.

87. Cheng, J.; Zhang, X.; Ye, Y. Synthesis of nickel nanoparticles and carbon encapsulated nickel nanoparticles supported on carbon nanotubes. *J. Solid State Chem.* **2006**, *179*, 91–95.

88. Hamilton, R.F.; Wu, Z.; Mitra, S.; Holian, A. The effects of varying degree of MWCNT carboxylation on bioactivity in various in vivo and in vitro exposure models. *Int. J. Mol. Sci.* **2018**, *19*, 354 (15 pp).

89. Boehm, H.P. Surface oxides on carbon and their analysis: A critical assessment. *Carbon* **2002**, *40*, 145–149.

90. Okpalugo, T.; Papakonstantinou, P.; Murphy, H.; McLaughlin, J.; Brown, N. High resolution XPS characterization of chemical functionalised MWCNTs and SWCNTs. *Carbon* **2005**, *43*, 153–161.

91. Pacheco, F.G.; Cotta, A.A.; Gorgulho, H.F.; Santos, A.P.; Macedo, W.A.; Furtado, C.A. Comparative temporal analysis of multiwalled carbon nanotube oxidation reactions: Evaluating chemical modifications on true nanotube surface. *Appl. Surf. Sci.* **2015**, *357*, 1015–1023.

92. Yamada, Y.; Yasuda, H.; Murota, K.; Nakamura, M.; Sodesawa, T.; Sato, S. Analysis of heat-treated graphite oxide by X-ray photoelectron spectroscopy. *J. Mater. Sci.* **2013**, *48*, 8171–8198.

93. Belin, T.; Epron, F. Characterization methods of carbon nanotubes: A review. *Mater. Sci. Eng. B* **2005**, *119*, 105–118.

94. Mejia, J.; Tichelaar, F.; Saout, C.; Toussaint, O.; Masereel, B.; Mekhalif, Z.; Lucas, S.; Delhalle, J. Effects of the dispersion methods in Pluronic F108 on the size and the surface composition of MWCNTs and their implications in toxicology assessment. *J. Nanoparticle Res.* **2011**, *13*, 655–667.

95. Nishikiori, H.; Tanigaki, T.; Endo, M.; Fujii, T. Quantitative characterization of acidic groups on acid-treated multi-walled carbon nanotubes using 1-aminopyrene as a fluorescent probe. *Carbon* **2014**, *66*, 560–566.

96. Trykowski, G.; Biniak, S.; Stobinski, L.; Lesiak, B. Preliminary investigations into the purification and functionalization of multiwall carbon nanotubes. *Acta Phys. Pol.-Ser. A Gen. Phys.* **2010**, *118*, 515–518.

97. Stéfani, D.; Paula, A.J.; Vaz, B.G.; Silva, R.A.; Andrade, N.F.; Justo, G.Z.; Ferreira, C.V.; Souza Filho, A.G.; Eberlin, M.N.; Alves, O.L. Structural and proactive safety aspects of oxidation debris from multiwalled carbon nanotubes. *J. Hazard. Mater.* **2011**, *189*, 391–396.

98. Kouklin, N.; Tzolov, M.; Straus, D.; Yin, A.; Xu, J. Infrared absorption properties of carbon nanotubes synthesized by chemical vapor deposition. *Appl. Phys. Lett.* **2004**, *85*, 4463–4465.

99. Fenoglio, I.; Greco, G.; Tomatis, M.; Muller, J.; Raymundo-Pinero, E.; Béguin, F.; Fonseca, A.; Nagy, J.B.; Lison, D.; Fubini, B. Structural defects play a major role in the acute lung toxicity of multiwall carbon nanotubes: Physicochemical aspects. *Chem. Res. Toxicol.* **2008**, *21*, 1690–1697.

100. Liu, Y.K.; Ye, J.; Han, Q.L.; Tao, R.; Liu, F.; Wang, W. Toxicity and bioactivity of cobalt nanoparticles on the monocytes. *Orthop. Surg.* **2015**, *7*, 168–173.

101. Charlier, J.-C. Defects in carbon nanotubes. *Acc. Chem. Res.* **2002**, *35*, 1063–1069.

102. Liu, Y.; Liggio, J.; Li, S.-M.; Breznan, D.; Vincent, R.; Thomson, E.M.; Kumarathasan, P.; Das, D.; Abbatt, J.; Antiñolo, M.; et al. Chemical and toxicological evolution of carbon nanotubes during atmospherically relevant aging processes. *Environ. Sci. Technol.* **2015**, *49*, 2806−2814.

103. Magrez, A.; Kasas, S.; Salicio, V.; Pasquier, N.; Seo, J.W.; Celio, M.; Catsicas, S.; Schwaller, B.; Forró, L. Cellular toxicity of carbon-based nanomaterials. *Nano Lett.* **2006**, *6*, 1121–1125.

104. Firme, C.P., III; Bandaru, P.R. Toxicity issues in the application of carbon nanotubes to biological systems. *Nanomed. Nanotechnol. Biol. Med.* **2010**, *6*, 245–256.

105. Bai, W.; Raghavendra, A.; Podila, R.; Brown, J.M. Defect density in multiwalled carbon nanotubes influences ovalbumin adsorption and promotes macrophage activation and cD4+ T-cell proliferation. *Int. J. Nanomed.* **2016**, *11*, 4357–4371.

106. Jiang, W.; Wang, Q.; Qu, X.; Wang, L.; Wei, X.; Zhu, D.; Yang, K. Effects of charge and surface defects of multi-walled carbon nanotubes on the disruption of model cell membranes. *Sci. Total Environ.* **2017**, *574*, 771–780.

107. Li, Y.; Cao, J. The impact of multi-walled carbon nanotubes (MWCNTs) on macrophages: Contribution of MWCNT characteristics. *Sci. China Life Sci.* **2018**, *61*, 1333–1351.

108. Muller, J.; Huaux, F.; Fonseca, A.; Nagy, J.B.; Moreau, N.; Delos, M.; Raymundo-Pinero, E.; Béguin, F.; Kirsch-Volders, M.; Fenoglio, I. Structural defects play a major role in the acute lung toxicity of multiwall carbon nanotubes: Toxicological aspects. *Chem. Res. Toxicol.* **2008**, *21*, 1698–1705.

109. Shannahan, J.H.; Brown, J.M.; Chen, R.; Ke, P.C.; Lai, X.; Mitra, S.; Witzmann, F.A. Comparison of nanotube–protein corona composition in cell culture media. *Small* **2013**, *9*, 2171–2181.

110. Ajdary, M.; Moosavi, M.A.; Rahmati, M.; Falahati, M.; Mahboubi, M.; Mandegary, A.; Jangjoo, S.; Mohammadinejad, R.; Varma, R.S. Health concerns of various nanoparticles: A review of their in vitro and in vivo toxicity. *Nanomaterials* **2018**, *8*, 634 (28 pp).

2.8. APPENDIX

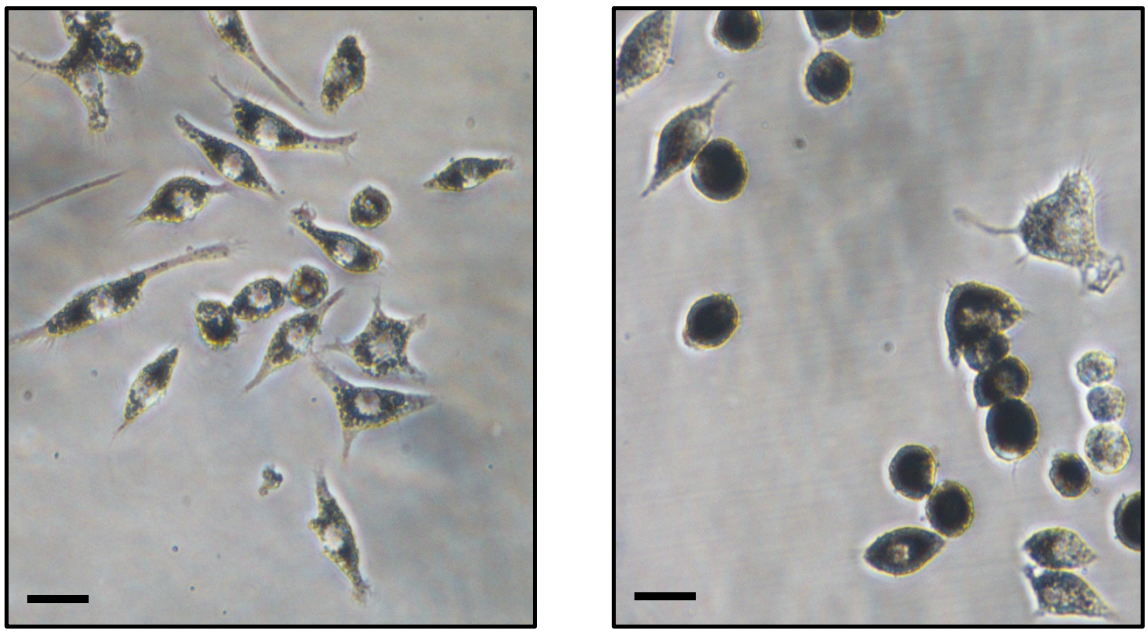

Figure A1. Representative phase contrast images acquired using an inverted light microscope (Nikon SMZ745T) equipped with a digital camera (Nikon DS-Fi2) of RAW 264.7 cells following 72 h of incubation with 125-µg/mL BSA-suspensions of 2015-pMWNTs (left) or 2018-pMWNTs (right). The scale bars represent 10 µm.

Table A1. ICP-MS analyses of pMWNT and cMWNT powders.

		2015-pMWNTs	2015-cMWNTs	2018-pMWNTs	2018-cMWNTs	MDL[1]
Aluminum	Al	35.622	7.103	11.496	7.953	0.012
Antimony	Sb	0.138	0.149	0.025	0.005	0.002
Arsenic	As	0.245	0.052	0.345	0.052	0.052
Barium	Ba	2.991	2.954	1.562	1.159	0.001
Beryllium	Be	0.014	0.014	0.014	0.014	0.014
Bismuth	Bi	0.003	0.001	0.022	0.470	0.001
Boron	B	14.625	18.884	9.189	10.957	0.174
Cadmium	Cd	0.029	0.004	0.005	0.008	0.004
Calcium	Ca	1,186.718	1,343.731	651.953	1,419.302	0.063
Chromium	Cr	8.932	0.837	3.714	18.656	0.005
Cobalt	Co	24.597	2.679	1,241.834	4.183	0.014
Copper	Cu	2.169	0.348	0.649	3.231	0.012
Gallium	Ga	0.026	0.005	0.015	0.012	0.005
Germanium	Ge	0.030	0.014	0.014	0.014	0.014
Gold	Au	0.003	0.003	0.003	0.003	0.003
Iron	Fe	1,689.820	28.690	475.353	123.964	0.022
Lead	Pb	0.543	0.033	0.076	0.721	0.005
Lithium	Li	0.130	0.085	0.092	0.055	0.001
Magnesium	Mg	197.304	198.221	66.185	174.402	0.002
Manganese	Mn	7.283	0.308	5.841	12.433	0.007
Molybdenum	Mo	110.852	4.300	3.237	9.936	0.009
Nickel	Ni	5,591.619	78.091	8.792	97.132	0.029
Niobium	Nb	0.189	0.012	0.008	0.007	0.002
Platinum	Pt	0.008	0.050	0.048	0.008	0.008
Potassium	K	20.245	30.789	13.715	33.888	0.021
Silver	Ag	1.675	0.318	0.009	0.014	0.003
Sodium	Na	78.042	72.556	31.502	49.317	0.004
Strontium	Sr	3.462	5.675	2.028	5.344	0.001
Tantalum	Ta	0.002	0.004	0.001	0.001	0.001
Thallium	Tl	0.001	0.001	0.001	0.001	0.001
Tin	Sn	0.147	0.035	0.145	0.179	0.003
Titanium	Ti	5.707	6.533	1.246	0.804	0.011
Tungsten	W	0.097	0.025	0.048	0.023	0.003
Vanadium	V	0.121	0.070	0.938	0.292	0.004
Zinc	Zn	10.458	2.308	1.314	2.965	0.018
Zirconium	Zr	16.233	479.190	119.315	42.038	0.010

[1] MDL = Method detection limit; MWNT data listed in blue font indicates that the observed results were at or below the MDL. All values are reported in units of ppm.

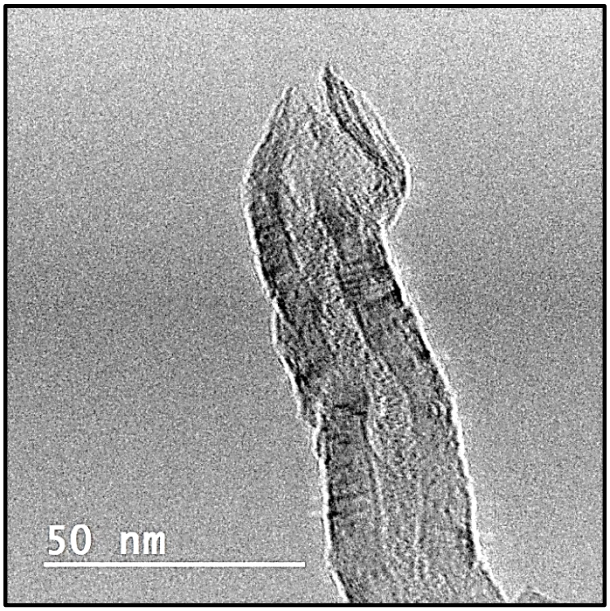

Figure A2. Representative HR-TEM image of a 2015-pMWNT highlighting asymmetric (bent) sidewall damage and a partially-collapsed, open-end.

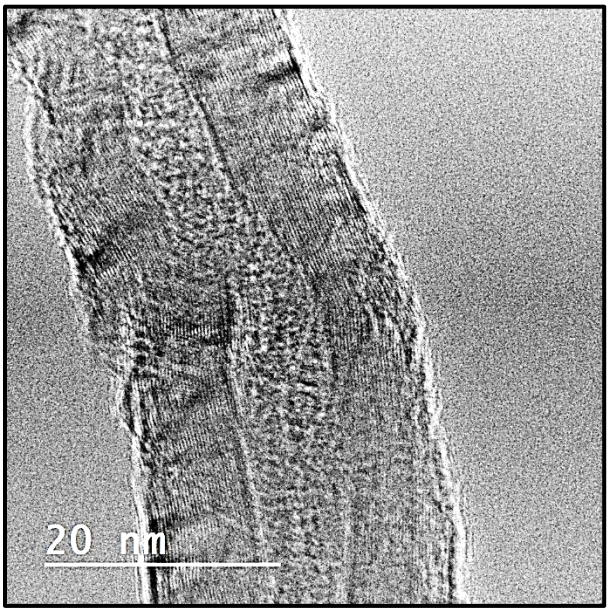

Figure A3. Representative HR-TEM image of a 2015-pMWNT showing asymmetric (bent) sidewall damage.

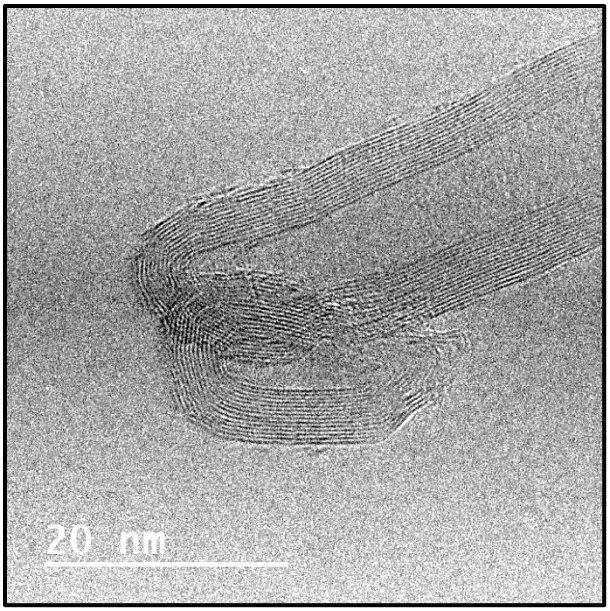

Figure A4. Representative HR-TEM image of a 2018-pMWNT highlighting a closed-end nanotube architecture, a hollow inner-cylinder, and a unique anomaly at the tip.

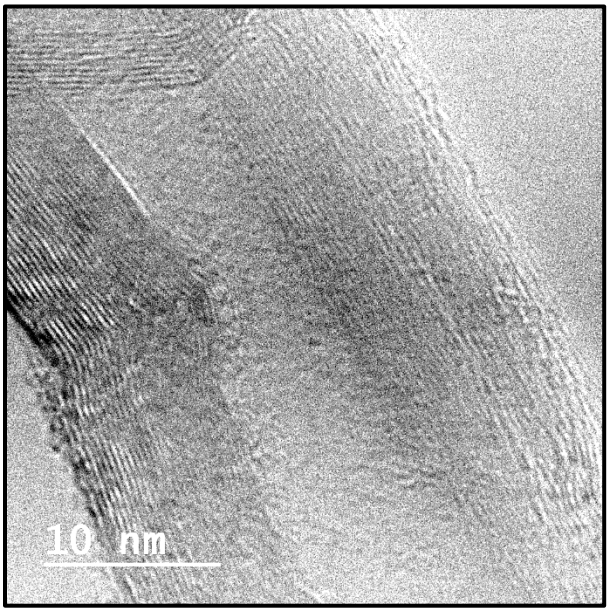

Figure A5. Representative HR-TEM image of a 2018-pMWNT highlighting asymmetric (bent) sidewall damage and sidewall debris.

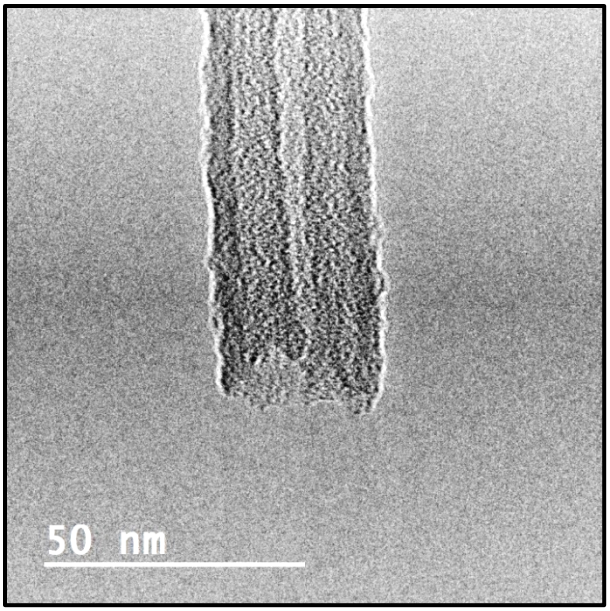

Figure A6. Representative HR-TEM image of a 2015-cMWNT highlighting a relatively symmetric, open-end nanotube architecture.

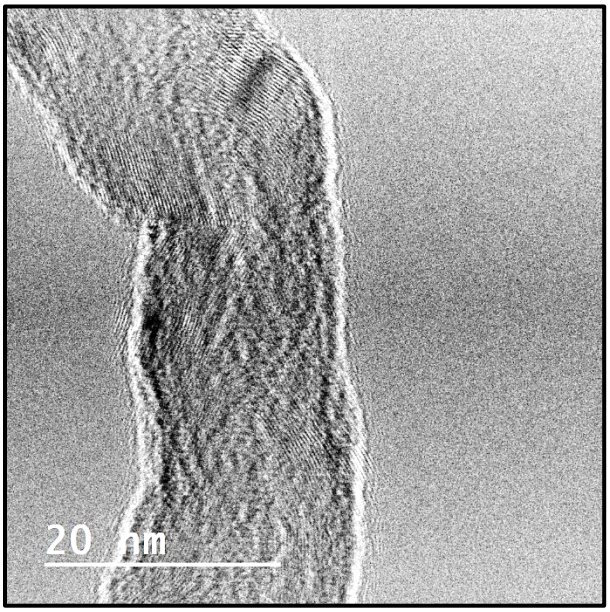

Figure A7. Representative HR-TEM image of a 2015-cMWNT highlighting asymmetric (bent) sidewall damage.

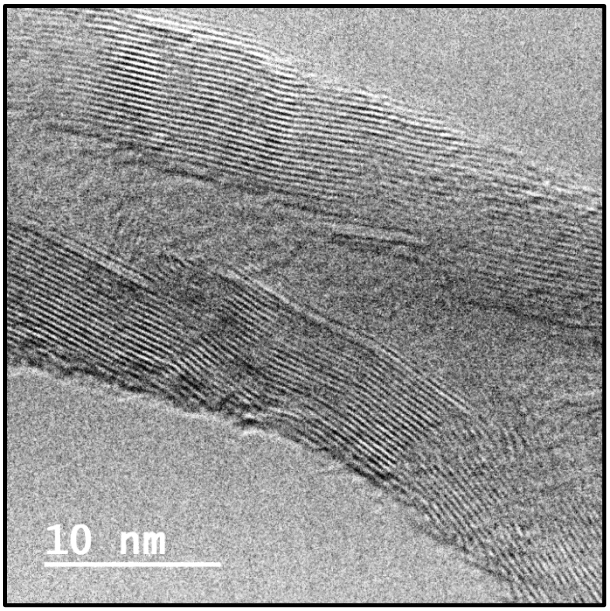

Figure A8. Representative HR-TEM image of a 2018-cMWNT highlighting a fishbone-type structure.

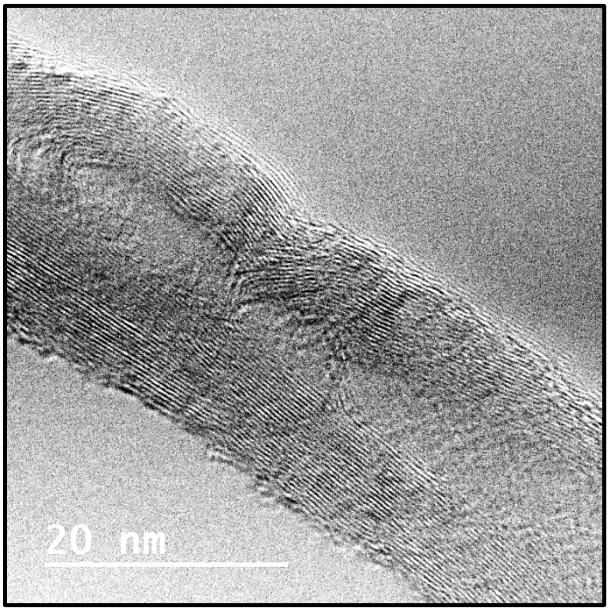

Figure A9. Representative HR-TEM image of a 2018-cMWNT highlighting cup-stacked structures.

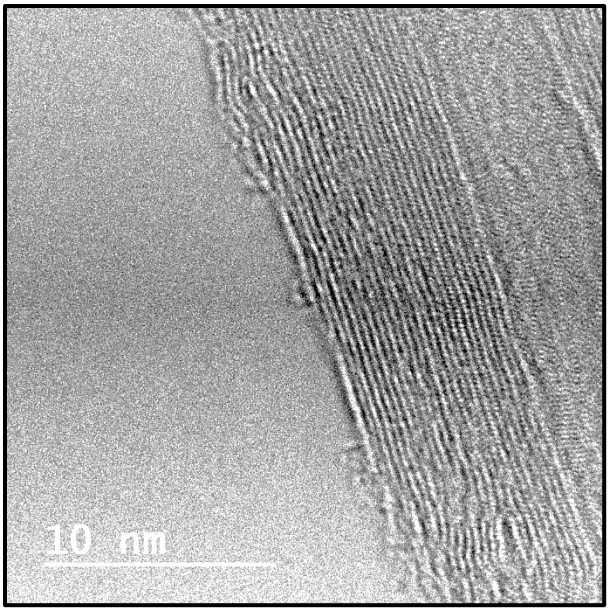

Figure A10. Representative HR-TEM image of a 2018-cMWNT highlighting a hollow inner-cylinder, sidewall damage, and sidewall debris.

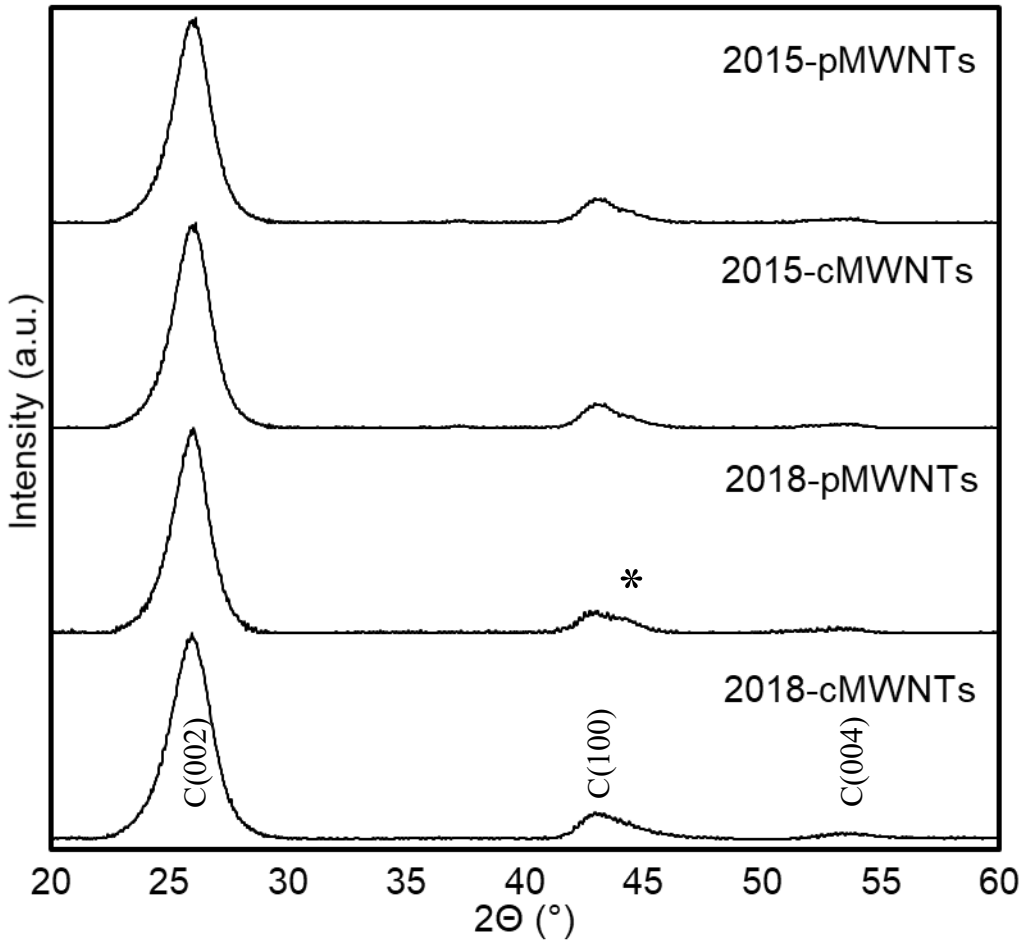

Figure A11. Representative XRD patterns (normalized and offset for clarity) of the 2015-pMWNT, 2015-cMWNT, 2018-pMWNT, and 2018-cMWNT powders showing the C(002), C(100), and C(004) diffraction peaks characteristic of an ideal graphite phase.

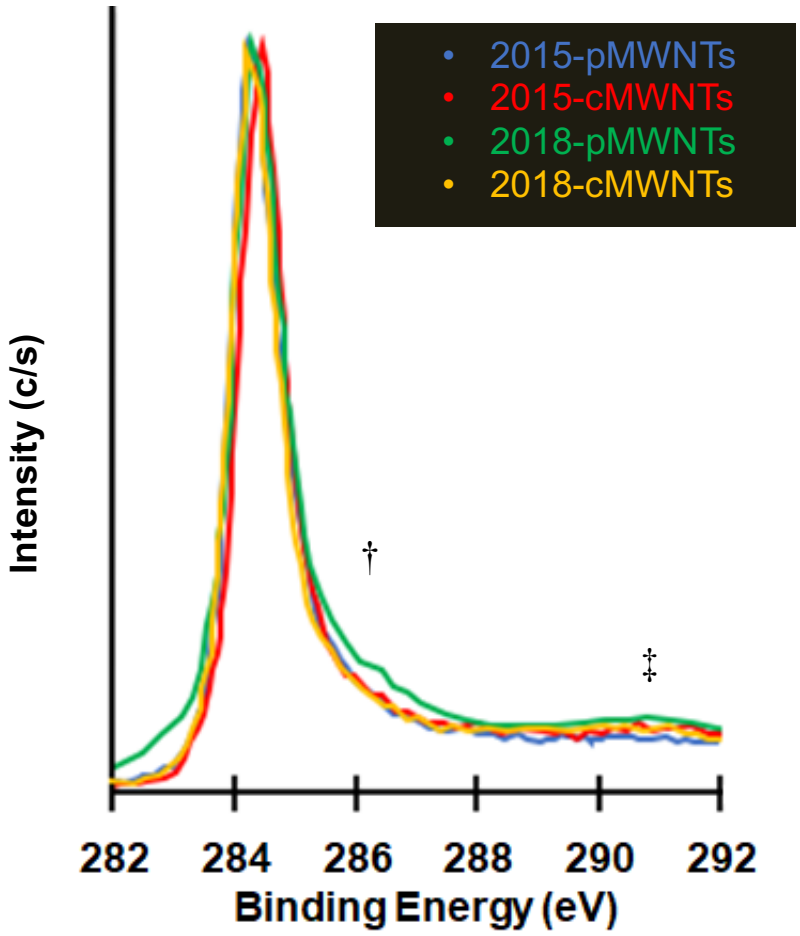

Figure A12. Representative C1s XPS spectra of the four MWNT powders where the major peak corresponds to sp^2-hybridized carbons is centered: at 284.2 eV (FWHM ≈ 1.1 eV) for the 2015-pMWNTs, at 284.4 eV (FWHM ≈ 1.1 eV) for the 2015-cMWNTs, at 284.2 eV (FWHM ≈ 1.1 eV) for the 2018-pMWNTs, and at 284.3 eV (FWHM ≈ 0.9 eV) for the 2018-cMWNTs. Note, that the <0.2 eV-differences in the positions of the main C1s peaks were considered insignificant based on the instrument's energy resolution. The symbols represent C1s spectral regions associated with sp^3-hybridized carbons (†) and the π–π* electronic transition that is representative of disordered sp^2 carbons (‡); see text for details.

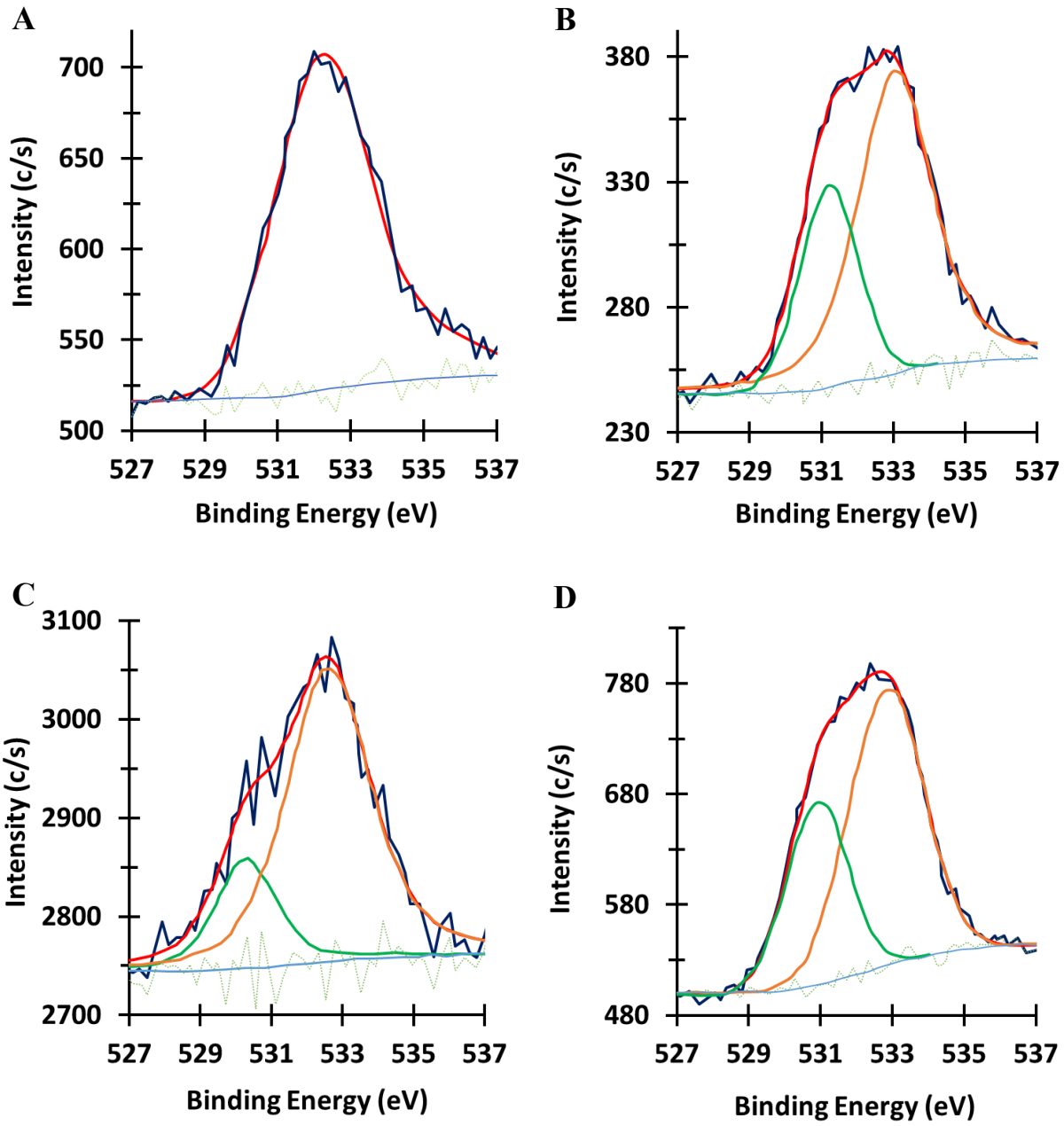

Figure A13. Representative O1s XPS spectra of (**A**) 2015-pMWNTs, (**B**) 2015-cMWNTs, (**C**) 2018-pMWNTs, and (**D**) 2018-cMWNTs. The dark-blue traces are the raw spectra and the red traces are the corresponding best fits; the light-green and light-blue traces are the raw background and smoothed background, respectively; and the green and orange traces are the best Gaussian fits.

Table A2. Analyses of the O1s XPS peaks from pMWNT and cMWNT powders.[1]

MWNT Powder	Peak 1 Position (eV)	Peak 1 Area (%)	Peak 2 Position (eV)	Peak 2 Area (%)
2015-pMWNTs	532.14	100	----	----
2015-cMWNTs	533.09	70	531.25	30
2018-pMWNTs	532.67	78	530.37	22
2018-cMWNTs	532.86	65	530.94	35

[1] Peak positions and areas determined from the O1s XPS peaks of the four MWNT powders shown in Figure A13. The O1s peak of the 2015-pMWNTs could be fit with a single Gaussian peak, while the O1s peaks of the other MWNT powders were best fit with two Gaussian peaks.

CHAPTER 3

SCAVENGER RECEPTOR A1 MEDIATES THE UPTAKE OF CARBOXYLATED AND PRISTINE MULTI-WALLED CARBON NANOTUBES COATED WITH BOVINE SERUM ALBUMIN

Authors - Mai Huynh [1], Carole Mikoryak [2], Paul Pantano [1], and Rockford Draper [1,2]

[1] Department of Chemistry and Biochemistry, BE 26
The University of Texas at Dallas
800 West Campbell Road, Richardson, Texas, 75080-3021

[2] Department of Biological Sciences, BSB 12
The University of Texas at Dallas
800 West Campbell Road, Richardson, Texas, 75080-3021

This chapter has been reproduced from *Nanomaterials* **2021**, *11*, 539, doi:10.3390/nano11020539.

3.1. ABSTRACT

Previously, we noted that carboxylated multi-walled carbon nanotubes (cMWNTs) coated with Pluronic® F-108 (PF108) bound to and were accumulated by macrophages, but that pristine multi-walled carbon nanotubes (pMWNTs) coated with PF108 were not (Wang et al., *Nanotoxicology* **2018**, *12*, 677). Subsequent studies with Chinese hamster ovary (CHO) cells that overexpressed scavenger receptor A1 (SR-A1) and with macrophages derived from mice knocked out for SR-A1 provided evidence that SR-A1 was a receptor of PF108-cMWNTs (Wang et al., *Nanomaterials* (Basel) **2020**, *10*, 2417). Herein, we replaced the PF108 coat with bovine serum albumin (BSA) to investigate how a BSA corona affected the interaction of multi-walled carbon nanotubes (MWNTs) with cells. Both BSA-coated cMWNTs and pMWNTs bound to and were accumulated by RAW 264.7 macrophages, although the cells bound two times more BSA-coated cMWNT than pMWNTs. RAW 264.7 cells that were deleted for SR-A1 using CRISPR-Cas9 technology had markedly reduced binding and accumulation of both BSA-coated cMWNTs and pMWNTs, suggesting that SR-A1 was responsible for the uptake of both MWNT types. Moreover, CHO cells that ectopically expressed SR-A1 accumulated both MWNT types, whereas wild-type CHO cells did not. One model to explain these results is that SR-A1 can interact with two structural features of BSA-coated cMWNTs, one inherent to the oxidized nanotubes (such as COOH and other oxidized groups) and the other provided by the BSA corona; whereas SR-A1 only interacts with the BSA corona of BSA-pMWNTs.

3.2. INTRODUCTION

The interaction of engineered nanoparticles (ENPs) with cells is influenced by a corona of macromolecules that deposit on the ENP surface from the surrounding biological fluid. What macromolecules (often proteins) adhere to the ENP depends on the properties of the macromolecules and on the ENP surface structure, charge, hydrophobicity, and geometry [1–4]. Corona components may provide dominant features controlling the interaction of ENPs with specific cell surface binding sites, often followed by ENP internalization and a subsequent response by the cells. Understanding what corona components are present on an ENP and how they interface with cells is thus important to provide rational approaches for promoting positive responses, such as targeted drug delivery, or mitigating negative responses, such as toxicity. However, understanding ENP coronas is challenging because the potential corona components in complex biological environments are diverse and the properties of ENP surfaces vary widely. Single-walled carbon nanotubes (SWNTs) and multi-walled carbon nanotubes (MWNTs) are ENPs whose production is increasing due to a wide variety of commercial applications [5–8]. Nevertheless, there is ample evidence that carbon nanotubes can be toxic to organisms and the environment, but how their coronas contribute to toxicity is not well understood [9–11].

We previously noted that carboxylated MWNTs (cMWNTs) coated with Pluronic® F-108 (PF108) preferentially bind to and are accumulated by cells, whereas PF108-coated pristine MWNTs (pMWNTs) do not bind and are poorly accumulated [12]. This suggested that surface receptors on macrophages selectively bind cMWNTs but not pMWNTs. Class A scavenger receptors (SR-As) are membrane glycoproteins that bind polyanionic compounds and modified proteins [13–15], and several observations in the literature implicate SR-As as potential carbon

nanotube receptors. For example, there is evidence that SWNTs coated with bovine serum albumin (BSA) are targeted to SR-As [16]. There are also numerous reports where antagonists of class A-type 1 scavenger receptors (SR-A1s) affect cell responses to MWNTs: The accumulation of cMWNTs by RAW 264.7 macrophages correlated with the extent of carboxylation and was inhibited by the SR-A1 antagonist dextran sulfate [17]; the rate of apoptosis induced by MWNTs could be reduced by treating the cells with poly I, another SR-A antagonist [18]; and the accumulation of FITC-BSA-coated MWNTs by THP-1 macrophages was inhibited by the SR-A antagonist fucoidan [19]. In addition, Hirano et al. found that MWNTs suspended in the surfactant Pluronic® F-68 bind to MARCO (SR-A6) receptors on Chinese hamster ovary (CHO) cells overexpressing MARCO [20]. We also observed that dextran sulfate reduced the binding of PF108-coated cMWNTs by macrophages [12].

Recently, we reported that alveolar macrophages derived from SR-A1 knockout mice did not bind or accumulate PF108-cMWNTs whereas they were accumulated by CHO cells that ectopically expressed SR-A1 [21] - strong evidence that SR-A1 is a receptor for PF108-coated cMWNTs. An interesting feature of PF108-coated cMWNTs is that they bind strongly to cells in the absence of serum or any exogenous protein, suggesting that a protein corona is not required for cMWNT binding to SR-A1 [12]. Thus, some inherent structural feature of oxidized MWNTs, perhaps carboxyl groups, carbonyl groups, or hydroxyl groups, appear sufficient for interaction with SR-A1.

Herein, we replaced the PF108 coat with BSA and studied the interaction of cMWNTs and pMWNTs bearing a BSA corona with CHO cells that ectopically express SR-A1 and with RAW 264.7 cells that were deleted for SR-A1 using CRISPR-Cas9 technology. CHO cells expressing

SR-A1, but not wild-type (WT) CHO cells, accumulated both BSA-coated cMWNTs and pMWNTs, but the amount of cMWNTs accumulated was 2–3 times more than pMWNTs. WT RAW 264.7 cells also accumulated approximately 2 times more BSA-coated cMWNTs than pMWNTs. Moreover, in binding studies with RAW 264.7 cells at 4 °C in the absence of serum, more BSA-cMWNTs than BSA-pMWNTs were bound. These data suggest that there are more binding sites on the RAW 264.7 cell surface for BSA-cMWNTs than BSA-pMWNTs. To assess what effect the absence of SR-A1 would have, the binding and accumulation of BSA-coated cMWNTs and pMWNTs to SR-A1 knockout RAW 264.7 cells at 4 °C in medium without serum and at 37 °C was measured. The amount of bound or accumulated BSA-MWNTs in the knockout SR-A1 cells was significantly decreased for both BSA-pMWNTs and BSA-cMWNTs compared to the WT RAW 264.7 cells. These observations suggest that pMWNTs coated with a BSA protein corona gain the capacity to bind SR-A1. Overall, BSA-cMWNTs have enhanced binding to SR-A1 above that observed with BSA-pMWNTs, emphasizing the differences between how BSA-coated cMWNTs and pMWNTs interact with receptors. Models to account for the differences are presented.

3.3. MATERIALS AND METHODS

3.3.1. Nanomaterials

The pMWNT (product 1236-YJS, lot 2015-041709) and cMWNT (product 1256-YJF, lot 2015-070510) powders were purchased from Nanostructured & Amorphous Materials, Inc. (Houston, TX). pMWNTs and cMWNTs were synthesized using a Fe/Co/Ni-catalyzed chemical vapor deposition process. Caution should be taken, and a fine particulate respirator and other appropriate personal protective equipment should be worn when handling dry MWNT powders.

Both MWNT products were reported by the manufacturer to be >95% in purity and to contain MWNTs with outer diameters of 10–20 nm, inner diameters of 5–10 nm, and lengths of 0.5–2 μm. The cMWNT powder was oxidized using sulfuric acid and potassium permanganate and comprised 1.9–2.1% by weight carboxylic acid groups. Elemental analyses of MWNTs were performed using a previously described combustion analysis technique [22]. The combined carbon, hydrogen, nitrogen, sulfur, and oxygen elemental analyses of the pMWNTs and cMWNTs were 99.52% and 98.18%, respectively, indicative of MWNT powders that are essentially metal-free. An extensive physical and chemical characterization of the pMWNTs and cMWNTs powders appears elsewhere [23]. The major similarities of the pMWNTs and cMWNTs were their outer diameters (18 ± 3 nm and 19 ± 5 nm, respectively) and inner diameters (5.6 ± 1.3 and 5.7 ± 1.7 nm, respectively), as determined using transmission electron microscopy. The key difference was the presence of a carbonyl vibrational stretching mode associated with carboxyl groups in the infrared spectra of cMWNTs that was not observed in the pMWNT spectra.

3.3.2. Chemicals and Solutions

Dulbecco's modified Eagle medium (DMEM) and Ham's F-12K complete medium were purchased from Gibco (Grand Island, NY, USA), fetal bovine serum (FBS) from Atlanta Biologicals (Flowery Branch, GA, USA), Geneticin® selective antibiotic G418 sulfate from Calbiochem (San Diego, CA, USA), and Accumax™ from Innovative Cell Technologies (San Diego, CA, USA). SR-AI/MSR Alexa Fluor® 488-conjugated antibody (R&D Systems cat. No. FAB1797G) and rat IgG2B Alexa Fluor® 488-conjugated Isotype Control (R&D Systems cat. No. IC013G) were purchased from R&D Systems (Minneapolis, MN, USA). Bovine serum albumin (BSA), dextran sulfate (product # D6001), chondroitin sulfate (product # C9819), penicillin

(10,000 U/mL), streptomycin (10 mg/mL), and all other chemicals were purchased from Millipore Sigma (Burlington, MA, USA). All chemicals were used as received. Deionized water (18.3 MΩ·cm) was obtained using a Milli-Q® Integral water purification system (Billerica, MA, USA). Phosphate buffered saline (PBS; 0.8 mM phosphate, 150 mM NaCl, pH 7.4) was sterilized by autoclaving at 121 °C for 45 min. Stock solutions of 100 mg/mL BSA were prepared by dissolving 10 g of BSA in 100 mL of deionized water and adjusting the pH to 7.4. Working solutions of 0.10 mg/mL BSA were prepared by diluting stock BSA solutions with aqueous 10 mM HEPES (pH 7.4) and filtering the solutions through a 0.22-μm pore membrane; stock and working solutions of BSA were stored at 4 °C in the dark.

3.3.3. Cell lines and Cell Culture

Abelson murine leukemia virus transformed RAW 264.7 macrophages were purchased from the American Type Culture Collection (ATCC® TIB-71™; Manassas, VA, USA). A scavenger receptor A1 (SR-A1) knockout RAW 264.7 cell pool was purchased from Synthego Corporation (Silicon Valley, CA, USA). The cell pool was generated using CRISPR-Cas9 technologies with the guide RNA sequence CAGCAUCCUCUCGUUCAUGA. Synthego validated, via genome sequencing, that 70% of the SR-A1 knockout pool of RAW 264.7 cells had insertion(s) or deletion(s) between base pairs 41 and 42 of the SR-A1 gene. Because the site of alteration is at the beginning of the gene, expression of SR-A1.1, which is a splice variant of SR-A1, would also be affected. A dilution scheme was used to clone cells that did not express SR-A1 receptors on their surface. Serial dilutions of the SR-A1 knockout RAW 264.7 cell pool were plated in 96-well plates and incubated for 7 days. Cells that had arisen from a single colony were grown for several passages before selecting clones that lacked surface SR-A1 expression using

immunofluorescence microscopy and flow cytometry. All RAW 264.7 cells and SR-A1 knockout RAW 264.7 cells were grown in DMEM supplemented with 1.5 mg/mL sodium bicarbonate, 10 mM HEPES (pH 7.4), and 10% (v/v) FBS.

Chinese hamster ovary (CHO) cells stably transfected with mouse SR-A1 cDNA (CHO[mSR-AI] cells) were generously provided by Professor Monty Krieger (Massachusetts Institute of Technology) [24]. The control WT CHO cell line for CHO[mSR-AI] cells were CHO-K1 cells (ATCC® CCL-61™). All CHO cells were grown in Ham's F-12K medium supplemented with 2.0 mg/mL sodium bicarbonate, 10 mM HEPES (pH 7.4), 10% (v/v) FBS, 100 units/mL penicillin, and 100 μg/mL streptomycin; the mSR-AI cells were additionally maintained under 0.25 mg/mL G418. The standard incubation conditions for all cell lines were 37 °C in a 5% CO_2 and 95% air environment.

3.3.4. Preparation of BSA-MWNT Suspensions

The sonication and centrifugation protocol described in our previous works [12,25] was used with slight modifications to prepare purified BSA-coated MWNT suspensions, as summarized in Scheme 1. MWNTs were coated with BSA to match the albumin in the FBS used in growth media. A total of 10.0 mg of pMWNT or cMWNT powder was weighed into a pre-cleaned 20-mL glass vial and baked at 200 °C for 2 h to inactivate potential endotoxin contaminants [26]. Next, 10 mL of a 0.10 mg/mL BSA working solution was added to the vial and the mixture was sonicated. Specifically, a single vial was secured in a hanging rack and sonicated for 240 min using an ultrasonic bath sonicator (Elmasonic P30H; Elma Ultrasonic, Singen, Germany) that was operated at 120 W and 37 kHz in a 4 °C cold room. During sonication, the temperature of the bath water was maintained below 18 °C by using a refrigerated water bath

circulator (Isotemp 1006S). After sonication, the solution was divided by transferring 1-mL aliquots into ten 1.5-mL centrifuge tubes. One of the 1-mL aliquots of each non-centrifuged BSA-pMWNT or BSA-cMWNT suspension was set aside as the standard suspension, and each standard solution was serially diluted with a 0.10 mg/mL-BSA working solution. The absorbance at 500 nm of the dilutions determined using a BioTek SynergyMx plate reader (Winooski, VT, USA) was used to construct pMWNT or cMWNT calibration curves. The remaining nine aliquots were centrifuged at 20,000 RCF for 5 min at 4 °C using an Eppendorf 5417R centrifuge to remove MWNT bundles and other impurities, as demonstrated in our previous work [27]. The top 900 µL from each supernatant was collected without disturbing the pellet and combined in a sterile vial to afford ~9 mL of a purified BSA-pMWNT or BSA-cMWNT suspension. The concentration of MWNTs in each purified suspension was determined using the measured absorbance at 500 nm and the calibration curves described above. Purified BSA-MWNT suspensions were stored at 4 °C in the dark.

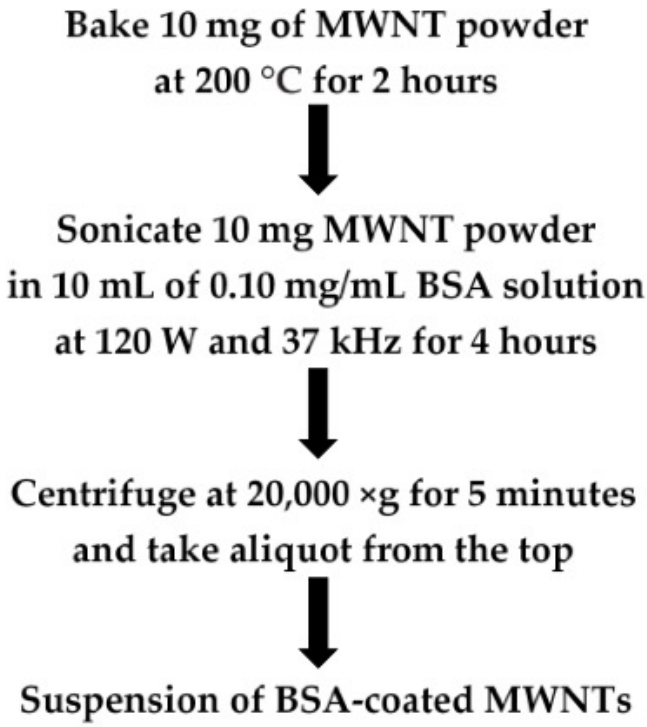

Scheme 1. Preparation of purified BSA-coated MWNT suspensions by sonication and centrifugation.

3.3.5. Characterization of MWNT Suspensions

The particle size distributions, in terms of hydrodynamic diameter, of BSA-MWNT suspensions were determined by dynamic light scattering (DLS). In brief, aliquots of purified pMWNT or cMWNT suspensions were diluted 1:10 in a 0.10 mg/mL BSA working solution and analyzed using a 633-nm laser and a backscatter measurement angle of 173° (Zetasizer Nano-ZS 3600, Malvern Instruments, Worcestershire, UK). The instrument was calibrated with Polybead® standards (Polysciences, Warrington, PA, USA) and ten consecutive 30-s runs were taken per measurement at 25 °C. The hydrodynamic diameter was calculated using a viscosity and refractive

index of 0.8872 cP and 1.330, respectively, for deionized water, and an absorption and refractive index of 0.010 and 1.891, respectively, for MWNTs. Zeta potential values were also determined for purified BSA-coated MWNT suspensions that were diluted 1:10 with deionized water, medium with serum, or serum-free medium. In addition, DLS and zeta potential analyses were performed periodically on purified MWNT suspensions stored at 4 °C to detect any changes. Typically, MWNT suspensions were stable in storage for months, indicated by the lack of aggregates detected by DLS and constant zeta potential results.

3.3.6. Crystal Violet Cell Proliferation Assay

For the assays with RAW 264.7 cells, purified BSA-MWNT suspensions were first diluted with a freshly prepared 0.10 mg/mL-BSA working solution to a concentration twice the desired MWNT concentration to be tested. The diluted MWNT suspensions were then mixed 1:1 in equal volumes with 2X-concentrated medium that contained 3.0 mg/mL sodium bicarbonate, 20 mM HEPES (pH 7.4), 20% (v/v) FBS, 200 units/mL penicillin, and 0.2 mg/mL streptomycin. The result is a test medium with the same concentration of 10 mM HEPES and 10% FBS as the control medium. A total of ~3.5×10^4 RAW 264.7 cells/well were seeded in 48-well plates and incubated at 37 °C overnight before the medium was replaced with freshly prepared control medium or test medium containing MWNTs and incubated for 24 h. At the end of the incubation, cells were washed 3 times with fresh medium, 2 times with PBS, air-dried, and fixed with 4% (w/v) paraformaldehyde in PBS. Cell proliferation was determined using a standardized crystal violet assay, as described in our previous work where it was demonstrated that MWNTs do not interfere with the assay [28].

3.3.7. Quantitation of MWNTs Extracted from Cell Lysates by SDS-PAGE

The SDS-PAGE method with optical detection [29], previously validated by a large-area Raman scan technique [12], was used for quantifying MWNTs extracted from RAW 264.7 cells or CHO cells. In brief, aliquots of known amounts of pMWNT or cMWNT standard suspensions, lysates of control cells, and lysates of cells treated with MWNTs were mixed with 5% 2-mercaptoethanol, 10% glycerol, 62.5 mM Tris-HCl, and 2X-concentrated SDS sample loading buffer to a final concentration of 2% SDS, and boiled for 3 min. Samples at various dilutions and volumes were subsequently loaded into the wells of an SDS-polyacrylamide gel composed of a 4% stacking gel on top of a 10% resolving gel. An electric current was applied at a constant 100 V for 2 h. MWNTs in standard suspensions and in the lysates bind SDS in the sample loading buffer to become negatively charged and migrate toward the anode upon electrophoresis. The large aspect ratio of MWNTs prevents them from sieving through the pores of a 4% polyacrylamide gel mesh; thus, the MWNTs accumulate at the bottom of the sample loading well during electrophoresis and form a sharp dark band. Following electrophoresis, optical images of the gels were obtained using a flatbed scanner (HP Scanjet G3110, Hewlett Packard Enterprise, Fort Collin, CO, USA), and the pixel intensity of each dark band was quantified using ImageJ software (NIH ImageJ system, Bethesda, MD, USA). The known amount of MWNTs in the standards and their corresponding pixel intensities form a linear calibration curve that was used to determine the unknown amount of MWNTs in cell lysates, based on the pixel intensities of lysate bands loaded in the same gel as the standards.

3.3.8. Accumulation of MWNTs by Cells at 37 °C

The following procedure was used to detect the accumulation of pMWNTs and cMWNTs by RAW 264.7 or CHO cells at 37 °C for 24 h. MWNT suspensions were first diluted in a freshly prepared 0.10 mg/mL BSA working solution to twice the desired final MWNT concentrations specified in the experiment. The diluted MWNT suspension samples were then mixed 1:1 with the appropriate 2X-concentrated medium. A total of ~3.5×10^5 cells/well were seeded in 6-well plates and incubated in medium at 37 °C overnight to allow the cells to adhere to the plates. The medium was removed the next day and 2 mL of the appropriate freshly prepared control medium that contained no MWNTs or test medium that contained an MWNT suspension at a specified concentration was added to each well. Cells were incubated in a control or test medium at 37 °C for 24 h, as described in each experiment. At the end of the incubation, the control and test media were removed by aspiration and the cells were washed 3 times with fresh medium followed by 2 washes with PBS. Cells were then lifted off the well using 0.5 mL Accumax™, transferred to a centrifuge tube, and the well was rinsed with 1.5 mL PBS that was subsequently added to the tube to make a final cell suspension of 2 mL/well/tube. Three aliquots of cell suspension, 100 µL each, were used to determine cell counts in each sample using a Beckman Coulter particle counter (Miami, FL, USA) and the cells in the remaining 1.7-mL cell suspension were collected by centrifugation at 1,000× g for 5 min at 4 °C. The cells in the pellet were lysed in 200 µL of cell lysis buffer that contained 0.25 M Tris-HCl (pH 6.8), 8% (w/v) SDS, and 20% (v/v) 2-mercaptoethanol. To ensure complete lysis of the cells, the lysate samples were heated in a boiling water bath for 2 h and then stored at 4 °C. The amounts of MWNTs in the cell lysate samples were determined using the SDS-PAGE method, as described previously herein.

3.3.9. Surface Binding of MWNTs to Cells at 4 °C

To detect and compare the association of pMWNTs and cMWNTs to the surface of RAW 264.7 cells in the absence of endocytic or phagocytic activity, ~5.0×10^5 RAW 264.7 cells/well were first seeded in 6-well plates and incubated in the appropriate medium at 37 °C overnight. Then, the cells were incubated in the appropriate serum-free medium for 2 h at 37 °C to deplete the serum in the cells. In order to incubate cells at a low temperature outside of the 37 °C incubator, the medium was replaced with the respective serum-free medium that additionally did not contain sodium bicarbonate. The 6-well plates were then placed on a shallow ice-water bath and incubated in a 4 °C cold room for 30 min. The appropriate 2X-concentrated, serum- and sodium bicarbonate-free medium was pre-chilled to 4 °C before mixing 1:1 with a MWNT suspension, such that the final test medium contained MWNTs at the desired concentration specified in the experiment. After chilling down to 4 °C, the cells were incubated for 1 h at 4 °C with the appropriate pre-chilled serum- and sodium bicarbonate-free medium that did not contain MWNTs (control), or test serum- and sodium bicarbonate-free medium that contained a MWNT suspension at the specified final MWNT concentration. Because phagocytosis and endocytosis are blocked at low temperature, MWNTs in the test medium were free to interact with cell surface components without subsequently entering the vacuolar compartment of the cells. After incubation, the cells were washed, harvested, and the subsequent procedures for cell counting and lysate preparation were followed, as described in the previous sections. The amounts of cell-surface bound MWNTs in the cell lysate samples were determined using the SDS-PAGE method, as described previously herein.

3.3.10. Dissociation of Bound BSA-cMWNTs and BSA-pMWNTs from RAW 264.7 Cells at 4 °C

MWNTs suspended in a 0.10 mg/mL BSA working solution were mixed with an equal volume of 2X-concentrated, serum- and sodium bicarbonate-free medium to give a final MWNT concentration of 100 μg/mL. Equivalent number of RAW 264.7 cells were seeded in 6-well plates and incubated at 37 °C under standard cell culture conditions for 24 h prior to the experiment. Next, the cells were pre-incubated with serum-free medium (in the absence of MWNTs) for 2 h at 37 °C to deplete the serum in the cells. The cells were then pre-chilled to 4 °C and incubated at 4 °C for 1 h in serum- and sodium bicarbonate-free medium that contained either BSA-pMWNTs or BSA-cMWNTs. Finally, the cells were then incubated with serum- and sodium bicarbonate-free medium for an additional 20, 40, 60, 90, or 120 min, and then washed 3 times with serum- and sodium bicarbonate-free medium, then 2 times with PBS. After incubation, surface-bound MWNTs were extracted and quantified by the SDS-PAGE method, as described previously herein.

3.3.11. Additive Binding Test for BSA-cMWNTs and BSA-pMWNTs to RAW 264.7 Cells

To determine whether BSA-cMWNTs and BSA-pMWNTs use independent surface binding sites, ~5.0×10^5 RAW 264.7 cells/well were first seeded in 6-well plates and incubated in medium at 37 °C overnight. Cells were then incubated in a serum-free medium for 2 h at 37 °C to deplete the serum in the cells. Next, this medium was replaced with a serum-free medium that did not contain sodium bicarbonate. The 6-well plates were placed on a shallow ice-water bath and incubated in a 4 °C cold room for 30 min. A 2X-concentrated, serum- and sodium bicarbonate-free medium was pre-chilled to 4 °C before mixing 1:1 with a MWNT suspension such that the final test serum- and sodium bicarbonate-free medium contained 100 μg/mL MWNTs. After chilling to 4 °C, the cells were incubated with either BSA-cMWNTs or BSA-pMWNTs separately

at 4 °C for 90 min or simultaneously with both ligands at 4 °C for 90 min. In a slightly different experimental design, the ligands were added sequentially, first BSA-cMWNTs for 45 min at 4 °C followed by washing the cells and the addition of BSA-pMWNTs, for 45 min at 4 °C for a total incubation time of 90 minutes. The order of the ligand addition was then reversed with another set of cells. The amounts of cell-surface bound MWNTs in the cell lysate samples were determined using the SDS-PAGE method, as described previously herein.

3.3.12. Surface Binding of MWNTs to RAW 264.7 Cells in the Presence of Dextran Sulfate, an SR-A1 Antagonist

To determine the effects of dextran sulfate on the association of pMWNTs and cMWNTs to the surfaces of RAW 264.7 cells, ~5.0×10^5 RAW 264.7 cells/well were seeded in 6-well plates and incubated in medium at 37 °C overnight. Then, RAW 264.7 cells were incubated in serum-free medium for 2 h at 37 °C to deplete the serum in the cells. To incubate cells at low temperature outside of the 37 °C incubator, the serum-free medium was replaced with serum-free medium that did not contain sodium bicarbonate. The 6-well plates were then placed on a shallow ice-water bath and incubated in a 4 °C cold room for 30 min. A 2X-concentrated, serum- and sodium bicarbonate-free medium was pre-chilled to 4 °C before mixing 1:1 with a MWNT suspension followed by the addition of dextran sulfate (or chondroitin sulfate, a control that is not an SR-A1 antagonist) at various concentrations such that the final test serum- and sodium bicarbonate-free medium contained 100 μg/mL MWNTs. After chilling down to 4 °C, the cells were incubated for 1 h at 4 °C with test serum- and sodium bicarbonate-free medium that contained 100 μg/mL MWNTs, washed 3 times with serum- and sodium bicarbonate-free medium, and then washed 2

times with PBS. In all cases, the amounts of cell-surface bound MWNTs in the cell lysate samples were determined using the SDS-PAGE method, as described previously herein.

3.3.13. Immunofluorescence Microscopy of WT and SR-A1 Knockout RAW 264.7 Cells

A total of ~2 × 10^4 RAW 264.7 cells were seeded on coverslips in 4-well plates and incubated in medium at 37 °C for 48 h to allow the cells to adhere to the plates. RAW 264.7 cells were incubated in serum-free medium for 1 h at 37 °C to deplete the serum in the cells. The cells were washed three times with media and 2 times with PBS. Then the cells were fixed with 4% paraformaldehyde at room temperature for 20 min followed by washing with PBS. The cells were incubated in blocking buffer containing 4% fish gelatin in PBS at room temperature for 1 hour to block non-specific protein-protein interactions. The cells were incubated with mouse SR-AI/MSR Alexa Fluor® 488-conjugated antibody or a rat IgG2B Alexa Fluor® 488-conjugated monoclonal antibody as the isotype control at room temperature for 1 h in the dark; control cells were not treated with any antibody. After rinsing, cell nuclei were stained with Hoechst 33342 dye for 10 min at room temperature. Then the cells were washed two times with PBS to remove excess dye. The coverslips were mounted on the glass slide using Fluoromount-G™. Images were taken with a Nikon Eclipse TE-2000 fluorescence microscope using a 60× oil-immersion objective with a NA of 1.4; the images for Hoechst 33342 (Ex. 350 nm; Em. 435–485 nm) and Alexa Fluor® 488 (Ex. 488 nm; Em. 520–550 nm) were overlaid using ImageJ software.

3.3.14. Flow Cytometry for Surface Receptor(s) on WT and SR-A1 Knockout RAW 264.7 Cells

A total of ~2 × 10^6 RAW 264.7 cells were seeded in 10-mm plates and incubated in medium at 37 °C for 48 h to allow the cells to adhere to the plates. The cells were rinsed and harvested with warm FACS staining buffer (1% BSA in PBS) in 15 mL centrifuge tube followed by

centrifugation (1,000× g) for 5 min. The cells were suspended in 1 mL of FACS staining buffer, then three 100 µL-aliquots of the cell suspension were used to determine cell counts in each aliquot using a Beckman Coulter particle counter. A total of ~1 × 10^6 cells in 100 µL FACS staining buffer were aliquoted into 2 mL tubes. The cells were incubated in blocking buffer containing 5 µg IgG for 15 min at 4 °C to block non-specific protein interactions. The cells were stained with 5 µg mouse SR-AI/MSR Alexa Fluor® 488-conjugated antibody or a rat IgG2B Alexa Fluor® 488-conjugated monoclonal antibody as the isotype control for 30 min at 4 °C in the dark; control cells were not treated with any antibody. Unbound antibody was removed by washing and re-suspending the cells in 1.5 mL FACS staining buffer thrice. The cells were re-suspended in 500 µL of FACS staining buffer for the final flow cytometric analysis. Flow cytometry analysis and data processing were performed using BD Accuri™ C6 Plus flow cytometer and CSampler™ Plus software (Becton and Dickinson Company, Franklin Lakes, NJ, USA) to determine the mean fluorescent index of each sample using a 518–548 nm emission filter.

3.4. RESULTS

3.4.1. Characterization of BSA-MWNT Suspensions

The sonication and centrifugation protocol used to prepare purified BSA-coated MWNT suspensions is shown in Scheme 1. The initial baking step is to inactivate lipopolysaccharide derived from bacteria, should any be present. DLS and zeta potential analyses were used as part of a quality control routine for the preparation of all MWNT suspensions, as previously described [25,27]. Table 3.1 shows few differences in the particle size distributions of BSA-pMWNT and BSA-cMWNT suspensions, and that the zeta potentials for the BSA-cMWNTs in deionized water were slightly more negative than those for the BSA-pMWNTs. Zeta potentials were also

determined for BSA-pMWNTs and BSA-cMWNTs in cell culture medium with and without 10% serum. In both matrices, the values were less negative for both MWNT samples in medium than in water as expected due to the increase in salt and/or serum proteins; the BSA-cMWNTs still had a slightly more negative zeta potential than the BSA-pMWNTs as expected due to the presence of ionized carboxyl groups on the cMWNTs.

Table 3.1. Dynamic light scattering (DLS) particle size and zeta potential analyses of BSA-MWNT suspensions.

MWNT Suspension	DLS [1]		Zeta Potential [2] (mV)		
	HDD (nm)	PDI	Water	Medium + FBS	Medium - FBS
BSA-pMWNTs	83.23	0.20	-31.2	-5.7	-5.6
BSA-cMWNTs	84.18	0.19	-32.5	-6.6	-6.1

[1] Aliquots of purified pristine multi-walled carbon nanotubes (pMWNT) or carboxylated multi-walled carbon nanotubes (cMWNT) suspensions were diluted 1:10 in 0.10 mg/mL BSA working solutions. HDD is the hydrodynamic diameter, and PDI is the polydispersity index. [2] Aliquots of purified pMWNT or cMWNT suspensions were diluted 1:10 in deionized water, medium with fetal bovine serum (FBS), or FBS-free medium.

3.4.2. BSA-pMWNTs and BSA-cMWNTs are not Significantly Toxic to RAW 264.7 Cells

The cell proliferation of RAW 264.7 cells incubated with BSA-pMWNTs or cMWNTs was measured after 24-h exposure to different concentrations of MWNTs up to 200 µg/mL using a previously standardized crystal violet assay [28]. The control in each case was cells exposed to BSA alone. Figure 3.1 shows no significant decline in cell proliferation for RAW 264.7 cells with either BSA-pMWNTs or cMWNTs at the highest concentrations tested (200 µg/mL); however,

exposures longer than 24 h could reveal toxicity. Except where noted, a MWNT concentration of 100 µg/mL was chosen for the majority of experiments involving a constant MWNT concentration.

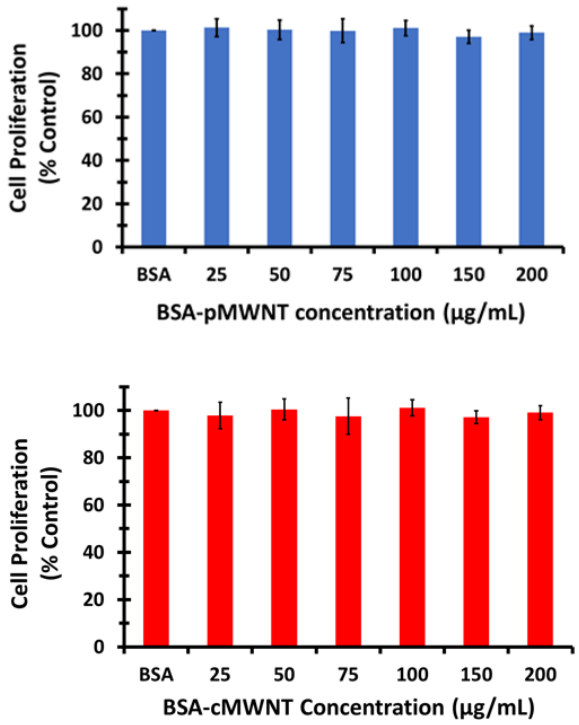

Figure 3.1. Cell proliferation of RAW 264.7 cells cultured with BSA-MWNTs. MWNTs suspended in a 0.10 mg/mL BSA working solution were mixed with an equal volume of 2X-concentrated medium to produce MWNT concentrations shown on the x-axes of the graphs. An equivalent number of cells were seeded in 48-well plates and incubated at 37 °C under standard cell culture conditions for 24 h prior to the experiment. Cell proliferation after incubation with control and test media for 24 h at 37 °C was determined by the crystal violet assay as described in the Methods, where the proliferation of control cells exposed to BSA in the absence of MWNTs was set to 100%. **(Top)** RAW 264.7 macrophage cell proliferation post 24-h incubation with various concentrations of BSA-pMWNTs. **(Bottom)** RAW 264.7 macrophage cell proliferation post 24-h incubation with various concentrations of BSA-cMWNTs. Both data sets are the mean of quadruple samples in three independent experiments ± the standard deviation (SD).

3.4.3. Evidence for BSA-MWNT Receptors on RAW 264.7 Cells

The accumulation of MWNTs by RAW 264.7 cells at 37 °C as a function of the applied BSA-MWNT concentrations between 0 and 200 µg/mL at 37 °C for 24 h was determined for BSA-pMWNTs and cMWNTs (Figure 3.2A). For both, the uptake was linear to ~100 µg/mL and then

began to decline as the concentration approached 200 µg/mL, consistent with a saturable receptor-mediated uptake process. To determine whether the receptors could be saturated when bound MWNTs were not internalized and in the absence of serum that otherwise could complicate the interpretation of the results, MWNT binding to cells was performed at 4 °C in medium without serum. RAW 264.7 cells were incubated with different concentrations of BSA-MWNTs (0–200 µg/mL) at 4 °C for 1 h in serum- and sodium bicarbonate-free medium. As shown in Figure 3.2B, these experiments directly demonstrated that the binding of both MWNT types to the cell surface was a saturable function of the applied MWNT concentration, supporting the idea that there are receptors that bind BSA-coated MWNTs. Note also that more BSA-cMWNTs were bound than BSA-pMWNTs, suggesting that there are differences in the receptor interactions between the two MWNT types.

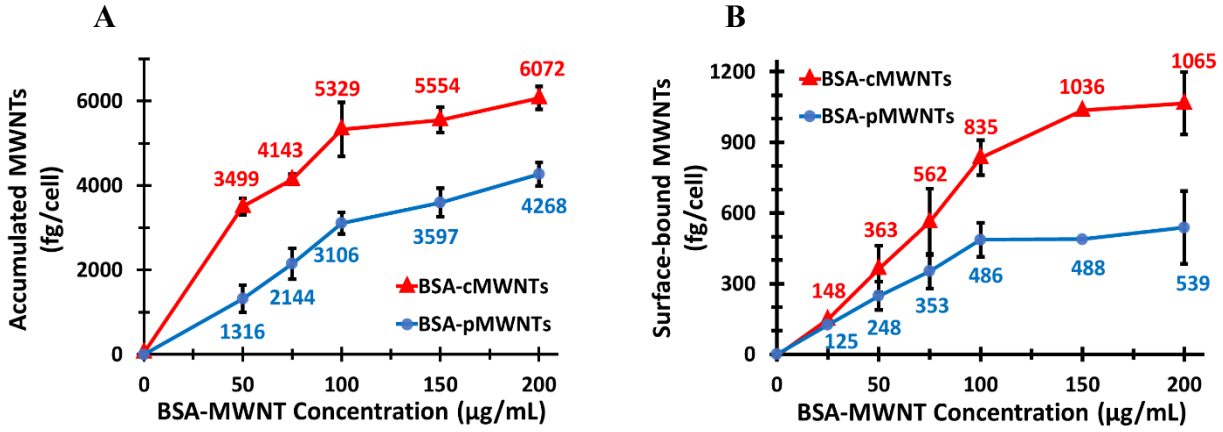

Figure 3.2. Accumulation at 37 °C and surface binding at 4 °C of BSA-MWNTs by RAW 264.7 cells as a function of the applied BSA-MWNT concentration. MWNTs suspended in a 0.10 mg/mL BSA working solution were mixed with an equal volume of 2X-concentrated medium to produce MWNT concentrations shown in the x-axes of the graphs. Exposure to a 0.10 mg/mL BSA working solution alone (in the absence of MWNTs) was the control. **(A)** RAW 264.7 cells in 6-well plates were incubated at 37 °C for 24 h in complete medium with serum that contained either BSA alone, BSA-pMWNTs (blue line), or BSA-cMWNTs (red line). After incubation,

MWNTs were extracted from cells and quantified by the SDS-PAGE method. **(B)** Cells in 6-well plates were pre-incubated with serum-free medium (in the absence of BSA-MWNTs) for 2 h at 37 °C to deplete the serum in the cells. The cells were then pre-chilled to 4 °C and incubated at 4 °C for 1 h in serum- and sodium bicarbonate-free medium that contained either a 0.10 mg/mL BSA working solution without MWNTs, with BSA-pMWNTs (blue line), or with BSA-cMWNTs (red line). After incubation, surface-bound MWNTs were extracted and quantified by the SDS–PAGE method. For both data sets the numbers above the data points are the mean femtograms of MWNTs/cell; each data point is the mean of ≥3 independent experiments ± SD.

To further characterize the ligand/receptor properties of bound BSA-coated MWNTs, the dissociation of bound BSA-cMWNTs and BSA-pMWNTs from cells was measured in the absence of serum at 4 °C. Briefly, RAW 264.7 cells were incubated with BSA-coated MWNTs to allow binding at 4 °C, washed, and further incubated in medium without serum to allow dissociation, followed by quantitating the amount of cell-bound MWNTs as a function of dissociation time. BSA-pMWNTs dissociated very slowly from cells, with more than 80% of the material still bound after 120 min (Figure 3.3, inset). This slow dissociation is not surprising considering that BSA is likely a major determinant of receptor interaction, and there are multiple copies of BSA on each nanotube that may simultaneously interact with multiple receptors, decreasing the probability of dissociation. BSA-cMWNTs' dissociation was biphasic, with about 50% of the bound material dissociating within the first hour, followed by a slowly dissociating component, suggesting that BSA-cMWNTs may contain two binding sites for cells that have different dissociation rates from the two receptor sites. Further, the slowly dissociating component seen with BSA-cMWNTs might share features with the slowly dissociating material observed with BSA-pMWNTs. Regardless of mechanistic details, these data emphasize that the receptor interaction characteristics of BSA-cMWNTs and BSA-pMWNTs are not identical.

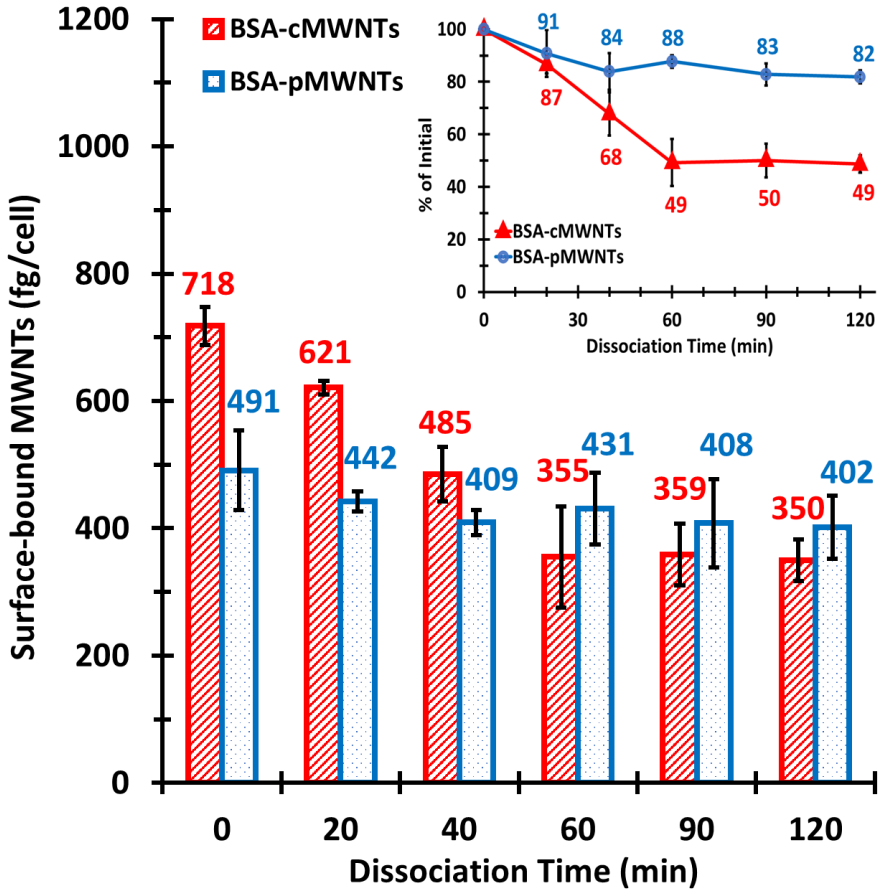

Figure 3.3. Dissociation of bound BSA-cMWNTs and BSA-pMWNTs from RAW 264.7 cells at 4 °C. A total of 100 µg/mL of BSA-cMWNTs or BSA-pMWNTs in serum- and sodium bicarbonate-free medium were incubated with RAW 264.7 cells at 4 °C for 1 h to achieve binding, then washed and incubated in serum- and sodium bicarbonate-free medium for the indicated times, as described in Methods. Surface-bound MWNTs were extracted and quantified by the SDS-PAGE method. The numbers above the bars are the mean femtograms of MWNTs/cell. **Inset:** The data are plotted as the percentage of the initial surface-bound MWNTs at t = 0 min. Data are the mean of ≥3 independent experiments ± SD.

One explanation for the apparent differences between BSA-cMWNTs and BSA-pMWNTs in the number of cell surface binding sites and the differing dissociation kinetics is that there are two independent receptors on these cells - one for BSA-coated cMWNTs and another for BSA-coated pMWNTs. If so, then their binding should be additive at saturation; that is, if BSA-

cMWNTs and BSA-pMWNTs are both added simultaneously, the total cell-associated MWNTs should be the sum of the amount for each when added alone. As shown in Figure 3.4, when cells were incubated with both BSA-cMWNTs and BSA-pMWNTs, the amount bound by cells was greater than for BSA-pMWNTs alone, but did not exceed that of BSA-cMWNTs alone, which is not fully additive. In a slightly different experimental design to test additive binding, the cells were exposed to the ligands sequentially-an experimental design that avoids the possible interaction of cMWNTs and pMWNTs when they are together in medium during binding. Cells were first exposed for 45 min to BSA-cMWNTs alone, followed by washing and exposure for 45 min to BSA-pMWNTs. The order of the two sequential ligand additions was then reversed, with results seen in the last two bars of Figure 3.4. When BSA-cMWNTs were added first, followed by BSA-pMWNTs, there was no additional binding compared to BSA-cMWNTs alone, suggesting that there were no further open sites for BSA-pMWNTs. When BSA-pMWNTs were added first, followed by BSA-cMWNTs, there was additional binding compared to pMWNTs alone, but binding did not exceed that of BSA-cMWNTs alone. Altogether, these data do not fit a simple model of additive binding with two independent receptors each interacting autonomously with the two ligands. Rather, they suggest a semi-additive situation where BSA-cMWNTs can occupy all the sites that BSA-pMWNTs may interact with, but that there are sites for BSA-cMWNTs to which BSA-pMWNTs do not bind.

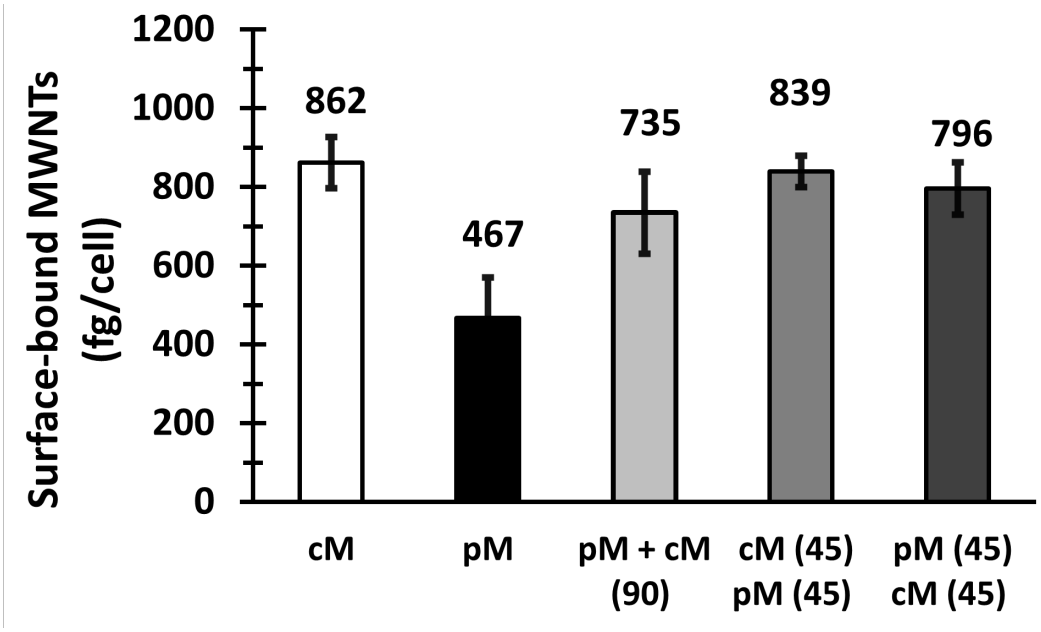

Figure 3.4. Test for additive binding of BSA-cMWNTs and BSA-pMWNTs to cells. Equivalent numbers of RAW 264.7 cells were seeded in 6-well plates and incubated at 37 °C under standard cell culture conditions for 24 h prior to the experiment in preparation for the additive binding studies as described in Methods. Cells were exposed to serum- and sodium bicarbonate-free media containing either 100 µg/mL BSA-pMWNTs or BSA-cMWNTs (labelled pM and cM in the graph) followed by incubation at 4 °C for 90 min to establish the amount of each bound when separate. Additive binding was tested by exposing the cells simultaneously to both BSA-cMWNTs and BSA-pMWNTs for 90 min. In a slightly different experimental design, the cells incubated with either BSA-cMWNTs or BSA-pMWNTs at 4 °C for 45 min, washed, and incubated with BSA-pMWNTs or BSA-cMWNTs, respectively, at 4 °C for 45 min for a total incubation time of 90 minutes. Surface-bound MWNTs were extracted and quantified using the SDS-PAGE method. The numbers above the bars are the mean femtograms of MWNTs/cell, and each data point is the mean of ≥3 independent experiments ± SD.

3.4.4. An SR-A Antagonist Reduces Binding of BSA-MWNTs to RAW 264.7 Cells

SR-As are involved in the binding of anionic ligands and certain modified proteins, such as oxidized LDL and maleylated albumin [30–33]. Moreover, the interaction of BSA with several nanoparticles causes conformation changes in BSA that expose cryptic SR-A1 binding sites [34–36]. In addition, there is indirect evidence that SRs bind carbon nanotubes [20]. Work from our lab also provided evidence that PF108-cMWNTs, but not PF108-pMWNTs, interact with SR-A1

[12][21]. Thus, SR-A1 is a potential receptor for BSA-MWNTs. This was initially explored by determining whether dextran sulfate, a known antagonist of SR-As, interferes with the binding of BSA-coated MWNTs. Chondroitin sulfate, an anionic polysaccharide that is not a SR-A1 inhibitor, was used as the control. RAW 264.7 cells were exposed to 100 μg/mL of BSA-MWNTs in serum- and sodium bicarbonate-free medium at 4 °C in the presence or absence of dextran sulfate or chondroitin sulfate, as indicated in Figure 3.5. The amount of BSA-cMWNTs bound to the cells declined as a function of dextran sulfate concentration and leveled off to about 50% compared to cells not exposed to the antagonist, whereas the amount of BSA-pMWNTs bound appeared to monotonically decline to a final level of ~25% of the control at the highest dextran sulfate concentration. These data again emphasize the differences in the receptor binding properties of the two BSA-MWNT types and further suggest that binding of both MWNTs types to receptors are sensitive to an SR-A1 antagonist; however, interpreting the data is not straightforward because the inhibition was partial, especially for BSA-cMWNTs. Therefore, studies were performed with cells that over- or under-express SR-A1 to clarify whether SR-A1 might interact with BSA-cMWNTs or BSA-pMWNTs, or both.

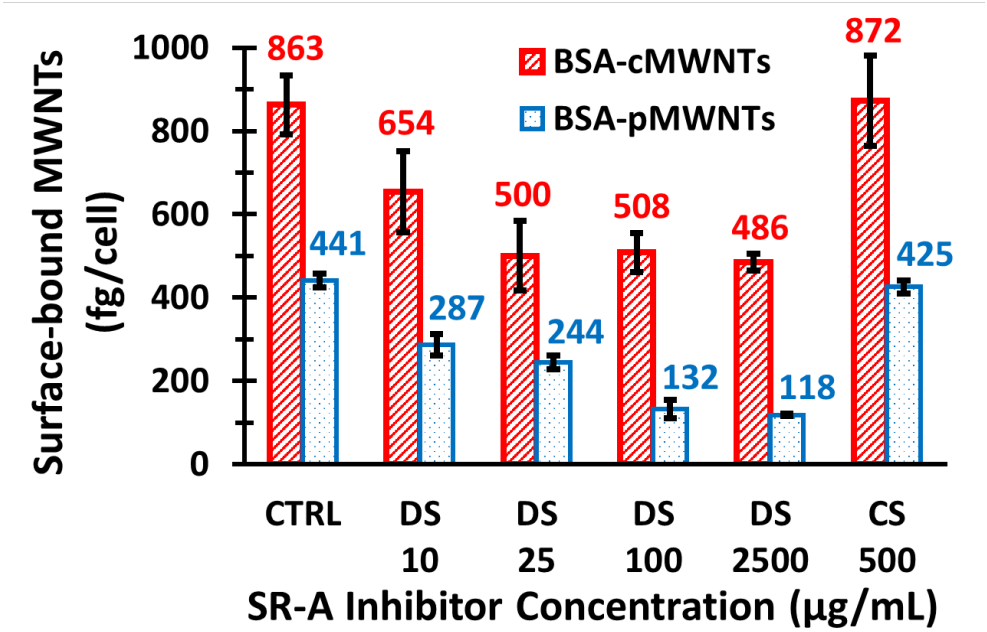

Figure 3.5. Effect of dextran sulfate on BSA-MWNT binding to RAW 264.7 cells at 4 °C. MWNTs suspended in a 0.10 mg/mL BSA working solution were mixed with an equal volume of 2X-concentrated, serum- and sodium bicarbonate-free medium to give a MWNT concentration of 100 µg/mL followed by the addition of chondroitin sulfate (CS) or the SR-A1 antagonist dextran sulfate (DS) at various concentrations as described in the Methods. The serum- and sodium bicarbonate-free medium control contained the same 100 µg/mL BSA-MWNTs, but without CS or DS. After initial plating and attachment to the substrate, cells were pre-incubated with serum-free medium (in the absence of MWNTs) for 2 h at 37 °C to deplete the serum in the cells. The cells were then pre-chilled to 4 °C and incubated at 4 °C for 1 h in serum- and sodium bicarbonate-free test medium that contained either a 0.10 mg/mL BSA working solution without MWNTs, with BSA-pMWNTs ± DS or CS (blue bars and line), or with BSA-cMWNTs ± DS or CS (red bars and line). Surface-bound MWNTs were extracted and quantified using the SDS-PAGE method. The numbers above the bars are the mean femtograms of MWNTs/cell. Data are the mean of ≥3 independent experiments ± SD.

3.4.5. Evidence that SR-A1 Mediates the Uptake of both BSA-cMWNTs and BSA-pMWNTs in CHO Cells Overexpressing SR-A1

CHO cells stably transfected with mouse SR-A1 cDNA (CHO[mSR-AI] cells) [24] were studied to determine whether the expression of SR-A1 in a cell line that does not normally express the receptor results in the accumulation of BSA-coated MWNTs by the cells. CHO[mSR-AI] cells overexpressing SR-A1 were incubated at 37 °C for 24 h with 100 µg/mL of BSA-pMWNTs or

cMWNT dispersions. Similarly treated wild-type CHO-K1 cells were the control. The results showed that the SR-A1 overexpressing CHO-K1 cells accumulated BSA-pMWNTs and BSA-cMWNTs two and three times more, respectively, compared to the control cells (Figure 3.6). This evidence supports the idea that SR-A1 is a receptor for both BSA-cMWNTs and BSA-pMWNTs, and also recapitulates the observation in Figure 3.2 that BSA-cMWNTs were accumulated to a greater extent than BSA-pMWNTs.

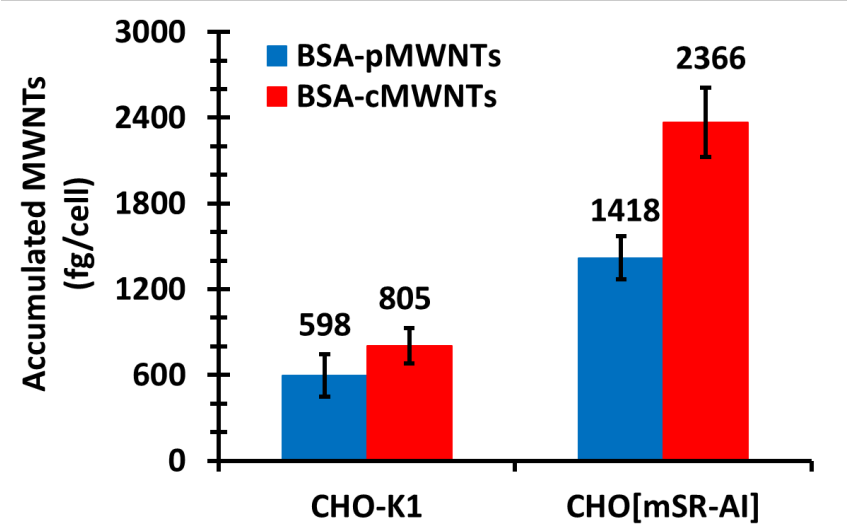

Figure 3.6. Accumulation of BSA-MWNTs by wild-type Chinese hamster ovary (WT CHO)-K1 control cells and Chinese hamster ovary (CHO) cells that overexpress SR-A1 receptors (CHO[mSR-AI] cells) at 37 °C. Equivalent numbers of each cell line were seeded in 6-well plates and incubated at 37 °C under standard cell culture conditions for 24 h prior to the experiment. The cells were then incubated at 37 °C for 24 h in medium that contained BSA-pMWNTs (blue bars) or BSA-cMWNTs (red bars) each at 100 µg/mL. After incubation, MWNTs were extracted from the cells and quantified by the SDS-PAGE method. The numbers above the data points are the mean femtograms of MWNTs/cell, and each data point is the mean of ≥3 experiments ± SD.

3.4.6. SR-A1 Knockout RAW 264.7 Cells Bind and Accumulate Far Less BSA-MWNTs Than WT Cells

Another approach to understanding the role that SR-A1 has in the uptake and binding of BSA-MWNTs is to knock out the SR-A1 gene using CRISPR-Cas9 technology. A RAW 264.7 cell knockout pool was obtained that contained a high proportion of cells with a mutation in the SR-A1 gene at a site near the beginning of the DNA sequence. This ensured that both SR-A1 as well as SR-A1.1 protein expression would be affected. A dilution cloning strategy was used to obtain 10 cell clones that did not express SR-A1 receptors on their surface as validated by immunofluorescence microscopy and flow cytometry. Both techniques showed that WT RAW 264.7 cells had high expression of SR-A1 receptors, whereas two knockout clones selected for study (termed C4 and B11) had negligible surface receptors (Figure 3.7).

To assess the recognition of BSA-pMWNTs and BSA-cMWNTs by SR-A1 receptors, the accumulation of 100 μg/mL BSA-coated pMWNTs or cMWNTs was measured using knockout clones C4 and B11 with the corresponding WT RAW 264.7 cells for comparison. The cells were incubated at 37 °C for 24 h with 100 μg/mL BSA-MWNTs and the accumulated MWNTs were measured using SDS-PAGE. As shown in Figure 3.8, the amount of accumulated MWNTs in the knockout SR-A1 cell lines was significantly decreased for both BSA-pMWNTs and BSA-cMWNTs compared to the WT RAW 264.7 cells.

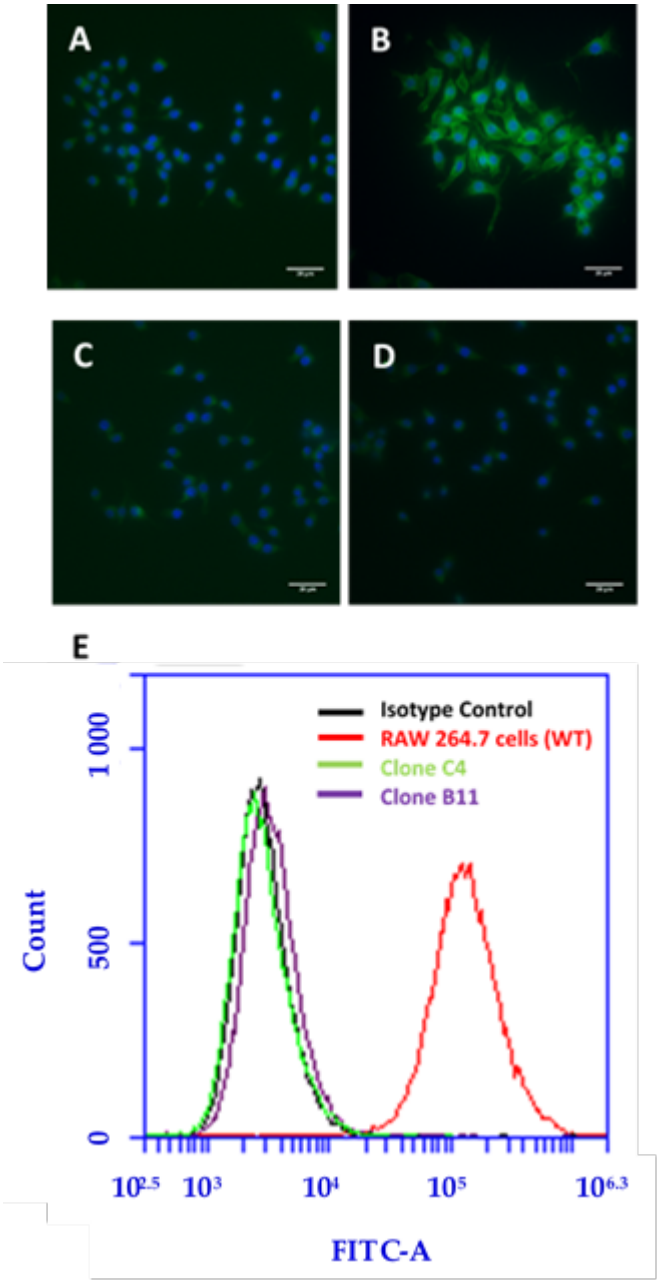

Figure 3.7. Immunofluorescence microscopy and flow cytometric analysis of WT and SR-A1 knockout RAW 264.7 cells. Immunofluorescence images of **(A)** control WT RAW 264.7 cells without mouse anti-SR-AI/MSR Alexa Fluor® 488-conjugated antibody, **(B)** WT RAW 264.7 cells incubated with mouse anti SR-AI/MSR Alexa Fluor® 488-conjugated antibody, and **(C, D)** two different clones (C4 and B11) of SR-A1 knockout RAW 264.7 cells incubated with anti-mouse SR-AI/MSR Alexa Fluor® 488-conjugated antibody. Hoechst 33342 staining is shown in blue and Alexa Fluor® 488 staining is shown in green. All images are normalized to the same intensity scale, and the scale bars represent 20 µm. **(E)** Flow cytometry analyses where the black line represents WT RAW 264.7 cells incubated with the rat IgG2B Alexa Fluor® 488-conjugated

monoclonal antibody as the isotype control, the red line represents WT RAW 264.7 cells incubated with mouse anti-SR-AI/MSR Alexa Fluor® 488-conjugated antibody, and the green and purple lines represent two different clones (C4 and B11, respectively) of SR-A1 knockout RAW 264.7 cells incubated with mouse anti-SR-AI/MSR Alexa Fluor® 488-conjugated antibody. The x-axis denotes fluorescence detected in the 518–548 nm spectral region, and the y-axis denotes the number of events for each analysis.

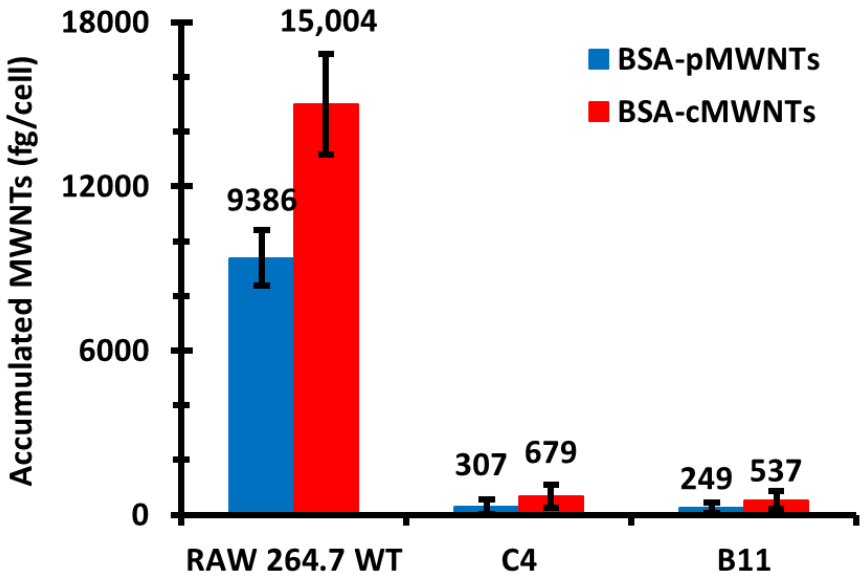

Figure 3.8. Accumulation of BSA-MWNTs by WT and SR-A1 knockout RAW 264.7 cells at 37 °C. MWNTs suspended in a 0.10 mg/mL BSA working solution were mixed with an equal volume of 2X-concentrated medium to produce MWNT concentrations of 100 µg/mL. Equivalent numbers of WT and SR-A1 knockout RAW 264.7 cells were seeded in 6-well plates and incubated at 37 °C under standard cell culture conditions for 24 h prior to the experiment. The cells were then incubated at 37 °C for 24 h in medium that contained BSA-pMWNTs (blue bars) or BSA-cMWNTs (red bars). After incubation, MWNTs were extracted from cells and quantified by the SDS-PAGE method. The numbers above the data points are the mean femtograms of MWNTs/cell. Data are the mean of ≥3 experiments ± SD.

The binding of 100 µg/mL BSA-coated cMWNTs and pMWNTs by RAW 264.7 cells was also studied using the same knockout SR-A1 clones (C4 and B11) and corresponding WT RAW 264.7 cells at 4 °C in the absence of serum, conditions under which MWNT binding by macrophages can be directly measured where the influence of protein coronas and cell uptake are controlled. The results indicated that there is a significant decrease in binding of BSA-pMWNTs

and BSA-cMWNTs by SR-A1 knockout RAW 264.7 cells compared to WT RAW 264.7 cells (Figure 3.9). Interestingly, 20% of the surface-bound BSA-cMWNTs were still present on the SR-A1 knockout cells, suggesting that a low binding capacity for BSA-cMWNTs still remained. Taken together, the observation that CHO cells expressing SR-A1 do bind BSA-MWNTs and the finding that RAW 264.7 cells lacking SR-A1 have greatly reduced binding, suggest that SR-A1 has a dominant role in the binding and accumulation of both BSA-MWNTs types.

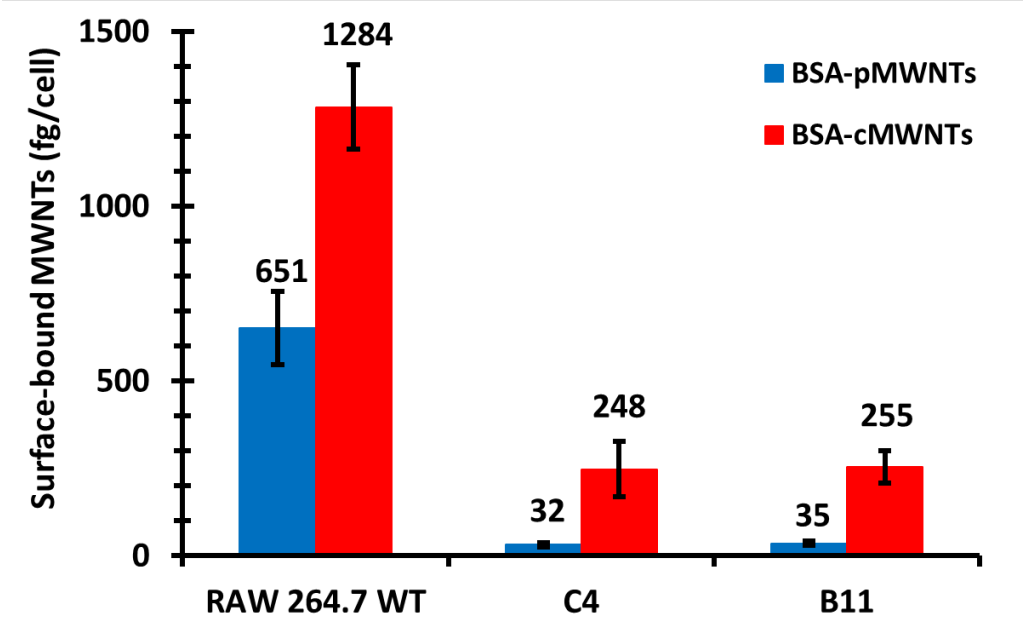

Figure 3.9. Surface binding of BSA-MWNTs by WT and SR-A1 knockout RAW 264.7 cells at 4 °C. MWNTs suspended in a 0.10 mg/mL BSA working solution were mixed with an equal volume of 2X-concentrated serum- and sodium bicarbonate-free medium to produce MWNT concentrations of 100 µg/mL. Equivalent numbers of WT and SR-A1 knockout RAW 264.7 cells were seeded in 6-well plates and incubated at 37 °C under standard cell culture conditions for 24 h prior to the experiment. Next, the cells were pre-incubated with serum-free medium (in the absence of BSA-MWNTs) for 2 h at 37 °C to deplete the serum in the cells. The cells were then pre-chilled to 4 °C and incubated at 4 °C for 1 h in serum- and sodium bicarbonate-free medium that contained either BSA-pMWNTs (blue bars) or BSA-cMWNTs (red bars). After incubation, surface-bound MWNTs were extracted and quantified by the SDS-PAGE method. Numbers above the data points are the mean femtograms of MWNTs/cell. Data are the mean of ≥3 independent experiments ± SD.

3.5. DISCUSSION

WT RAW 264.7 cells accumulated both BSA-cMWNTs and BSA-pMWNTs as a function of concentration after a 24 h exposure at 37 °C, although BSA-coated cMWNTs were accumulated to almost twice the amount of pMWNTs at each concentration tested. Uptake for both was near linear up to 100 μg/mL, after which the rate of accumulation was reduced. The break in the uptake curve at 100 μg/mL suggests a saturable receptor could be involved in the uptake process; however, accumulation depends not only on uptake, but also on potential loss of the MWNTs from cells by either recycling or degradation, or a loss of surface receptors that are internalized from the cell surface but not replaced. To focus on the initial interaction of MWNTs with cells, binding experiments were performed at 4 °C where internalization is inhibited. Moreover, serum proteins other than BSA that might confound the interpretation of the results were absent from the binding medium. Under these conditions, the binding of BSA-coated cMWNTs or pMWNTs to RAW 264.7 cells was near linear up to 100 μg/mL and then began to plateau, suggesting a saturable receptor-mediated binding event. There were two notable observations in comparing the binding of BSA-coated MWNTs to that we previously described for PF108-coated MWNTs. First, BSA-pMWNTs bound to cells, whereas previous studies showed that PF108-coated pMWNTs did not [12,21]. This indicates that the BSA corona confers the ability of pMWNTs to bind cells. Second, the cells bound more BSA-cMWNTs than BSA-pMWNTs, evidence that there remains a difference in binding capacity between the two MWNT types. Differences between BSA-cMWNTs and BSA-pMWNTs were also seen in their kinetics of dissociation from cells: BSA-pMWNTs dissociated very slowly, whereas BSA-cMWNTs had a faster dissociating component followed by a slowly dissociating component.

One model to explain the difference in the binding of BSA-cMWNTs and BSA-pMWNTs to cells is that there are two independent receptors - one for each type of MWNT. If there are two receptors interacting independently with two ligands, then exposing cells simultaneously to both ligands should result in an amount bound that is the sum of both when added separately. However, this was not observed. The amount bound after simultaneous exposure to both BSA-cMWNTs and BSA-pMWNTs never exceed the amount bound to cells when BSA-cMWNTs were added alone, which is not a simple additive result. To further explore this issue, sequential binding experiments were undertaken. The level of cell-associated MWNTs when BSA-cMWNTs were added first, followed by BSA-pMWNTs, was equal to the amount of MWNTs bound when BSA-cMWNTs were added alone, which is not additive. However, when the order was reversed and BSA-pMWNTs were added first followed by BSA-cMWNTs, there was more binding than observed when BSA-pMWNTs were added alone, and the amount was again equal to the increased binding seen with BSA-cMWNTs alone, an additive result. Altogether, the results of the binding experiments suggest a semi-additive model: BSA-cMWNTs can occupy all the binding sites available to BSA-pMWNTs, plus additional sites not available to BSA-pMWNTs. Thus, when BSA-cMWNTs are added first, no binding of BSA-pMWNTs occurs because the sites are occupied by BSA-cMWNTs. However, when BSA-pMWNTs are added first, there remain sites available for BSA-cMWNTs to which BSA-pMWNTs cannot bind.

The semi-additive data are compatible with a two-receptor model and also with a model where a single receptor has two binding sites. In the two-receptor model, one receptor would bind both cMWNTs and pMWNTs, and the other receptor would bind only cMWNTs. To help address the question of whether one or two receptors were involved in binding cMWNTs and pMWNTs,

the accumulation and binding of BSA-coated MWNTs was studied with RAW 264.7 cells in which the SR-A1 gene had been knocked out. Two clones isolated from the knockout pool, which were shown to lack immunologically detectable SR-A1 on their surfaces, failed to accumulate either BSA-coated cMWNTs or pMWNTs at 37 ℃. In binding studies at 4 ℃, the binding of BSA-pMWNTs was negligible and the binding of BSA-cMWNTs was reduced by 80%. It is not clear what is responsible for the 20% of BSA-cMWNT binding in the knockout cells, but perhaps one or more minor receptors for BSA-cMWNTs are present at low levels, and their contributions are seen in SR-A1 knockout cells. Nevertheless, it appears that knocking out SR-A1 severely affects the accumulation and binding of both BSA-cMWNTs and BSA-pMWNTs.

The simplest explanation for the knockout results is that SR-A1 is a receptor for both BSA-cMWNTs and BSA-pMWNTs. However, an alternative explanation is that knocking out SR-A1 suppresses the expression of one or more other cell surface proteins that could be major receptors for BSA-coated MWNTs. Two lines of evidence argue against this possibility. One is that dextran sulfate, a known antagonist of ligand binding to SR-A1, at least partially inhibited the binding of both BSA-coated pMWNTs and cMWNTs to cells, supporting the idea that SR-A1 is a receptor for these ligands. Second, CHO-K1 cells that ectopically express SR-A1 accumulated significantly more BSA-coated cMWNTs and pMWNTs than normal CHO-K1 cells. It seems unlikely that a covert receptor is activated in CHO cells, a cell type very different than RAW 264.7 macrophages, upon expression of SR-A1. Altogether, the simplest interpretation of the evidence argues that SR-A1 binds both BSA-cMWNTs and BSA-pMWNTs.

Understanding what features of BSA-coated MWNTs interact with SR-A1 is an interesting challenge. Previous work established that PF108-coated cMWNTs bound to and were

accumulated by macrophages that expressed SR-A1 in the absence of serum or serum proteins [12], whereas alveolar macrophages derived from mice knocked out for SR-A1 failed to accumulate the MWNTs [21]. PF108-coated pMWNTs were not bound or accumulated by either SR-A1 positive or negative macrophages [12,21]. Thus, no protein corona was necessary for SR-A1 to interact with cMWNTs. This suggested that one or more oxidized functionalities intrinsic to cMWNTs (carboxyl, hydroxyl, phenolic, etc.) are structural features potentially recognized by SR-A1. SR-A1 access to cMWNT surface features might occur at nanotube ends where the high curvature may not support coat binding and where oxidized functionalities are often located due to ring strain [37–40]. In addition, the residence time of BSA on MWNTs appears to be short and not all the surface is covered with protein at one time [41]. Thus, it is likely that SR-A1 would have access to oxidized groups intrinsic to the MWNT surface of BSA-coated cMWNTs.

It is understood now that while native BSA does not interact with SR-A1, conformational changes in BSA upon binding several types of nanoparticles uncover latent sites that do bind SR-A1 [34–36]. Moreover, BSA undergoes significant conformation changes upon binding to cMWNTs [42]. This leads to Binding Hypothesis 1 in Figure 3.10A, where BSA-coated cMWNTs present two sites that can interact with SR-A1 - one for oxidized groups inherent to the nanotube and another for the coat of conformationally altered BSA protein. This model may explain why more BSA-cMWNTs bind cells than BSA-pMWNTs, and also is consistent with the semi-additive binding data: all binding sites are occupied by BSA-cMWNTs, whereas only the BSA binding sites are occupied by BSA-pMWNTs. The model is also consistent with the differences in dissociation of the two MWNT types from cells assuming BSA-cMWNTs and BSA-pMWNTs

bound to SR-A1 at BSA binding sites dissociate slowly and that BSA-cMWNTs bound to oxidized functionalities dissociate more rapidly.

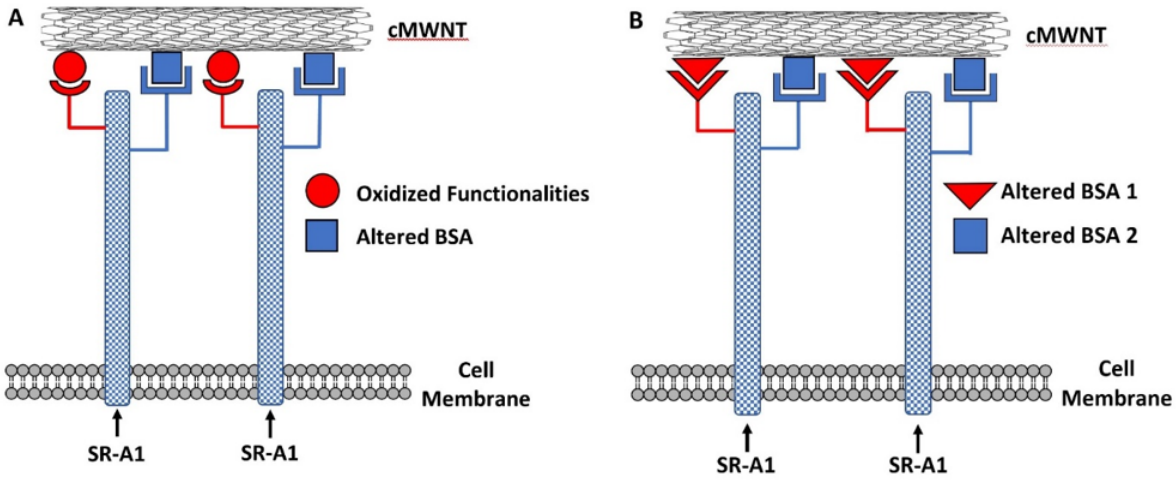

Figure 3.10. Models for the binding of cMWNTs to SR-A1. **(A)** Model where one site on SR-A1 interacts with altered binding sites on a BSA conformer and another site interacts with oxidized functionalities on cMWNTs. **(B)** Model where one site on SR-A1 interacts with altered binding sites on BSA Conformer 1 and another site interacts with altered binding sites on BSA Conformer 2.

An alternative model is one in which all the oxidized binding sites on cMWNTs are unavailable because they are covered by BSA, and that binding of BSA to cMWNTs exposes additional latent SR-A1 binding sites that are not exposed when BSA binds to pMWNTs; hence, cells bind more BSA-cMWNTs than BSA-pMWNTs. A model of this type shown in Figure 3.10B cannot be ruled out with the available data.

SR-A1 is a homotrimer and each monomer comprises an N-terminal cytoplasmic tail, a transmembrane domain, a spacer region, an α-helical coiled coil domain, a collagenous domain, and a C-terminal scavenger receptor cysteine rich (SRCR) domain [15,30,43]. Depending on the ligand, either the collagenous domain, the SRCR, or both, may be involved in ligand binding of various scavenger receptors, but the details are not well understood and appear to depend on the

structural context within each receptor type. For example, there is evidence from mutational studies with SR-A1 that positively charged residues in the collagenous domain are important for binding oxidized LDL [31,44]. Further, SR-A1.1, an alternatively spliced variant of SR-A1 lacking the SRCR domain, still binds oxidized LDL, suggesting that the collagenous domain is the major binding site for this ligand, although this does not rule out that the SRCR domain of SR-A1 may also interact with oxidized LDL or other protein ligands. Indeed, recent work suggests that the SR-A1 SRCR domain binds spectrin [45] and ferritin [46]. The SRCR domain is involved in the ligand binding by MARCO, a member of the class A scavenger receptors that shares the highly conserved SRCR domain with SR-A1 [47–49]. The functional unit of many scavenger receptor family members is a trimer, including SR-A1, and the potential for three ligand binding sites per trimer is believed to enhance binding avidity to larger ligands, such as intact bacteria, and which would presumably include large ENPs such as MWNTs [33]. This feature is not explicitly shown in the models of Figure 3.10, but could be accommodated. Nevertheless, given the intricacies of how different domains in scavenger receptors interact with ligands, it is difficult to parse which SR-A1 domains interact with what features of BSA-coated MWNTs.

Additional complexities in scavenger receptor interaction with ligands arise from evidence that scavenger receptors, including SR-A1, may form complexes with other pattern recognition receptors, termed co-receptors, that also interact with the same ligand. The resulting complexes can then recruit components to form “Signalosomes” that contain two or more receptors bound to the same ligand plus associated signaling components that may activate cell signaling pathways [32,33,50]. For example, there is evidence from computational work [51] and from molecular docking studies that SWNTs may bind toll-like receptor 4 (TLR4) [52]. It would be interesting to

know whether the ~20% of cMWNT binding to RAW 264.7 cells lacking SR-A1 seen in Figure 3.9 is due to TLR4. Thus, the simple models in Figure 3.10 may not capture the range of possibilities for how MWNTs interact with SR-A1 and other cell components via co-receptors. Nevertheless, SR-A1 is a key player evidenced by the major loss of binding in SR-A1 knockout cells and the gain of binding in CHO cells that ectopically express SR-A1.

3.6. CONCLUSIONS

From previous work, PF108-coated pMWNTs fail to bind to macrophages but BSA-coated pMWNTs do bind, suggesting that a BSA corona confers the ability of pMWNTs to bind to cells. Therefore, in this article we studied the interaction of BSA-MWNTs with macrophages using a direct binding assay under highly controlled conditions where the influence of nanotube functionalization and protein coronas could be controlled. The results demonstrated that the binding of both BSA-cMWNTs and BSA-pMWNTs to the cell surface was a dose-dependent and saturable function of the applied MWNT concentration. Both MWNT types bound and were accumulated by RAW 264.7 cells; however, the cells bound and accumulated two times more BSA-cMWNTs than BSA-pMWNTs, suggesting that there are more binding sites on the cell surface for BSA-cMWNTs than BSA-pMWNTs. The binding of BSA-coated cMWNTs and pMWNTs to RAW 264.7 cells was semi-additive, suggesting that a single receptor with two distinct binding sites could explain the data. SR-A1 knockout RAW 264.7 cells had significantly reduced binding and accumulation of both BSA-pMWNTs and cMWNTs and CHO cells that ectopically expressed SR-A1 accumulated both MWNT types, whereas WT CHO cells did not, suggesting that SR-A1 is the key receptor for both MWNT types. Models consistent with the data are proposed where SR-A1 has two binding sites that interact with BSA-coated MWNTs

differently depending on the presence of a BSA corona and on the presence or absence of oxidized groups on the MWNTs. The approaches and observations in this study may contribute to the rational design of nanotoxicity remediation efforts and biomedical applications of engineered carbon nanoparticles.

3.7. REFERENCES

1. Walczyk, D.; Bombelli, F.B.; Monopoli, M.P.; Lynch, I.; Dawson, K.A. What the Cell "Sees" in Bionanoscience. *J. Am. Chem. Soc.* **2010**, *132*, 5761–5768.

2. Monopoli, M.P.; Walczyk, D.; Campbell, A.; Elia, G.; Lynch, I.; Baldelli Bombelli, F.; Dawson, K.A. Physical−Chemical Aspects of Protein Corona: Relevance to in Vitro and in Vivo Biological Impacts of Nanoparticles. *J. Am. Chem. Soc.* **2011**, *133*, 2525–2534.

3. Westmeier, D.; Stauber, R.H.; Docter, D. The concept of bio-corona in modulating the toxicity of engineered nanomaterials (ENM). *Toxicol. Appl. Pharmacol.* **2016**, *299*, 53–57.

4. Alberg, I.; Kramer, S.; Schinnerer, M.; Hu, Q.; Seidl, C.; Leps, C.; Drude, N.; Möckel, D.; Rijcken, C.; Lammers, T., et al. Polymeric Nanoparticles with Neglectable Protein Corona. *Small* **2020**, *16*, 1907574 (13 pp).

5. Schnorr, J.M.; Swager, T.M. Emerging Applications of Carbon Nanotubes†. *Chem. Mater.* **2011**, *23*, 646–657.

6. De Volder, M.F.L.; Tawfick, S.H.; Baughman, R.H.; Hart, A.J. Carbon Nanotubes: Present and Future Commercial Applications. *Science* **2013**, *339*, 535–539.

7. Sehrawat, P.; Julien, C.; Islam, S.S. Carbon nanotubes in Li-ion batteries: A review. *Mater. Sci. Eng., B* **2016**, *213*, 12–40.

8. Rao, R.; Pint, C.L.; Islam, A.E.; Weatherup, R.S.; Hofmann, S.; Meshot, E.R.; Wu, F.; Zhou, C.; Dee, N.; Amama, P.B., et al. Carbon Nanotubes and Related Nanomaterials: Critical Advances and Challenges for Synthesis toward Mainstream Commercial Applications. *ACS Nano* **2018**, *12*, 11756–11784.

9. Petersen, E.J.; Zhang, L.; Mattison, N.T.; O'Carroll, D.M.; Whelton, A.J.; Uddin, N.; Nguyen, T.; Huang, Q.; Henry, T.B.; Holbrook, R.D., et al. Potential release pathways, environmental fate, and ecological risks of carbon nanotubes. *Environ. Sci. Technol.* **2011**, *45*, 9837–9856.

10. Sweeney, S.; Grandolfo, D.; Ruenraroengsak, P.; Tetley, T.D. Functional consequences for primary human alveolar macrophages following treatment with long, but not short, multiwalled carbon nanotubes. *Int J Nanomedicine* **2015**, *10*, 3115–3129.

11. Allegri, M.; Perivoliotis, D.K.; Bianchi, M.G.; Chiu, M.; Pagliaro, A.; Koklioti, M.A.; Trompeta, A.-F.A.; Bergamaschi, E.; Bussolati, O.; Charitidis, C.A. Toxicity determinants of multi-walled carbon nanotubes: The relationship between functionalization and agglomeration. *Toxicol. Rep.* **2016**, *3*, 230–243.

12. Wang, R.; Lee, M.; Kinghorn, K.; Hughes, T.; Chuckaree, I.; Lohray, R.; Chow, E.; Pantano, P.; Draper, R. Quantitation of cell-associated carbon nanotubes: Selective binding and accumulation of carboxylated carbon nanotubes by macrophages. *Nanotoxicology* **2018**, *12*, 677–690.

13. Brown, M.S.; Goldstein, J.L. Lipoprotein Metabolism in the Macrophage: Implications for Cholesterol Deposition in Atherosclerosis. *Annu. Rev. Biochem.* **1983**, *52*, 223–261.

14. Kingsley, D.M.; Krieger, M. Receptor-mediated endocytosis of low density lipoprotein: Somatic cell mutants define multiple genes required for expression of surface-receptor activity. *Proc. Natl. Acad. Sci. USA* **1984**, *81*, 5454–5458.

15. PrabhuDas, M.R.; Baldwin, C.L.; Bollyky, P.L.; Bowdish, D.M.E.; Drickamer, K.; Febbraio, M.; Herz, J.; Kobzik, L.; Krieger, M.; Loike, J., et al. A Consensus Definitive Classification of Scavenger Receptors and Their Roles in Health and Disease. *J. Immunol.* **2017**, *198*, 3775–3789.

16. Dutta, D.; Sundaram, S.K.; Teeguarden, J.G.; Riley, B.J.; Fifield, L.S.; Jacobs, J.M.; Addleman, S.R.; Kaysen, G.A.; Moudgil, B.M.; Weber, T.J. Adsorbed proteins influence the biological activity and molecular targeting of nanomaterials. *Toxicol. Sci.* **2007**, *100*, 303–315.

17. Singh, R.P.; Das, M.; Thakare, V.; Jain, S. Functionalization density dependent toxicity of oxidized multiwalled carbon nanotubes in a murine macrophage cell line. *Chem. Res. Toxicol.* **2012**, *25*, 2127–2137.

18. Wang, X.; Guo, J.; Chen, T.; Nie, H.; Wang, H.; Zang, J.; Cui, X.; Jia, G. Multi-walled carbon nanotubes induce apoptosis via mitochondrial pathway and scavenger receptor. *Toxicol. In Vitro* **2012**, *26*, 799–806.

19. Gao, N.; Zhang, Q.; Mu, Q.; Bai, Y.; Li, L.; Zhou, H.; Butch, E.R.; Powell, T.B.; Snyder, S.E.; Jiang, G., et al. Steering carbon nanotubes to scavenger receptor recognition by nanotube surface chemistry modification partially alleviates NFκB activation and reduces its immunotoxicity. *ACS Nano* **2011**, *5*, 4581–4591.

20. Hirano, S.; Fujitani, Y.; Furuyama, A.; Kanno, S. Macrophage receptor with collagenous structure (MARCO) is a dynamic adhesive molecule that enhances uptake of carbon nanotubes by CHO-K1 Cells. *Toxicol. Appl. Pharmacol.* **2012**, *259*, 96–103.

21. Wang, R.; Lohray, R.; Chow, E.; Gangupantula, P.; Smith, L.; Draper, R. Selective Uptake of Carboxylated Multi-Walled Carbon Nanotubes by Class A Type 1 Scavenger Receptors and Impaired Phagocytosis in Alveolar Macrophages. *Nanomaterials (Basel)* **2020**, *10*, 2417 (29 pp).

22. Braun, E.I.; Pantano, P. The importance of an extensive elemental analysis of single-walled carbon nanotube soot. *Carbon* **2014**, *77*, 912–919.

23. Huynh, M.T.; Veyan, J.F.; Pham, H.; Rahman, R.; Yousuf, S.; Brown, A.; Lin, J.; Balkus, Jr., K.J.; Diwakara, S.D.; Smaldone, R.A., et al. The Importance of Evaluating the Lot-to-Lot Batch Consistency of Commercial Multi-Walled Carbon Nanotube Products. *Nanomaterials (Basel)* **2020**, *10*, 1930 (27 pp).

24. Ashkenas, J.; Penman, M.; Vasile, E.; Acton, S.; Freeman, M.; Krieger, M. Structures and high and low affinity ligand binding properties of murine type I and type II macrophage scavenger receptors. *J. Lipid Res.* **1993**, *34*, 983–1000.

25. Wang, R.; Meredith, N.A.; Lee Jr., M.; Deutsch, D.; Miadzvedskaya, L.; Braun, E.; Pantano, P.; Harper, S.; Draper, R. Toxicity assessment and bioaccumulation in zebrafish embryos exposed to carbon nanotubes suspended in Pluronic® F-108. *Nanotoxicology* **2016**, *10*, 689–698.

26. Nakata, T. Destruction of challenged endotoxin in a dry heat oven. *PDA J. Pharm. Sci. Technol.* **1994**, *48*, 59–63.

27. Wang, R.; Hughes, T.; Beck, S.; Vakil, S.; Li, S.; Pantano, P.; Draper, R.K. Generation of toxic degradation products by sonication of Pluronic® dispersants: Implications for nanotoxicity testing. *Nanotoxicology* **2013**, *7*, 1272–1281.

28. Wang, R.; Mikoryak, C.; Li, S.; Bushdiecker 2nd, D.; Musselman, I.H.; Pantano, P.; Draper, R.K. Cytotoxicity screening of single-walled carbon nanotubes: Detection and removal of cytotoxic contaminants from carboxylated carbon nanotubes. *Mol. Pharm.* **2011**, *8*, 1351–1361.

29. Wang, R.; Mikoryak, C.; Chen, E.; Li, S.; Pantano, P.; Draper, R.K. Gel electrophoresis method to measure the concentration of single-walled carbon nanotubes extracted from biological tissue. *Anal. Chem.* **2009**, *81*, 2944–2952.

30. Krieger, M.; Herz, J. Structures and functions of multiligand lipoprotein receptors: Macrophage scavenger receptors and LDL receptor-related protein (LRP). *Annu. Rev. Biochem.* **1994**, *63*, 601–637.

31. Andersson, L.; Freeman, M.W. Functional Changes in Scavenger Receptor Binding Conformation Are Induced by Charge Mutants Spanning the Entire Collagen Domain. *J. Biol. Chem.* **1998**, *273*, 19592–19601.

32. Martínez, V.G.; Moestrup, S.K.; Holmskov, U.; Mollenhauer, J.; Lozano, F. The Conserved Scavenger Receptor Cysteine-Rich Superfamily in Therapy and Diagnosis. *Pharmacol. Rev.* **2011**, *63*, 967–1000.

33. Canton, J.; Neculai, D.; Grinstein, S. Scavenger receptors in homeostasis and immunity. *Nat. Rev. Immunol.* **2013**, *13*, 621–634.

34. Fleischer, C.C.; Payne, C.K. Nanoparticle–Cell Interactions: Molecular Structure of the Protein Corona and Cellular Outcomes. *Acc. Chem. Res.* **2014**, *47*, 2651–2659.

35. Fleischer, C.C.; Payne, C.K. Secondary Structure of Corona Proteins Determines the Cell Surface Receptors Used by Nanoparticles. *J. Phys. Chem. B* **2014**, *118*, 14017–14026.

36. Mortimer, G.M.; Butcher, N.J.; Musumeci, A.W.; Deng, Z.J.; Martin, D.J.; Minchin, R.F. Cryptic Epitopes of Albumin Determine Mononuclear Phagocyte System Clearance of Nanomaterials. *ACS Nano* **2014**, *8*, 3357–3366.

37. Wong, S.S.; Joselevich, E.; Woolley, A.T.; Cheung, C.L.; Lieber, C.M. Covalently functionalized nanotubes as nanometre-sized probes in chemistry and biology. *Nature* **1998**, *394*, 52–55.

38. Chen, J.; Hamon, M.A.; Hu, H.; Chen, Y.; Rao, A.M.; Eklund, P.C.; Haddon, R.C. Solution properties of single-walled carbon nanotubes. *Science* **1998**, *282*, 95–98.

39. Sun, Y.P.; Fu, K.; Lin, Y.; Huang, W. Functionalized carbon nanotubes: Properties and applications. *Acc. Chem. Res.* **2002**, *35*, 1096–1104.

40. Zhang, J.; Zou, H.; Qing, Q.; Yang, Y.; Li, Q.; Liu, Z.; Guo, X.; Du, Z. Effect of chemical oxidation on the structure of single-walled carbon nanotubes. *J. Phys. Chem. B* **2003**, *107*, 3712–3718.

41. Frise, A.E.; Edri, E.; Furó, I.n.; Regev, O. Protein Dispersant Binding on Nanotubes Studied by NMR Self-Diffusion and Cryo-TEM Techniques. *J. Phys. Chem. Lett.* **2010**, *1*, 1414–1419.

42. Lou, K.; Zhu, Z.; Zhang, H.; Wang, Y.; Wang, X.; Cao, J. Comprehensive studies on the nature of interaction between carboxylated multi-walled carbon nanotubes and bovine serum albumin. *Chem.-Biol. Interact.* **2016**, *243*, 54–61.

43. Zani, I.; Stephen, S.; Mughal, N.; Russell, D.; Homer-Vanniasinkam, S.; Wheatcroft, S.; Ponnambalam, S. Scavenger receptor structure and function in health and disease. *Cells* **2015**, *4*, 178 (24 pp).

44. Doi, T.; Higashino, K.; Kurihara, Y.; Wada, Y.; Miyazaki, T.; Nakamura, H.; Uesugi, S.; Imanishi, T.; Kawabe, Y.; Itakura, H. Charged collagen structure mediates the recognition of negatively charged macromolecules by macrophage scavenger receptors. *J. Biol. Chem.* **1993**, *268*, 2126–2133.

45. Cheng, C.; Hu, Z.; Cao, L.; Peng, C.; He, Y. The scavenger receptor SCARA1 (CD204) recognizes dead cells through spectrin. *J. Biol. Chem.* **2019**, *294*, 18881–18897.

46. Yu, B.; Cheng, C.; Wu, Y.; Guo, L.; Kong, D.; Zhang, Z.; Wang, Y.; Zheng, E.; Liu, Y.; He, Y. Interactions of ferritin with scavenger receptor class A members. *J. Biol. Chem.* **2020**, *295*, 15727–15741.

47. Chen, Y.; Sankala, M.; Ojala, J.R.M.; Sun, Y.; Tuuttila, A.; Isenman, D.E.; Tryggvason, K.; Pikkarainen, T. A Phage Display Screen and Binding Studies with Acetylated Low Density Lipoprotein Provide Evidence for the Importance of the Scavenger Receptor Cysteine-rich (SRCR) Domain in the Ligand-binding Function of MARCO. *J. Biol. Chem.* **2006**, *281*, 12767–12775.

48. Whelan, F.J.; Meehan, C.J.; Golding, G.B.; McConkey, B.J.; E Bowdish, D.M. The evolution of the class A scavenger receptors. *BMC Evol. Biol.* **2012**, *12*, 227 (11 pp).

49. Ojala, J.R.M.; Pikkarainen, T.; Tuuttila, A.; Sandalova, T.; Tryggvason, K. Crystal Structure of the Cysteine-rich Domain of Scavenger Receptor MARCO Reveals the Presence of a Basic and an Acidic Cluster That Both Contribute to Ligand Recognition. *J. Biol. Chem.* **2007**, *282*, 16654–16666.

50. Heit, B.; Kim, H.; Cosío, G.; Castaño, D.; Collins, R.; Lowell, Clifford A.; Kain, Kevin C.; Trimble, William S.; Grinstein, S. Multimolecular Signaling Complexes Enable Syk-Mediated Signaling of CD36 Internalization. *Dev. Cell* **2013**, *24*, 372–383.

51. Turabekova, M.; Rasulev, B.; Theodore, M.; Jackman, J.; Leszczynska, D.; Leszczynski, J. Immunotoxicity of nanoparticles: A computational study suggests that CNTs and C60 fullerenes might be recognized as pathogens by Toll-like receptors. *Nanoscale* **2014**, *6*, 3488–3495.

52. Mukherjee, S.P.; Bondarenko, O.; Kohonen, P.; Andón, F.T.; Brzicová, T.; Gessner, I.; Mathur, S.; Bottini, M.; Calligari, P.; Stella, L., et al. Macrophage sensing of single-walled carbon nanotubes via Toll-like receptors. *Sci. Rep.* **2018**, *8*, 1115 (17 pp).

CHAPTER 4

CONCLUSIONS

Both the production and use of multi-walled carbon nanotubes (MWNTs) are rapidly increasing world-wide despite the possible adverse effects they may have on human health. Of particular concern are reports that MWNTs can cause pulmonary fibrosis that may lead to mesothelioma, similar to asbestos. Macrophages are a key intermediary in MWNT pathology and the molecular mechanisms of how MWNTs interact with macrophages to influence inflammatory responses have been widely studied; however, there remain significant knowledge gaps and conflicting literature, especially regarding the interaction of MWNTs with cells and receptors. Investigating the nature of MWNT receptors on macrophages with well-characterized MWNTs plays a critical role in studying the pathogenesis of MWNTs because of consistent reports that MWNTs can be toxic.

This dissertation presents important contributions towards the safe use of well-characterized MWNTs. Chapter 1 reviews MWNT synthetic methods, their unique physicochemical properties and commercial applications, root causes of their toxic behavior, and a novel method developed by our team to quantify the binding and accumulation of MWNTs by mammalian cells. Next, the interaction of macrophages with MWNTs is surveyed including the effect that a protein corona has on the binding and accumulation of MWNTs by cells, and a review of macrophage receptors implicated in the accumulation of MWNTs, in particular, class A-type 1 scavenger receptors (SR-A1s). This chapter concludes with a description of the CRISPR-Cas9

gene-editing technique, since it is believed that this is its first use in studying the binding of MWNTs with SR-A1s.

Chapter 2 presents a comprehensive physicochemical characterization of two commercial lots of pristine MWNTs (pMWNTs) and carboxylated MWNTs (cMWNTs) purchased in 2015 and 2018. The analyses revealed many similarities between the two cMWNT products and several key differences between the two pMWNT products. The pMWNTs purchased in 2018 displayed less oxidative stability, a higher defect density, and a smaller amount of surface oxygen species relative to the 2015-pMWNTs. Additionally, the concentration of pMWNTs that could be suspended by bovine serum albumin (BSA) with the 2018-pMWNTs was significantly lower relative to the 2015-pMWNTs. Most importantly, while the 24-h proliferation of RAW 264.7 macrophages cultured with BSA-suspensions of 2015-pMWNTs were statistically similar to the proliferation of cells observed with the two BSA-cMWNT suspensions, the 24-h proliferation of RAW 264.7 cells incubated with BSA-suspensions of 2018-pMWNTs was not. Specifically, the 24-h proliferation of cells incubated with BSA-suspensions of 2018-pMWNTs at 100 μg/mL was ~20% lower relative to BSA-suspensions of 2015-pMWNTs at 100 μg/mL, even though the amount of the 2018-pMWNTs accumulated by cells was ~16% less relative to the amount of 2015-pMWNTs accumulated by cells. In addition, whereas the 72-h proliferation of cells incubated with 125 μg/mL BSA suspensions of 2015-pMWNTs was reduced by ~33% relative to the control, the 72-h proliferation of cells incubated with BSA-coated 2018-pMWNTs at 125 μg/mL was reduced by ~70% relative to the control, corresponding to a 72-h half maximal inhibitory concentration (IC-50) of ~90 μg/mL for the 2018-pMWNTs. The results suggest that the 2018-pMWNTs was significantly more toxic than the 2015-pMWNTs. Thus, this chapter demonstrates

(i) the difficulty in assessing the role of a single physicochemical property of a MWNT product to an observed biological response, (ii) that subtle physicochemical differences can have a significant effect on the response of biological cells to a MWNT product, and (iii) that production-lot consistency must be considered when assessing the toxicity or biological activity of MWNTs and other carbon nanomaterials. It is believed that this work is the first to present comprehensive material characterization data for different production lots of MWNTs used subsequently in assessing the biological response of MWNTs to mammalian cells.

Chapter 3 focuses on the biological responses of macrophages to the high-quality pMWNT and cMWNT lots that were coated with BSA. Herein, Chinese hamster ovary (CHO) cells that ectopically express SR-A1 and RAW 264.7 cells that were deleted for SR-A1 expression by CRISPR-Cas9 technology were used to address the questions of whether these macrophages have MWNT receptors that might initiate or modulate signals involved in inflammation and to probe what cell surface receptors are involved in recognizing BSA-coated MWNTs. Under highly controlled conditions where the influence of nanotube functionalization and protein corona could be studied, the binding and accumulation of both BSA-pMWNTs and BSA-cMWNTs to wild-type RAW 264.7 cells was found to be a dose-dependent and saturable function of the MWNT concentration. Specifically, RAW 264.7 cells bound and accumulated two times more BSA-cMWNTs than BSA-pMWNTs, demonstrating that there are more binding sites on the RAW 264.7 cell surface for BSA-cMWNTs than BSA-pMWNTs, and suggesting that there were specific receptors that bind both BSA-coated pMWNTs and cMWNTs. This is interesting because previous work from our team showed that Pluronic® F-108 polymer-coated pMWNTs failed to bind to macrophages [1,2], whereas it was demonstrated here that BSA-coated pMWNTs do bind,

suggesting that pMWNTs coated with a BSA protein corona confers the capacity to bind to cells. SR-A1 knockout RAW 264.7 cells reduced significantly the binding and accumulation of both BSA-pMWNTs and cMWNTs and CHO cells that ectopically expressed SR-A1 accumulated both MWNT types, whereas wild-type CHO cells did not, suggesting that SR-A1 is the key receptor for both MWNT types. Furthermore, CHO cells that ectopically express SR-A1 accumulated 2-3 times more BSA-cMWNTs than BSA-pMWNTs, emphasizing the differences between how BSA-cMWNTs and BSA-pMWNTs interact with SR-A1. One model to explain these results is that SR-A1 can interact with two structural features of BSA-coated cMWNTs, one inherent to the oxidized nanotubes (such as carboxyl and other oxidized groups) and the other provided by the BSA corona, whereas SR-A1 only interacts with the BSA corona of BSA-pMWNTs that do not display significant oxidized functional groups. A better understanding of the mechanisms by which MWNTs interact with macrophages should lead to the rational design of nanotoxicity remediation efforts and biomedical applications of carbon nanomaterials.

REFERENCES

1. Wang, R.; Lee, M.; Kinghorn, K.; Hughes, T.; Chuckaree, I.; Lohray, R.; Chow, E.; Pantano, P.; Draper, R. Quantitation of cell-associated carbon nanotubes: selective binding and accumulation of carboxylated carbon nanotubes by macrophages. *Nanotoxicology* **2018**, *12*, 677-698.

2. Wang, R.; Lohray, R.; Chow, E.; Gangupantula, P.; Smith, L.; Draper, R. Selective Uptake of Carboxylated Multi-Walled Carbon Nanotubes by Class A Type 1 Scavenger Receptors and Impaired Phagocytosis in Alveolar Macrophages. *Nanomaterials* **2020**, *10*, 2417 (29 pp.).

BIOGRAPHICAL SKETCH

Mai T. Huynh was born in Vietnam. She immigrated to Dallas, Texas in 2011. She attended Richland Community College in 2012 and was awarded a STEM Scholarship for students who demonstrate excellence in STEM academics. Two consecutive honor summer research internship programs played a great foundation for her research interest in science, the first being a National Science Foundation - Research Experiences for Undergraduates Programs at Texas A&M University, and the second being a Howard Hughes Medical Institute Science Education Programs at the University of North Texas. In 2014, she discovered a new bacteriophage that infects *Streptomyces Griseus* with a never before published DNA sequence and it was named after her (MaiH). After completion of her Associates Degree from Richland College, she was accepted by The University of Texas at Dallas (UT Dallas) in Fall of 2014 as a Terry Foundation scholar, a program for students who demonstrate excellence in academics. She performed honor undergraduate research with Drs. Paul Pantano of the Chemistry Department and Homer Montgomery of the Geology Department. She graduated Summa Cum Laude and Major Honor with a Bachelor degree in Chemistry from UT Dallas in May 2016. Being interested in analytical chemistry and cell biology, she immediately joined the UT Dallas Bionanosciences group of Drs. Paul Pantano and Rockford Draper in 2016. She worked as a graduate research assistant under supervision of Drs. Paul Pantano and Rockford Draper during her time at UT Dallas. She was awarded a McDermott Graduate Fellowship – an award for outstanding students pursuing leadership roles in research enterprises in 2017 and a National Science Foundation Graduate Research Fellowship - an award for outstanding graduate students in STEM disciplines in 2018. She plans to continue her work in nanotoxicology and imaging technology as a postdoctoral fellow.

CURRICULUM VITAE

MAI T. HUYNH

Email: mai.t.huynh@utdallas.edu

EDUCATION

Ph.D. in Chemistry **Aug 2016 – 2021**
The University of Texas at Dallas, Richardson, Texas

Bachelor of Science in Chemistry **May 2016**
Summa Cum Laude and Major Honors
The University of Texas at Dallas, Richardson, Texas

Associate Degree in Science **May 2014**
Richland College, Dallas, Texas

HONORS AND AWARDS (The University of Texas at Dallas)

National Science Foundation - Graduate Research Fellowship Program **2018 – Present**
A 3-year award for outstanding graduate students in STEM disciplines.

Eugene McDermott Graduate Fellowship **2017 – Present**
A 4-year award for outstanding students pursuing leadership roles in research enterprises.

American Chemical Society – Chemistry Student of the Year **2016**
An award for the top senior undergraduate chemist in the department.

Terry Foundation Scholarship – Honors College **2014 – 2017**
An award for those who demonstrate excellence in academics and future leadership distinction.

Dean's List – School of Natural Sciences and Mathematics **2014 – 2016**
An award for students with a GPA that is among the top 10% of all students within the school.

Comet Transfer Scholarship **2014**
An award for transfer students whose GPA is among the top 10% of their class.

Phi Theta Kappa Scholarship **2014**
An award for transfer students whose GPA is among the top 10% of their class.

HONORS AND AWARDS (Richland College)

DCCCD STEM Scholarship **2012 – 2014**

A 3-year award for students who demonstrate excellence in STEM academics and who show promise of future leadership distinction.

Asian Pacific Islander American Scholarship **2014**

A scholarship for Asian students who demonstrate excellence in academics and leadership.

JD and Lillie Belle Hall Scholarship **2014**

A scholarship for students based on excellent academic and leadership performance.

President's Honor Roll – Richland College **2012 – 2014**

An award for students who maintain a 4.0 GPA.

PROFESSIONAL AFFILIATIONS

Member, Society of Toxicology **2017 – Present**

Member, American Chemical Society **2016 – Present**

Member, Phi Kappa Phi National Honor Society **2015 – Present**

Member, Golden Key International Honor Society **2015 – Present**

Member, Tau Sigma National Honor Society **2015 – Present**

Member, Phi Theta Kappa National Honor Society **2012 – Present**

Member, Richland College Honor Academy **2013 – 2014**

Member, Mu Alpha Theta National Mathematics Honor Society **2012 – 2014**

PUBLICATIONS

Huynh, M. T.; Mikoryak, C.; Pantano, P.; Draper, R. "*Scavenger Receptor A1 Mediates the Uptake of Carboxylated and Pristine Multi-Walled Carbon Nanotubes Coated with Bovine Serum Albumin*", Nanomaterials, 11 (2021) 539. Editor's Choice Distinction

PUBLICATIONS (continued)

Huynh, M. T.; Veyan, J. F.; Pham, H.; Rahman, R.; Yousuf, S.; Brown, A.; Lin, J.; Balkus, K. J.; Diwakara, S.; Smaldone, R.; Legrand, B.; Mikoryak, C.; Draper, R.; Pantano, P. *"The Importance of Evaluating the Lot-to-Lot Batch Consistency of Commercial Multi-Walled Carbon Nanotube Products"*, Nanomaterials, 10 (2020) 1930.

Donegan-Quick, R.; Gibbs, Z. A.; Amuka, P. O.; Bernal, J. T.; Boyd, D. A. M.; Burr, A. R.; Cohelho, R. E.; Dossou, A. S.; Henry, R. M.; **Huynh, M. T.**; Kanani-Hendijani, T. A.; Martinez, G.; McClendon-Moss, T. O.; Orozco, S.; San Martin, J. M.; Stoddart, K. E.; Stringer, M. M.; Villegas, R. L.; Nayek, S.; Suri, N.; Garlena, R. A.; Russel, D. A.; Hughes, L. E. "*Genome Sequences of Five Streptomyces Bacteriophages Forming Clustere BG",* Genome Announcements 28 (2017) 5.

Becker, A. L.; Montgomery, K.; **Huynh, M. T.**; Santistevan, I. "*Lightcurves of Asteroids 4271 Novosibirsk and 6335 Nicolerappaport"*, Minor Planet Bulletin 42 (2015) 107.

INVITED SCIENTIFIC PRESENTATIONS

Society of Toxicology Annual Meeting **Spring 2020**
Role of Macrophage Surface Receptors on the Uptake and Binding of Protein-coated MWNTs

Society of Toxicology Annual Meeting **Spring 2018**
The Intracellular Fate of Multi-Walled Carbon Nanotubes in Macrophages Using Laser Scanning Confocal Raman Microscopy

Dallas County Community College District STEM Institute Summit **Spring 2016**
Label-free Raman Imaging of Carbon Nanotubes in Macrophages

Richland College Science Department Seminar **Fall 2015**
Infrared Imaging Analysis of Micro-Fibers Obtained from Galveston Bay

Dallas County Community College District STEM Institute Summit **Spring 2015**
Infrared Imaging Analysis of Micro-Fibers Obtained from Galveston Bay

University of North Texas – Howard Hughes Medical Institute Symposium Summer 2014
Discovery of Streptomyces Phage MaiH

Texas A & M University at Commerce – REU Symposium **Summer 2013**
Time Series Observations of the Cataclysmic Variable V1159 Ori

CONTRIBUTED SCIENTIFIC PRESENTATION

14th Annual WITec Confocal Raman Imaging Symposium **Fall 2017**

Determining the Intracellular Fate of Raman-active Nanoparticles in Macrophages

GRADUATE RESEARCH

Bionanosciences Group – The University of Texas at Dallas **June 2016 – Present**

One focus of our Group concerns reports that multi-walled carbon nanotubes (MWNTs) can cause pulmonary fibrosis that may lead to mesothelioma, similar to asbestos. My first project involved optimizing a high-throughput Raman imaging system to study the interactions of various MWNTs with macrophages – the body's first responders to invaders such as microorganisms or manufactured nanomaterials. My second project was an extensive characterization and comparison of the physical and chemical properties of the specific lots of carboxylated MWNTs (cMWNTs) and pristine MWNTs (pMWNTs) that I used in all of my projects. My third project involved investigating the nature of MWNT receptors present on macrophages that may play critical roles in the pathogenesis of MWNTs. In this project, I developed new approaches to determine the important role of class-A scavenger receptors (SR-As) in the binding and accumulation of bovine serum albumin (BSA) coated-MWNTs using SR-A knockout RAW 264.7 cells that were generated using CRISPR-Cas9 technology.

Advisors: Drs. Paul Pantano (Chemistry) and Rockford K. Draper (Biological Sciences)

UNDERGRADUATE RESEARCH

University of Texas at Dallas Senior Honors Thesis **Jan 2015 – May 2016**

I investigated sediment cores from Galveston Bay seeking evidence of ancient hurricanes. The theory involved the discovery of synthetic micro-fibers in some cores at a depth of several centimeters that could be used for constructing a hurricane timeline based on the invention dates of rayon, polyester, and nylon. My contribution to this project was to develop methods to identify the chemical compositions of the Galveston Bay micro-fibers using Fourier Transform infrared (FTIR) microscopy and spectroscopy. My honor thesis, "Infrared Imaging Analysis of Microfibers Obtained from Galveston Bay", revealed a preponderance of rayon fibers in a number of the Galveston Bay core samples.

Advisors: Drs. Paul Pantano (Chemistry) and Homer Montgomery (Geology)

UNDERGRADUATE RESEARCH (continued)

Summer Research Experience at University of North Texas **Summer 2014**

I collaborated on a Howard Hughes Medical Institute (HHMI) research project at UNT regarding phage genome annotation and bioinformatics. This Phage Hunter Advancing Genomes and Evolutionary Sciences (PHAGES) project focused on isolating, purifying, and sequencing new phages found in soil that infect *Streptomyces Griseus.* A new bacteriophage was found with a never before published DNA sequence and it was named after me (MaiH). I performed the annotation of genomes for Mycobacteriophage Bubbles123 and *Streptomyces* phage Karimac by using DNA Master software.

Advisor: Dr. Lee Hughes (Biological Science)

REU Program at Texas A&M University at Commerce **Summer 2013**

I was among only eight students selected from across the nation to shadow Professors and Scientists in performing Physics and Astronomy research. In this internship, we observed many different planets and variable stars, determined transit times, and controlled the SARA 0.9-m Telescope at Kitt Peak National Observatory and the SARA 0.6-m Telescope at Cerro Tololo InterAmerican Observatory in Chile.

Advisor: Dr. Matt Wood (Physics and Astronomy)

WORK EXPERIENCE

Research Assistant **June 2016 – Present**
Department of Chemistry & Biochemistry and Department of Biological Sciences
The University of Texas at Dallas, Richardson, Texas

Teaching Assistant **August 2016 – December 2016**
Department of Chemistry & Biochemistry
The University of Texas at Dallas, Richardson, Texas

Science Lab Assistant **March 2012 – March 2015**
Richland College, Dallas, Texas

Science Tutor **January 2013 – March 2015**
Richland College, Dallas, Texas

LABORATORY SKILLS

- Expertise in:
  - **Analytical techniques:** Raman spectroscopy, Fourier Transform Infrared (FTIR) spectroscopy and imaging, thermogravimetric analysis (TGA), X-ray diffraction (XRD), X-ray photoelectron spectroscopy (XPS), Brunauer-Emmett-Teller (BET) analyses, UV-Vis-NIR spectroscopy, and dynamic light scattering (DLS) and Zeta Potential analyses.
  - **Cell biology techniques:** mammalian cell culturing, single cell cloning, flow cytometry, cytotoxicity assays, and SDS-PAGE analyses.
  - **Cellular imaging techniques:** confocal 3-D Raman imaging, fluorescence imaging, and phase contrast microscopy.
- Proficiencies in:
  - Gene editing and CRISPR-Cas9 methodologies.

OTHER SKILLS

- Vietnamese – Read, write, and speak fluently
- Mastery of Microsoft Office Programs (Word, Excel, Power Point, Access, and Photoshop)
- Ability to work with several operating systems, including WINDOWS, MAC OSX, LINUX
- Excellent interpersonal and communication skills
- Ability to effectively work individually and in a team environment
- Strong attention to details, disciplined, careful and focused